



UNIVERSIDAD NACIONAL AUTÓNOMA DE MÉXICO
PROGRAMA DE MAESTRÍA Y DOCTORADO EN INGENIERÍA
INGENIERÍA ELÉCTRICA – SISTEMAS ELÉCTRICOS DE POTENCIA

ELECTROMAGNETIC MODELING OF LARGE-SCALE HIGH-TEMPERATURE
SUPERCONDUCTOR SYSTEMS

TESIS
QUE PARA OPTAR POR EL GRADO DE:
DOCTOR EN INGENIERÍA

PRESENTA:
EDGAR BERROSPE JUÁREZ

TUTORES PRINCIPALES
DR. FRÉDÉRIC TRILLAUD, INSTITUTO DE INGENIERÍA, UNAM
DR. VÍCTOR MANUEL RODRÍGUEZ ZERMEÑO, NKT
COMITÉ TUTOR
DR. RAFAEL ESCARELA PEREZ, UAM-AZCAPOTZALCO
DR. GERARDO RENÉ ESPINOSA PÉREZ, FACULTAD DE INGENIERÍA

CIUDAD UNIVERSITARIA, CD. MX., MAYO DE 2020



Universidad Nacional
Autónoma de México

Dirección General de Bibliotecas de la UNAM

Biblioteca Central



UNAM – Dirección General de Bibliotecas
Tesis Digitales
Restricciones de uso

DERECHOS RESERVADOS ©
PROHIBIDA SU REPRODUCCIÓN TOTAL O PARCIAL

Todo el material contenido en esta tesis esta protegido por la Ley Federal del Derecho de Autor (LFDA) de los Estados Unidos Mexicanos (México).

El uso de imágenes, fragmentos de videos, y demás material que sea objeto de protección de los derechos de autor, será exclusivamente para fines educativos e informativos y deberá citar la fuente donde la obtuvo mencionando el autor o autores. Cualquier uso distinto como el lucro, reproducción, edición o modificación, será perseguido y sancionado por el respectivo titular de los Derechos de Autor.

JURADO ASIGNADO:

Presidente: Dr. Rafael Escarela Pérez
Secretario: Dr. Gerardo René Espinosa Pérez
1er. Vocal: Dr. Frédéric Trillaud
2do. Vocal: Dr. Francesco Grilli
3er. Vocal: Dr. Víctor Manuel Rodríguez Zermeño

Esta tesis se realizó en el Instituto de Ingeniería, UNAM; y en el Instituto Tecnológico de Karlsruhe, Alemania.

TUTORES DE TESIS:

Dr. Frédéric Trillaud

Dr. Víctor Manuel Rodríguez Zermeño

FIRMA

FIRMA

... al final de este viaje
en la vida quedará
nuestro rastro invitando a vivir
por lo menos por eso es que estoy aquí...

al final de este viaje
en la vida quedarán
nuestros cuerpos tendidos al sol
como sábanas blancas después del amor...

Silvio Rodríguez

Dedicado a:

Mis padres y mi hermana, porque siempre me han brindado más apoyo del que es necesario.

Mis amigos, aquellos que siempre han estado y aquellos a los que fue necesario cruzar un oceano para conocer.

(My friends, those who have always been and those that it was necessary to cross an ocean to meet.)

Diana, porque “en la calle codo a codo somos mucho más que dos”.

Acknowledgments

I wish to express my deepest gratitude to all the people and institutions whose assistance made possible the completion of this project, especially to:

My supervisors, Frédéric Trillaud and Víctor Manuel Rodríguez Zermeño, for their infinite passion to share knowledge.

Francesco Grilli, for receiving me as a visiting student at Karlsruher Institut für Technologie, and for his very valuable comments on this thesis.

Andy Gavrilin, Hubertus Weijers, and Mark Bird; for giving me opportunity to collaborate in the 32 T all-superconducting magnet project, and for inviting me to visit the National High Magnetic Field Laboratory.

Marco Breschi and Pier Luigi Ribani, for receiving me as a visiting student at Università di Bologna.

Consejo Nacional de Ciencia y Tecnología, for the founding received through the doctoral scholarship, CVU 490544.

Universidad Nacional Autónoma de México for the founding received through the grants PAPIIT-2017 TA100617 and PAPIIT-2019 IN107119.

Table of Contents

Chapter 1	Introduction	1
1.1	Large-Scale HTS Systems.....	2
1.2	Motivation.....	2
1.3	Objectives.....	3
1.4	Justification.....	3
1.5	Contributions.....	4
1.6	Organization of the Document.....	5
Chapter 2	State of the Art	7
2.1	Type-I and Type-II Superconductors.....	7
2.2	Critical-State Model.....	9
2.3	Characteristics of HTS.....	11
2.3.1	$E - J$ Relation	11
2.3.2	Critical Current Density	12
2.4	Computation of Electromagnetic Quantities in Superconductors.....	13
2.5	Formulations.....	14
2.5.1	H Formulation	14
2.5.2	$T-A$ Formulation	17
2.6	Strategies for Large-Scale HTS systems	20
2.6.1	Multi-scaling	20
2.6.2	Homogenization	22
Chapter 3	Case Study	25
3.1	Reference Model.....	25
3.2	H Full Model.....	27

3.3	<i>T-A Full Model</i>	29
3.4	<i>H Multi-Scale and H Homogenous Models</i>	31
3.4.1	<i>H Multi-Scale Model</i>	31
3.4.2	<i>H Homogeneous Model</i>	32
3.4.3	Results	32
Chapter 4 <i>H Formulation Strategies</i>		35
4.1	Iterative Multi-Scaling	35
4.1.1	<i>H Iterative Multi-Scale Model</i>	37
4.1.2	Results	37
4.2	Simultaneous Multi-Scaling	40
4.2.1	<i>H Simultaneous Multi-Scale Models</i>	41
4.2.2	Results	42
Chapter 5 <i>T-A Formulation Strategies</i>		45
5.1	Densification	45
5.1.1	<i>T-A Densified Model</i>	47
5.1.2	Results	48
5.2	Simultaneous Multi-Scaling	49
5.2.1	<i>T-A Simultaneous Multi-Scale Models</i>	50
5.2.2	Results	51
5.3	Homogenization	53
5.3.1	<i>T-A Homogeneous Model</i>	55
5.3.2	Results	55
Chapter 6 <i>Comparison</i>		57
Chapter 7 <i>32 T All-Superconducting Magnet</i>		61
7.1	Magnet Description and Model	62
7.2	Critical Current Density	64
7.3	<i>T-A Homogeneous Model</i>	65
7.4	Simulation Results	66
7.4.1	Losses	67
7.4.2	Screening Current-Induced Field	68

7.5	Real-Time Simulations.....	69
<i>Chapter 8</i>	<i>Conclusions</i>	<i>71</i>
<i>Appendix</i>	<i>A.....</i>	<i>75</i>
<i>Appendix</i>	<i>B.....</i>	<i>79</i>
<i>Appendix</i>	<i>C.....</i>	<i>85</i>
<i>Appendix</i>	<i>D.....</i>	<i>87</i>
<i>Bibliography</i>	<i>.....</i>	<i>89</i>

Chapter 1 Introduction

The Dutch physicist Heike Kamerlingh Onnes was the first to liquify helium in 1908 [1]. Three years after this important technological step, Onnes observed that the resistivity of mercury drops to zero at 4.2 K [2], [3]. In the same year, this phenomenon named superconductivity was observed in tin and lead [4]. The first superconductors to be discovered were type-I superconductor, but their use for practical applications was hindered by their low critical field, the field above which the material revert to the normal resistive state [3], [5].

In 1935 Rjabinin and Shubnikov first recognized the type-II superconductors [4]. During the following years new type-II superconductors exhibiting higher critical temperatures and fields were discovered. For instance, Nb_3Sn with a critical temperature of 18 K and a critical field of 25 T was discovered in 1954, and NbTi with a critical temperature of 10 K and a critical field of 12 T was discovered in 1961 [5]. An amazing discovery was made in 1986, when George Bednorz and Alex Müller discovered the first High-Temperature Superconductor (HTS), LBCO , with a critical temperature of 35 K [6]. Soon after in 1987, the first superconductor with a critical temperature above the boiling point of nitrogen was found, YBCO , with a critical temperature of 93 K [7].

More than three decades after the discovery of the HTS, the technology has matured and the second-generation of High Temperature (2G HTS) conductors are nowadays commercially available [8]–[10]. The 2G HTS conductors are made of rare earth-based HTS materials, referred as (RE)BCO (RE for rare earth). These rare earth elements include, but are not limited to, yttrium, samarium and gadolinium [8]. The 2G HTS conductors are layered composites with a thin layer of HTS material, as shown in Figure 1.1. The 2G HTS conductors are also called 2G HTS wires, coated conductors, (RE)BCO tapes, etc. For simplicity, in this manuscript they are called HTS tapes.

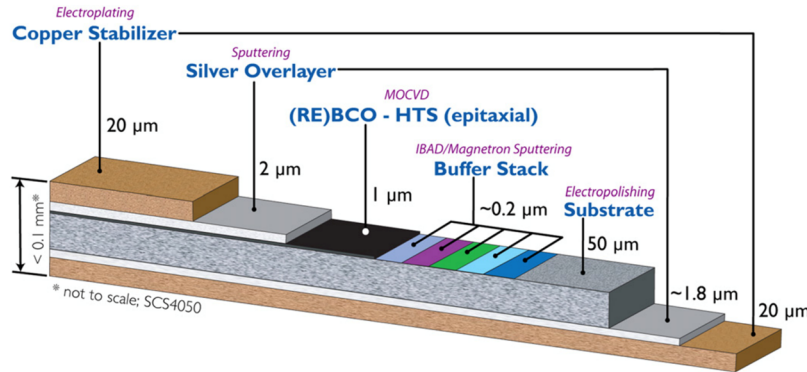


Figure 1.1. Structure of a 2G HTS conductor. SCS4050 commercial tape commercialized by SuperPower Inc. (Image courtesy of SuperPower Inc. [8]).

1.1 Large-Scale HTS Systems

The emergence of HTS tapes has favored the development of devices for power systems, as well as medical and scientific applications. For power systems, it is expected that cables and fault current limiters will soon reach market maturity [11]. Nevertheless, continuing research and development has targeted other power devices such as transformers, generators, and superconducting magnetic energy storage systems [12], [13].

For scientific and medical applications, the interest in the technology has spawned over MRI and NMR magnets [14], [15] and high magnetic field magnets [16]. These devices are typically made of hundreds or even thousands of turns of conductors and are classified as large-scale HTS systems [17]–[19]. The high critical current and high critical field of the HTS tapes allows building high field DC magnets, whose magnetic field can significantly exceed the maximum field achievable with Low-Temperature Superconductors (LTS), this former limit is approximately 25 T [16]. In December 2017, a breakthrough was achieved with the successful demonstration of the 32 T all-superconducting magnet of the National High Magnetic Field Laboratory (NHMFL) in Tallahassee [20].

1.2 Motivation

To ensure safe operation of the HTS devices, their design must consider transient effects that may arise from changes in the external magnetic field and in the transport currents. During these changes, hysteresis losses are generated in the HTS materials, which leads to temperature rises and potentially to the loss of the superconducting state in extreme cases [19], [21], [22]. Therefore, to ensure a reliable operation, the heat load due to the hysteresis losses must be removed by the cryogenic system. In this thesis, the term hysteresis losses is preferred instead of AC losses, because the AC losses may include other contributions like the losses in the copper and other normal conductors [21]. The estimation of

current density distribution, electric and magnetic fields inside the superconductor is a mandatory step for obtaining the hysteresis losses, as well as other quantities of interest for practical applications [23].

Some of these applications, like NMR magnets, require a very high field quality [24]. Therefore, it is important to understand and remedy issues produced by the non-uniform current density distribution in the HTS tapes, e.g., Screening Current-Induced Field (SCIF) and field drift [14], [25]–[27]. The knowledge of the current density and magnetic field distributions is also necessary to address the analysis of the mechanical stresses. These analyses are particularly important to improve the design of high field magnets [16], [28].

1.3 Objectives

The first and general objective of this thesis is to develop efficient strategies to address the electromagnetic modeling of large-scale HTS systems. The proposed strategies will be validated against the H formulation strategy [29], [30]. For its part, the H formulation strategy has been already validated against experimental and simple analytical results. The new strategies must reduce the computational load, memory and computation time, required to analyze such systems, and therefore increasing the size of the systems that can be analyzed.

Once the proposed strategies are validated, an assessment will be done to determine which is the best strategy to address the next objective. The second and particular objective is to build an electromagnetic model of the 32 T all-superconducting magnet of the NHMFL. This last model must be capable of predicting current density distribution, hysteresis losses and screening current-induced field.

1.4 Justification

The available analytical models are restricted to the analysis of individual tapes or relatively simple assemblies [31]. Therefore, it is not possible to apply these analytical tools to the study of large-scale HTS systems, and numerical methods are required [21]. During the last years, the finite element models based on the H formulation of the Maxwell's equations [29], [30] have been extensively and successfully used to address the electromagnetic modeling of HTS systems [32]. Nevertheless, due to the non-linear constitutive relations of the superconducting materials and the large size of some systems, the use of models using the H formulation and considering in detail each individual tape of the system becomes a prohibitive task in terms of computational load. This kind of models are known as H full models.

The limitations of the H full models, have favored the emergence of other strategies like the multi-scaling and homogenization. The multi-scaling strategy is based on analyzing a reduced set of tapes, called analyzed tapes, and approximating the behavior of the full system using the information

of the analyzed tapes [19]. The homogenization assumes that a stack made of HTS tapes can be represented by a single anisotropic homogeneous bulk [22]. As of today, these two strategies have been successfully used together with the H formulation, giving rise to the H multi-scale [19] and H homogeneous [22] strategies.

More recently, the so-called T - A formulation of the Maxwell's equations has been proposed [33], [34]. This approach considers that the thin layers of the HTS tapes can be modeled as 1D lines. Thus far, the T - A formulation is one of the most efficient strategies to address the electromagnetic modeling of systems made of HTS tapes, even though just the T - A full models have been described.

1.5 Contributions

The main contributions of this thesis can be classified in two groups, one group for the strategies based on the H formulation and the other for the strategies based on the T - A formulation.

The first group comprises two strategies: the H iterative multi-scale and H simultaneous multi-scale. Both strategies overcome the main limitation of the already described H multi-scale strategy, which is the lack of knowledge of the current density distribution [19]. The H iterative multi-scale strategy is the iterative implementation of the H multi-scale strategy. The first step of this strategy is to compute the magnetic fields on the basis of a uniform current density distribution, then a new current density distribution can be estimated based on the previously computed magnetic field. The next step is to compute again the magnetic field, but this time, the new current density distribution is used. The process is repeated until a convergence criterion is fulfilled. In the H simultaneous multi-scale strategy, the model is capable of simultaneously computing the current density distribution and the magnetic field.

The second group of contributions comprises the T - A simultaneous multi-scale, T - A homogeneous and T - A densified strategies. The T - A simultaneous multi-scale and T - A homogeneous strategies are the respective counterparts of the H simultaneous multi-scale strategy and the H homogeneous, which has already been described in [22]. The multi-scaling and homogenization are here adapted so that they can be coupled with the T - A formulation. The T - A densified strategy consists in merging the HTS tapes of a stack with their neighboring tapes so that the stack can be modeled by means of a stack made of fewer HTS tapes. The T - A densified strategy does not have an H formulation counterpart.

Figure 1.2 shows a tree diagram with the different strategies that emerge from the combination of the H and T - A formulations, and the densification, multi-scaling and homogenization strategies. In this tree the blue rectangles represent the strategies already described in the literature, while the green rectangles stand for the strategies that are original contributions of this doctoral research.

This thesis contains two additional contributions. First, a comprehensive derivation of the correct choice of the order of the element for the T - A formulation. Second, a new method to interpolate current density distributions based on the inverse cumulative density function interpolation method

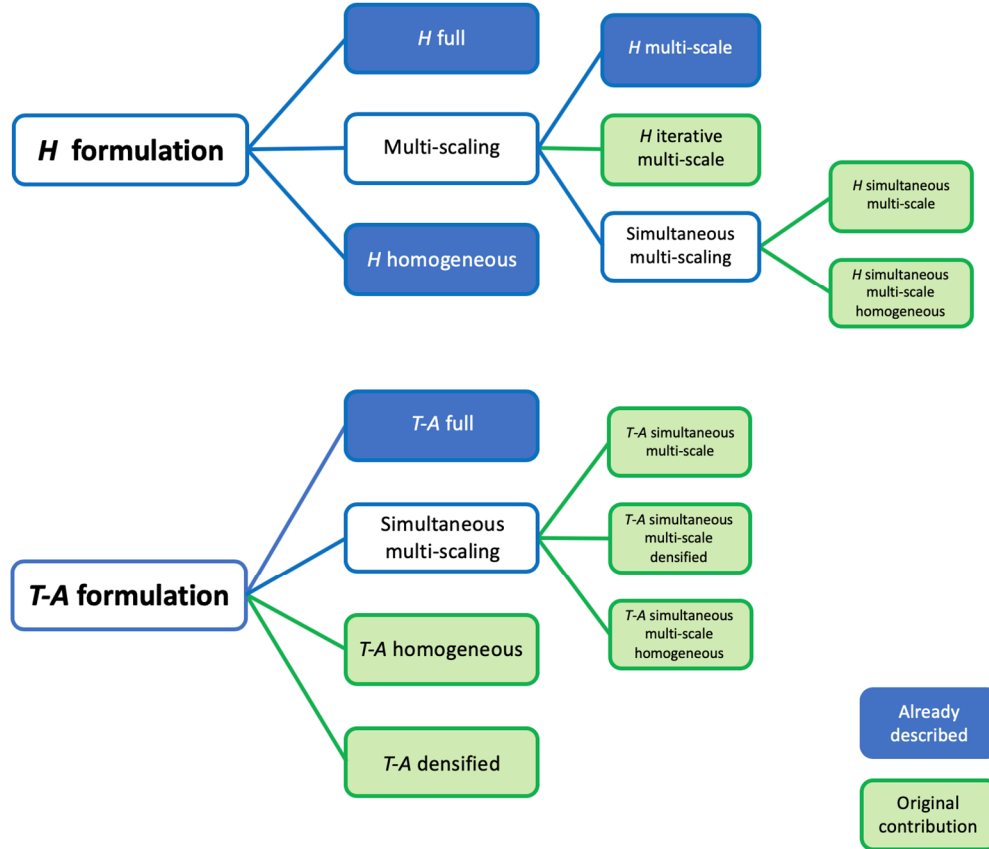


Figure 1.2. Tree diagram showing the strategies that emerge from the coupling of the H and $T-A$ formulation; and the densification, multi-scaling and homogenization strategies.

[35]. The new interpolation method is a complement for the H iterative multi-scale strategy, and allows producing more meaningful results than the usual linear interpolation.

1.6 Organization of the Document

This document is composed of eight chapters and two appendices. Chapter 2, named *State of the Art*, begins with a brief introduction to the superconductivity phenomenon in type-II superconductors. The first sections of Chapter 2 are not intended as a comprehensive review of type-II superconductors, and just the information considered relevant for the present work is included. The following sections contain the description of the H and $T-A$ formulation of the Maxwell's equations. The multi-scaling and homogenization strategies are introduced in the last section of Chapter 2.

The case study used to compare and validate the proposed strategies is presented in Chapter 3, which also presents the models of the case study that can be built using the strategies described in Chapter

2, strategies previously described in the literature. The results presented in this chapter will allow drawing fair comparisons and conclusions about the new proposed strategies.

The main original contributions of the thesis are contained in Chapter 4 and Chapter 5. The new proposed strategies based on the H formulation are described in Chapter 4, while the new proposed strategies based on the $T-A$ formulation are described in Chapter 5. The structure of these chapters is the same, the description of the strategies is followed by the respective models of the case study applying each strategy.

The comparison of the different models of the case study is presented in Chapter 6. The factors that are considered in this comparison include the accuracy, as well as the computation time and the size of the models, which is measured in terms of the number of degrees of freedom. The data compiled in Chapter 6 allows discussing the pros and cons of the different strategies. The electromagnetic modeling of the 32 T all-superconducting magnet from the NHMFL is addressed in Chapter 7.

The concluding remarks of the thesis are presented in Chapter 8. Finally, three appendices are included. Appendix A contains the derivation of the correct choice of the order of the elements for the $T-A$ formulation. The description of the new inverse cumulative density function interpolation method is included in Appendix B. Appendix D contains two tables with parameters used for the calculations presented in Chapter 7. The list of the articles, published during the course of the PhD study, is included in Appendix D.

Chapter 2 State of the Art

This chapter starts by stating the main differences between type-I and type-II superconductors, giving special emphasis to the properties of type-II superconductors. Then, Bean's critical-state model is introduced, this model is useful as a first approximation to describe the electromagnetic behavior of type-II superconductors when subjected to changing conditions, i.e., transport current and external magnetic field.

In the next section, the constitutive relation between the electric field and the current density, and the definition of the critical current density are discussed. Also, a brief revision of the different analytical methods and numerical models is given in a later section. Once the numerical models are presented, the H and T - A formulations of the Maxwell's equations are described. Finally, a brief description of two of the available strategies to analyze large-scale HTS systems, homogenization and multi-scaling, is given. The two formulations as well as the two strategies are going to be the main focus of this work.

2.1 Type-I and Type-II Superconductors

Superconducting materials exhibit zero electrical resistivity below a certain temperature, namely the critical temperature T_c [2]. This is the first important characteristic of the superconducting state. A second important characteristic is the Meissner effect, which is the exclusion of the magnetic field from the interior of the superconducting materials by means of screening currents in the surface of the sample. Hence, the magnetic field penetrates over a thin layer below the surface of the material. The thickness of this layer is referred to as the London penetration depth [36]. The Meissner effect cannot be derived from the Maxwell's equations with the only assumption that the material does not present any resistivity. Indeed, the field exclusion happens regardless of whether the external fields are applied after or before the cooling of the sample. The superconductors are classified as type-I, those which exhibit only the Meissner effect; and as type-II, those which, in addition to the Meissner effect, exhibit a different state at greater magnetic fields, known as mixed state.

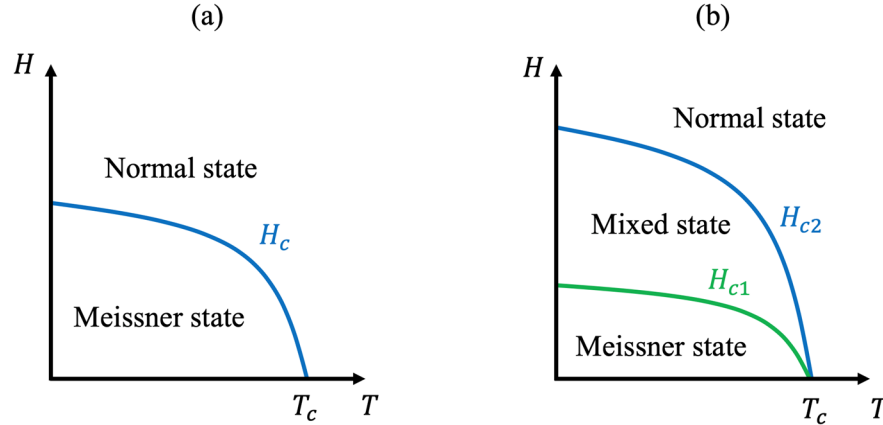


Figure 2.1. (a) Phase diagram for type-I superconductors, for magnetic fields below H_c , the Meissner state is observed. (b) Phase diagram for type-II superconductors, for fields below H_{c1} and above H_{c2} , the mixed state is observed.

The superconducting state does not only require a temperature below T_c , but also the magnetic field must be lower than the critical field H_c [5]. The critical field depends on the temperature, and this dependence is approximately parabolic as shown in Figure 2.1 (a). In type-I superconductors, the Meissner state is completely lost when the value H_c is reached. Type-II superconducting materials exhibit a more complex behavior characterized by two critical fields: the lower critical field H_{c1} , and the upper critical field H_{c2} . For field values below H_{c1} the material is in the Meissner state, for values above H_{c2} the material turns to a normal conducting state. For values between H_{c1} and H_{c2} , it is in the so-called mixed state [37], as depicted in Figure 2.1 (b).

In the mixed state, the magnetic flux penetrates into the superconductors in the form of thin tubes, known as fluxoids. The regions occupied by the fluxoids are in the normal state. Each fluxoid carries one quantum of magnetic flux, and circular supercurrents, called Abrikosov vortices, flow around them [38]. The vortices are pinned to material defects by a “pinning force” [39]. Whenever the transport current or the external magnetic field are changed, the vortices enter or leave the sample through its boundary, and vortices rearrange themselves into another state such that all vortices are pinned again. Figure 2.2 shows a sample where the vortex lattice has been established.

When a transport current is applied, the vortices experience a Lorentz force pushing them in the direction perpendicular to both the flow of the transport current and the magnetic field. When the pinning force is larger than the Lorentz force, no displacement occurs. Hence, the transport current is able to flow without producing any energy dissipation. Conversely, if the Lorentz force surpasses the pinning forces, the vortices move inducing an electric field. Now, the material exhibits a resistivity, whose value approaches that of the normal state, as the magnetic field gets closer and closer to H_{c2} [40].

Almost all pure elemental superconductors are type-I [2]. Due to their low critical fields, type-I superconductors cannot sustain large magnetic fields, and therefore they are not suitable for practical applications [41]. Metal alloys and compounds, which basically include all the existing and

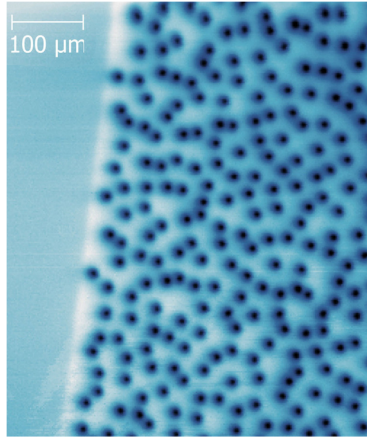


Figure 2.2. Abrikosov vortices in a 200-nm-thick YBCO film imaged by scanning SQUID microscopy. Figure taken from [43], used with permission, Frederik Wells.

commercial HTS and LTS superconductors, are type-II superconductors [2], [36]. Type-II superconductors with strong pinning forces (also called “hard superconductors”) allow high currents to flow under large background magnetic fields, making them ideal for practical applications [5]. Nowadays, the defects, producing pinning effects, are introduced on purpose to improve the current capacity of type-II superconductors [42].

2.2 Critical-State Model

It is a difficult task to associate the local behavior of the Abrikosov vortices with the macroscopic electromagnetic behavior of type-II superconductors. When subjected to changing conditions, the vortex lattice quickly adjusts itself, then a quasi-stationary model with instantaneous interactions can be applied [44]. The so-called Bean’s critical-state model (CSM) is a phenomenological description that was introduced by Bean [45], [46] to describe the magnetic hysteresis of type-II superconductors. It is a useful tool to describe the macroscopic behavior of type-II superconductors.

The CSM states that no current flows in the regions that are not previously penetrated by the Abrikosov vortices. While the current density distribution in the rest of the superconductor is defined by its magnetic history. The penetration of the vortices produces the penetration of magnetic flux density \mathbf{B} , and the change in the magnetic field in turn produces the appearance of electric field \mathbf{E} . There is an upper limit for the magnitude of the current density \mathbf{J} , which is the so-called critical current density J_c , and any \mathbf{E} value, however small, will induce this maximum current density to flow. The mathematical representation of the CSM is as follows,

$$|\mathbf{J}| = \begin{cases} 0, & \text{in regions where } \mathbf{E} = 0 \text{ in all past history} \\ J_c, & \text{elsewhere.} \end{cases} \quad (2-1)$$

The $E - J$ relation is the following,

$$\begin{cases} |\mathbf{J}| \leq J_c, & \text{if } \mathbf{E} = 0 \\ |\mathbf{J}| = J_c, & \text{otherwise.} \end{cases} \quad (2-2)$$

Figure 2.3 shows the characteristic curve this $E - J$ relation. The CSM corresponds to the ideal case depicted by the solid black line. In the original formulation, J_c is constant. Nevertheless, the computational tools existing today allow including refinements like the J_c dependence on the magnetic field and the flux creep effects in the $E - J$ relation [21].

The use of the CSM in a 2D model is illustrated in Figure 2.4. The infinitely long wire has a circular cross-section and carries a sinusoidal transport current with an amplitude lower than the critical current of the wire I_c , and an angular frequency ω . As the transport current is increased, the current density starts to fill the outer region of the cross-section, shielding the central region. As the transport current is decreased, a new current density front with an opposite direction penetrates from the outer of the cross-section. Figure 2.4 shows how the CSM predicts that type-II superconductors screen changes in magnetic field by setting up screening currents at critical values. The results obtained using the CSM do not depend on the change rate of the transport current neither on the change rate of the external field. Additionally, if the transport current or the external field stop changing the current density distribution remains frozen. The CSM is a first approximation for the calculation of magnetic field and current density distributions in HTS systems [21].

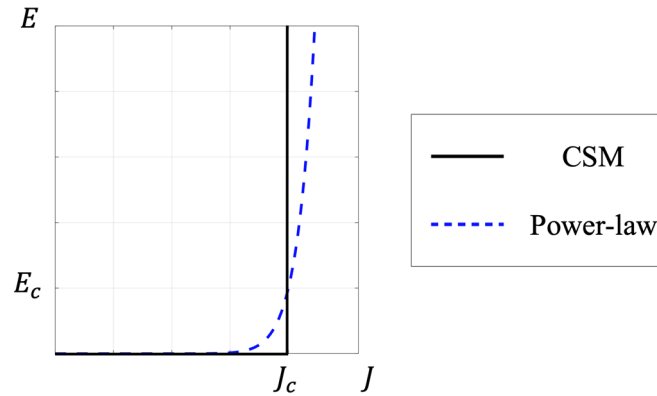


Figure 2.3. $E - J$ characteristic curves of the CSM and the power-law model.

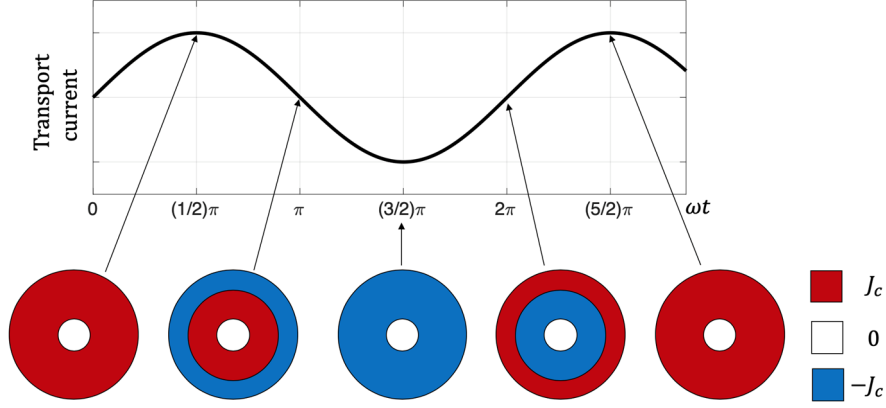


Figure 2.4. Current density distribution in a superconducting wire with circular cross-section carrying a sinusoidal current.

2.3 Characteristics of HTS

2.3.1 $E - J$ Relation

The CSM offers an intuitive picture of the electromagnetic behavior of HTS materials, but the $E - J$ relation (2-2) does not allow to consider overcritical currents neither relaxation effects [40], [47], [48]. The experimental results on the current-voltage characteristic reveal that the $E - J$ relation can be modeled by a power-law, as proposed by Rhyner [49]. The relation between the electric field \mathbf{E} and the current density \mathbf{J} becomes,

$$\mathbf{E} = E_c \left| \frac{\mathbf{J}}{J_c} \right|^n \frac{\mathbf{J}}{|\mathbf{J}|}, \quad (2-3)$$

where J_c is the critical current density, n is the power-law index or n -value, and E_c is called the critical electric field. The election of the E_c value is an arbitrary, usually $E_c = 1 \mu\text{V}/\text{cm}$, meaning that when the superconductor is carrying its critical current I_c , a $1 \mu\text{V}$ voltage drop is observed over 1 cm of the sample. Figure 2.3 shows the characteristic curve of the power law model (dashed blue line). It should be mentioned that both J_c and n depend on the temperature and the magnetic flux density [5], [21], [50].

The non-linear resistivity of the HTS material can be derived from (2-3), and is given by,

$$\rho_{HTS} = \frac{E_c}{J_c} \left| \frac{\mathbf{J}}{J_c} \right|^{n-1}. \quad (2-4)$$

When $n = 1$, equation (2-3) is simplified into the typical linear $E - J$ relation of normal metals. In the limit when $n \rightarrow \infty$, the CSM is retrieved as given by equation (2-2). Usually, n is within the interval (10, 100) [23]. When $|\mathbf{J}|$ is much larger than J_c , the power-law model is not suitable anymore, the validity range of (2-4) is further discussed in [23].

2.3.2 Critical Current Density

Several empirical models have been developed to fit the experimental results and describe the dependence of J_c on the magnetic field in HTS materials. The complexity of the models varies from the Kim model [51], which relies on 2 independent parameters, to the model proposed by Hilton *et al.* [52], relying on 8 independent parameters. Additional models have been compiled in [53].

The so-called Kim-like model (also called elliptical model) [21], [54], [55] has been widely used to model the anisotropic behavior of HTS tapes, where J_c depends not only on the magnitude of magnetic flux density but also on its orientation, as follows,

$$J_c(\mathbf{B}) = \frac{J_{c0}}{\left(1 + \frac{\sqrt{k^2 B_{\parallel}^2 + B_{\perp}^2}}{B_0}\right)^{\alpha}}, \quad (2-5)$$

where B_{\perp} and B_{\parallel} are the magnetic flux density components perpendicular and parallel to the wide surface of the tape, respectively. J_{c0} is the critical current density at zero field, k is the anisotropy parameter, B_0 and α are also material parameters. The model (2-5) provides a reasonable description of the behavior of HTS tapes without artificial pinning centers [56]–[58].

It is difficult to conduct measurements of J_c , typically the J_c values are derived from the I_c measurements [57], [59]. A first approach would be to define J_c as,

$$J_c(\mathbf{B}) = \frac{I_c(\mathbf{B})}{wd_{HTS}th_{HTS}}, \quad (2-6)$$

where wd_{HTS} and th_{HTS} are the width and thickness of the HTS layer of the tape, respectively. This simple approach is good enough in most of the cases. However, if the self-field contribution of the transport current of the conductor is comparable to the applied external field, the application of (2-6) leads to inaccuracies. Therefore, it is necessary to correct the errors induced by the self-field. A successful alternative is the parameter-free method proposed by Zermeño *et al.* [57]. This numerical method provides a good agreement with the experimental data.

2.4 Computation of Electromagnetic Quantities in Superconductors

Some relatively simple formulas have been developed to compute the hysteresis losses in superconductor systems. These analytical methods are limited to the study of systems with simple geometries, and subjected to simple conditions. The method presented by Norris in [60] applies for a single conductor carrying AC transport current, while the methods presented by Halse [61] and Brandt [62] apply for a single conductor subjected to an AC external field. Later methods, like those presented in [63]–[65] apply for conductor stacks under restrictive conditions. For a thorough review of the existing analytical methods the reader is referred to [31]. The estimation of the electromagnetic quantities in systems with more intricate geometries and more complicated operating conditions (real HTS systems) requires the use of numerical methods.

A numerical model is defined as the combination of a model and a numerical method [55]. The modeling of HTS has been extensively investigated in the literature, and different kind of numerical models have been proposed, e.g., integral, variational and differential models [66]. The model proposed by Brambilla *et al.* [67] is an example of the integral models. Among the variational models, it is possible to include the variational formulations proposed by Prigozhin [68], Prigozhin and Sokolovsky [69], and the models using Minimum Magnetic Energy Variation method proposed by Pardo *et al.* [70]. This last method has evolved into the Minimum Electro-Magnetic Entropy Production (MEMEP) method [71], [72]. For a detailed review of the available numerical models, the reader is referred to [21], [66].

The finite element method (FEM) is well documented in the literature [73]–[75] and has been extensively used to find approximate solutions of the Maxwell’s equations in superconductor systems. The Maxwell’s equations can be written using different formulations. The formulations differ from each other in the selection of the state variables. It would seem that the choice of a formulation is arbitrary, but as stated by Grilli *et al.*: “in principle, all these formulations are equivalent, but the solutions of the corresponding partial differential equations (PDE) by means of FEM can be very different” [76]. The most frequently used formulations within the superconductor community, are: the A - V formulation [23], [77]–[79], the T - Ω formulation [80], [81], and the H formulation [29], [30].

The use of the H formulation to address the electromagnetic modeling of superconductors can be traced back to 2003 [82], [83]. The approach, as used nowadays, without separation of the self and applied field contributions, was first introduced by Brambilla *et al.* [29] and Hong *et al.* [30]. The H formulation has been widely used during the last years and has arguably become the *de facto* standard within the applied superconductivity community. A review published by Shen *et al.* [32] claims: “at the time of writing, the H formulation has been used by more than 45 research groups worldwide” [32].

The T - A formulation was recently proposed by Zhang *et al.* [33] and Liang *et al.* [34]. This formulation allows building more efficient models than those based on the H formulation. In the T - A formulation, the HTS tapes are modelled as infinitely thin lines, therefore the mesh complexity and the computation time are reduced. Such infinitely thin approximation has been previously used in [63], [64], [69], [84], [85].

2.5 Formulations

In this section, we briefly recall some of the salient information of the H and T - A formulation. For further information related to the H formulation, the reader is referred to [29], [32]. While, for further information related to the T - A formulation, the reader is referred to [33], [34].

2.5.1 H Formulation

The H formulation uses the magnetic field strength \mathbf{H} as dependent variable.

Within a bounded universe the different materials are represented by different subdomains. Each subdomain has different properties i.e., resistivity ρ and permeability μ , that affect their constitutive relations, defined by,

$$\mathbf{E} = \rho \mathbf{J}, \quad (2-7)$$

$$\mathbf{B} = \mu \mathbf{H}, \quad (2-8)$$

where \mathbf{E} and \mathbf{H} are the electric and magnetic field strength, respectively. \mathbf{B} and \mathbf{J} are the magnetic flux and current density, respectively.

The resistivity of the superconducting subdomain is derived from the power-law model (2-3), while J_c may be defined by the Kim-like model (2-5) or other $J_c - \mathbf{B}$ relation. The resistivity value of the surrounding medium must be sufficiently large, in order to have negligible impact on the solution, a common choice is $\rho_m = 1 \Omega\text{m}$ [22], [86]. Other constant resistivity values are used in the normal conductor subdomains. The vacuum permeability μ_0 is used in the superconducting and surrounding medium subdomains, while for the normal conductors this value can be modified in the case of presence of magnetic materials.

To derive the governing equation of the H formulation, Ampère's law is written, neglecting the displacement current. Then, Faraday's and Ampère's laws are given by,

$$\nabla \times \mathbf{E} = -\frac{\partial \mathbf{B}}{\partial t}, \quad (2-9)$$

$$\nabla \times \mathbf{H} = \mathbf{J}, \quad (2-10)$$

substituting the constitutive relations (2-7) and (2-8) into (2-9), and restricting the present study to linear magnetic materials ($\mu = \text{const}$),

$$\nabla \times \rho \mathbf{J} = -\mu \frac{\partial \mathbf{H}}{\partial t}, \quad (2-11)$$

now, substituting (2-10) into (2-11) yields the governing equation,

$$\nabla \times (\rho \nabla \times \mathbf{H}) = -\mu \frac{\partial \mathbf{H}}{\partial t}. \quad (2-12)$$

Gauss's law $\nabla \cdot \mathbf{B} = 0$ is fulfilled by means of the election of the initial conditions. Taking the divergence of (2-12) yields,

$$\nabla \cdot \{\nabla \times (\rho \nabla \times \mathbf{H})\} = -\nabla \cdot \left\{ \frac{\partial (\mu \mathbf{H})}{\partial t} \right\}, \quad (2-13)$$

where the divergence of the rotational is zero. By exchanging the order of the divergence and the time derivative in the right-hand side it is easy to see that $\nabla \cdot (\mu \mathbf{H})$ is constant. Therefore, if $\nabla \cdot \mathbf{B} = 0$ holds for $t_0 = 0$, then it will hold at any future t .

Let us consider a space with infinite length in the z -direction, then it is possible to consider a two-dimensional (2D) planar model where the x - y plane contains the cross-section of the superconductors. It is important to introduce the 2D models here because this kind of models are the ones used in the rest of this work. We assume that the bounded universe is divided into different subdomains, as shown in Figure 2.5. The subdomains Ω_{sc} , Ω_n , and Ω_{sm} represent the superconductor, normal conductor and surrounding medium, respectively. The surrounding medium subdomain includes the insulating materials and the cryogenic liquid. In the 2D planar model, \mathbf{H} has two non-zero components, while \mathbf{E} and \mathbf{J} have just one non-zero component, therefore (2-12) can be written as follows,

$$\mu \frac{\partial H_x}{\partial t} + \frac{\partial (E_z)}{\partial y} = 0, \quad (2-14)$$

$$\mu \frac{\partial H_y}{\partial t} - \frac{\partial E_z}{\partial x} = 0, \quad (2-15)$$

where $E_z = \rho J_z$, and

$$J_z = \frac{\partial H_y}{\partial x} - \frac{\partial H_x}{\partial y}. \quad (2-16)$$

When no external magnetic fields are considered, Neumann boundary conditions [87], [88] are applied to the external boundary of the bounded universe. To simulate the superconductors under the effect of external magnetic fields, Dirichlet boundary conditions need to be applied, such that at the external boundary the field is equal to the sum of the external and self-contributions [29], [53], [88].

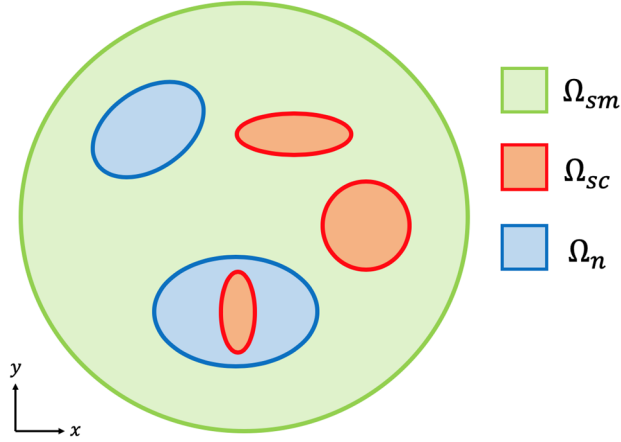


Figure 2.5. Bounded universe of the 2D planar model, formed by the union of the superconductor Ω_{sc} , normal conductor Ω_n , and surrounding medium Ω_{sm} subdomains.

The outer boundary is typically set at a distance of 5 to 10 times the maximum cross-sectional diameter of the conductors [22], [88], [89].

It is also possible to impose a given transport current in each conductor. This can be done by means of integral constraints of the form,

$$I_k = \iint_{\Omega_k} \mathbf{J} \cdot d\mathbf{S}, \quad (2-17)$$

where I_k is the transport current in the k^{th} conductor, and Ω_k is its subdomain. These integral constraints are numerically implemented by the introduction of Lagrange multipliers [22], [29].

The hysteresis loss in the k^{th} conductor is calculated by integrating the instantaneous power dissipation over the a given time span τ ,

$$Q_k = \int_{\tau} \iint_{\Omega_k} \mathbf{E} \cdot \mathbf{J} ds dt. \quad (2-18)$$

In cases where the conditions are periodic it is sufficient to simulate one cycle, the first half of the cycle contains the transient behavior, and the data of the second half of the cycle can be used to compute the average losses [22].

The selection of the elements used in the FEM discretization plays also an important role on the accuracy and computational speed of the numerical model. In the case of the H formulation, several arguments are presented in [22], [29], [89] showing the advantages of the first-order edge elements over other kind of elements. The edge elements assign the degrees of freedom to the edges rather than to the nodes, and they guarantee the continuity of the tangential component of the magnetic field strength between adjacent elements.

The results of the H formulation models have been validated against analytical results [29], as well as different experimental results, e.g., energy dissipation [90], [91], levitation forces [86] and magnetic field mapping [53]. The numerical scheme described in this section can be used to analyze circular coils considering cylindrical coordinates [29], [30]. The strategy has also been extended to 3D problems [92]–[94].

2.5.2 T - A Formulation

The T - A formulation, as reported in [33], [34], relies on the primary assumption that thin superconducting layers of the HTS tapes can be modelled as one dimensional (1D) objects when dealing with a 2D model, or 2D objects when dealing with a 3D model. The infinitely thin approximation is meaningful when dealing with superconductors wires having large aspect ratio (width/thickness), like the 2G HTS tapes where this ratio is in the range of 10^4 [8]. As it is suggested by its name, the T - A formulation requires the implementation of both the T and the A formulations, and therefore both state variables \mathbf{T} and \mathbf{A} , current and magnetic vector potentials, are evaluated.

Here, a 2D planar geometry is assumed, see Figure 2.6. The bounded universe is made of 1D superconducting layers and the surrounding medium Ω_m . The surrounding medium represents not only the insulating materials and the cryogenic liquid, but also the metallic layers of the HTS tapes. It is assumed that the current only flows through the superconducting layers and the surrounding medium is considered non-conductive. The current vector potential \mathbf{T} is exclusively defined over the superconducting layers, while the magnetic vector potential \mathbf{A} is defined over the entire bounded universe.

Considering the constitutive relation (2-7), Faraday's law (2-9) can be rewritten as,

$$\nabla \times \rho \mathbf{J} = -\frac{\partial \mathbf{B}}{\partial t}. \quad (2-19)$$

The current vector potential \mathbf{T} is defined as $\mathbf{J} = \nabla \times \mathbf{T}$ [29]. Substituting this last definition into (2-19) the governing equation of the T formulation is found as,

$$\nabla \times \rho \nabla \times \mathbf{T} = -\frac{\partial \mathbf{B}}{\partial t}. \quad (2-20)$$

Considering the constitutive relation (2-8), Ampère's law (2-10) can be rewritten as,

$$\nabla \times \mathbf{B} = \mu \mathbf{J}. \quad (2-21)$$

The magnetic vector potential \mathbf{A} is defined as $\mathbf{B} = \nabla \times \mathbf{A}$ [29]. Substituting this last definition into (2-9), the governing equation of the A formulation is inferred as,

$$\nabla \times \nabla \times \mathbf{A} = \mu \mathbf{J}. \quad (2-22)$$

Figure 2.6 shows the 2D representation of a stack of HTS tapes. As long as the thickness of the superconducting layer can be neglected, the derivatives of \mathbf{T} with respect to y (the direction perpendicular to the tape) are equal to zero. Then, \mathbf{J} has only one non-zero component defined by,

$$J_z = \frac{\partial T_y}{\partial x}. \quad (2-23)$$

Similarly, equation (2-20) is simplified to an expression that involves the only non-zero component of \mathbf{T} , as follows,

$$\frac{\partial}{\partial x} \left(\rho_{HTS} \frac{\partial T_y}{\partial x} \right) = \frac{\partial B_y}{\partial t}, \quad (2-24)$$

where ρ_{HTS} is the resistivity of the superconducting material, derived from the power-law (2-3) and Kim-like models (2-5).

The required boundary conditions for T_y at the edges of each 1D superconducting layer can be obtained by computing the flux of \mathbf{J} over the cross-section of the original 2D HTS tape which is equal to the transport current flowing in the tape, and then applying Stokes' theorem, as follows,

$$I_k = \iint_{\Omega_k} \mathbf{J} \cdot d\mathbf{S} = \iint_{\Omega_k} (\nabla \times \mathbf{T}) \cdot d\mathbf{S} = \oint_{\partial\Omega_k} \mathbf{T} \cdot d\mathbf{s}, \quad (2-25)$$

where Ω_k is the k^{th} superconductor subdomain, and $\partial\Omega_k$ is its boundary. As shown in Figure 2.6, (2-25) can then be rewritten as,

$$I_k = (T_1 - T_2)\delta, \quad (2-26)$$

where δ is the real thickness of the HTS layer. T_1 and T_2 are the values for T_y at the edges of the 1D layer as shown in Figure 2.6. Thus, a different given transport current can be imposed by modifying T_1 and T_2 . In practice, one value is set to zero and the other is calculated from (2-26).

The component of the magnetic flux density perpendicular to the superconducting layer B_y , required to compute T_y in (2-24), is obtained by calculating \mathbf{A} . In 2D cases, like the case in Figure 2.6, A_z is the only non-zero component of \mathbf{A} , therefore (2-22) can be simplified to,

$$\nabla^2 A_z = 0. \quad (2-27)$$

At first glance, equation (2-22) should be simplified to $\nabla^2 A_z = -\mu J_z$, but for the purpose of computing A_z , J_z is equal to zero all over the bounded universe. The reason for this is that the current

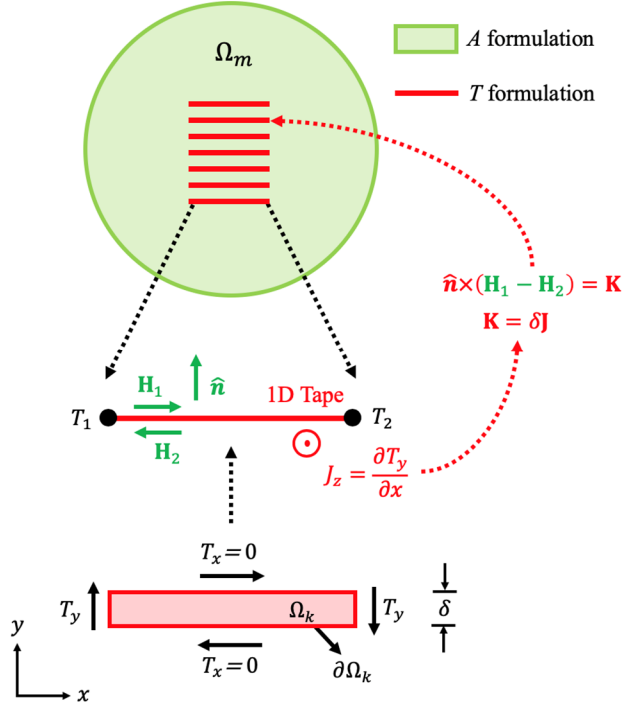


Figure 2.6. Bounded universe consisting of superconducting layers and a surrounding medium. The current vector potential \mathbf{T} is computed over the superconducting layers and the magnetic vector potential \mathbf{A} is computed over the entire bounded universe. The original cross-section of the HTS layer is depicted to show how the boundary conditions are deduced.

is assumed to flow only through the superconducting layers and these layers are assumed to be 1D objects.

In order to couple J_z , computed by means of (2-23), with the A formulation, the surface current density \mathbf{K} is defined as,

$$\mathbf{K} = \delta \mathbf{J}, \quad (2-28)$$

where δ is the real thickness of the HTS layer, and in the 2D case depicted in Figure 2.6, the current density $\mathbf{J} = (0, 0, J_z)$, where J_z is obtained from (2-23), Then, \mathbf{K} is imposed into the A formulation as an external surface current density by means of a boundary condition of the form,

$$\hat{\mathbf{n}} \times (\mathbf{H}_1 - \mathbf{H}_2) = \mathbf{K}, \quad (2-29)$$

where $\hat{\mathbf{n}}$ is the unit vector normal to the tape, while \mathbf{H}_1 and \mathbf{H}_2 are the magnetic field strength vectors above and below the layer, respectively.

The corresponding boundary conditions for A_z in equation (2-27) at the external boundary of the bounded universe can be of two kinds. Dirichlet boundary conditions, of the form $A_z = 0$, are used

when no external field is applied. Neumann boundary conditions are applied to include effects of external magnetic fields.

As in the case of the H formulation, the selection of the elements used in the FEM matters. Here, two kind of elements are required, Lagrange second-order elements are used to approximate \mathbf{A} and Lagrange first-order elements for \mathbf{T} . The proper choice of elements is also an original contribution of the present work, this choice is justified in Appendix A and in [95].

As mentioned previously, the 1D assumption restricts the application of the T - A formulation to systems where the superconducting layers have a large aspect ratio, like 2G HTS tapes. The current density can only vary along the 1D line, then it is not possible to consider the penetration of the parallel magnetic field component into the tape. However, the influence of both the parallel and perpendicular components of the magnetic field are taken into account for the purpose of computing J_c . As a consequence, the T - A formulation is only suitable for cases where the influence of the parallel component of the field is negligible, examples of this kind of cases are the coils analyzed in [19], [33], [34].

2.6 Strategies for Large-Scale HTS systems

As mentioned earlier, the H formulation has been a successful approach to modeling HTS systems, but its application is limited to medium-size systems (systems including hundreds of turns/tapes). In the case of large-scale HTS systems, the use of H formulation models considering in detail each individual tape of the system, is still impaired by the required huge amount of computational resources. This limitation has favored the emergence of strategies to undertake the challenges of modeling large-scale HTS system. For instances, the MEMEP method was used by Pardo to model coils with up to 10400 turns, considering each turns, and coils of up to 40000 turns, using the homogenous approximation of the stacks of tapes [72].

In the present study, a particular attention is given to the homogenization and multi-scaling strategies. The homogenization was first proposed by Clem *et al.* [96], and later refined by others in [22], [69], [97], [98], whereas the multi-scaling was proposed by Quéval *et al.* [99] and subsequently refined in [19]. In this section, it is recalled how the homogenization and multi-scaling, as respectively proposed by Zermeño *et al.* [22] and Quéval *et al.* [19], have been implemented with H formulation to increase the computational efficiency of the models.

2.6.1 Multi-scaling

The idea behind the multi-scaling strategy is to break up the model into several smaller models. Therefore, it is possible to reduce the size of the problem by analyzing in detail only some significant tapes called *analyzed tapes*.

The multi-scale model is formed by two 2D submodels that use the FEM to solve the Maxwell's equations. The first submodel is an A formulation magnetostatic model of the full coil that includes all the tapes with their actual geometry and is called *coil submodel*. The governing equation of the coil submodel is,

$$\nabla \times \nabla \times \mathbf{A} = \mu_0 \mathbf{J}_a, \tag{2-30}$$

where \mathbf{J}_a is the predefined applied current density. This submodel does not consider any superconducting properties, hence the results depend only on the predefined \mathbf{J}_a . The other submodel is an H formulation model, as those described in Section 2.5.1, of a unit cell containing just one tape, called *single-tape submodel*. The single-tape submodel does not consider the normal conductor layers of the HTS tape, and the HTS layer is considered with its actual thickness. The governing equation of this second submodel is already presented in (2-12). Both submodels are depicted in Figure 2.7 (a).

The computational process is carried out in two steps. The first step is to use the coil submodel to estimate the background magnetic field strength \mathbf{H} all across the bounded universe. Then, the magnetic field strength along the boundary of the unit cells of the analyzed tapes is exported to the single-tape submodel as time-dependent Dirichlet boundary conditions. These boundary conditions contain the magnetic field produced by all the tapes affecting a certain analyzed tape. Since the coil submodel is magnetostatic, it is run as many times as there are time steps to build the time-dependent

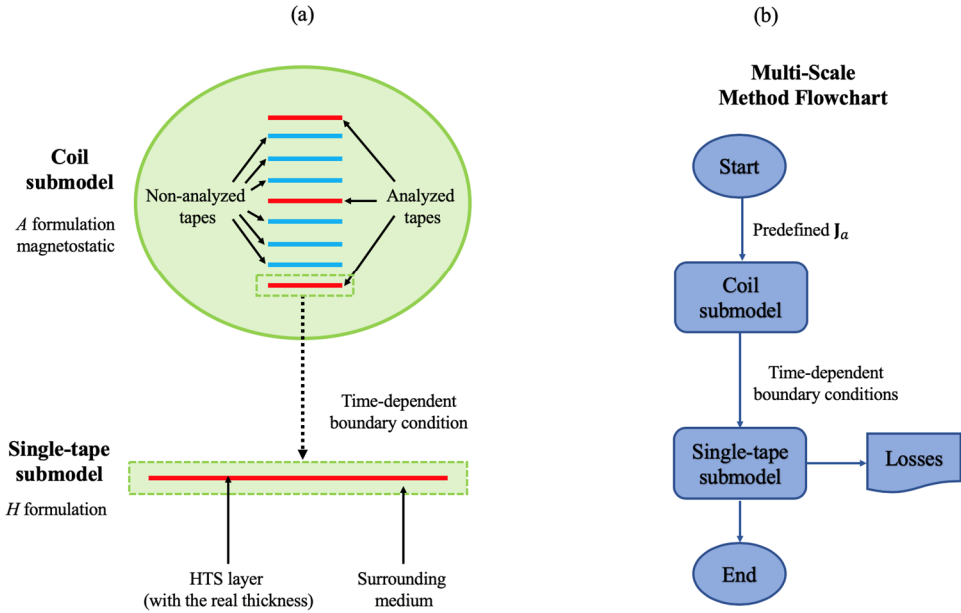


Figure 2.7. (a) Coil and single-tape submodels. Both models consider the actual dimensions (width and thickness) of the HTS layers. (b) Flowchart of the multi-scale method, the background field is computed with the coil submodel, then the losses in the analyzed tapes are computed with the single-tape submodel.

boundary conditions. The second step of the computational process is the use of the single-tape submodel. In this second step, the current density and hysteresis losses are calculated in all the analyzed tapes. Finally, the losses in the *non-analyzed tapes* can be obtained by interpolation. Figure 2.7 (b) shows the flowchart of the multi-scale method.

The increment in the number of the analyzed tapes enhances the accuracy of the model, but this number does not need to be large, e.g. in [19], a 500 turns system is modeled using just 25 analyzed tapes. Additionally, the accuracy relies upon the initial choice for the \mathbf{J} distribution i.e., \mathbf{J}_a . This is a main limitation of the multi-scaling strategy as described by Quéval *et al.* [19]. Two options for the initial choice are proposed in [19]: the first option is a uniform \mathbf{J} distribution in every turn, and the second one is the \mathbf{J} distribution produced by an infinite array. The second choice is closer to the current density estimated with a H full model and leads to more accurate results.

Breaking up the model into several smaller models not only reduces the computational burden, but also allows the parallelization of the problem, further reducing the computation time.

2.6.2 Homogenization

The homogenization strategy is applicable when the HTS tapes are regularly arranged forming stacks, then the stacks can be modeled as homogeneous anisotropic bulks. The HTS tapes are composed by one layer of superconductor and different layers of normal conductors i.e. copper, silver, substrate, see Figure 1.1. As shown in Figure 2.8, a *unit cell* includes one HTS tape and its surrounding medium e.g., cryogenic liquid and/or insulating materials. When the actual stack is transformed into an anisotropic bulk its geometric features are “washed out”. This process is depicted in Figure 2.8. The model should include additional features that allow the electromagnetic behavior of the homogeneous bulk to resemble that of the stack.

The non-superconducting materials forming part of the stack have resistivity values several orders of magnitude larger than those of the HTS material. Therefore, only the HTS material resistivity is considered in the homogenization process. The resistivity of the bulk is derived from the power-law (2-3) and Kim-like models (2-5). Although, the J_c value must be replaced by an engineering critical current density J_{ce} , defined as,

$$J_{ce} = f_{HTS} J_c, \quad (2-31)$$

where

$$f_{HTS} = \frac{\delta}{\Delta}, \quad (2-32)$$

δ is the real thickness of the HTS layer and Δ is the thickness of the unit cell. Thus, the superconducting properties of the bulk are similar to that of the HTS layers, but rescaled to the new

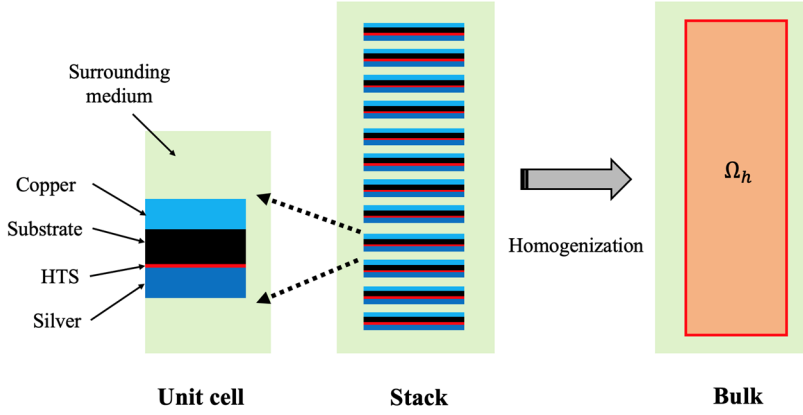


Figure 2.8. The HTS tapes are made of different layers, including one HTS layer. The stack is a periodic array of unit cells, which includes the surrounding medium. The homogenization process transforms the stacks of lines into homogeneous bulks.

cross-section area. As far as just non-magnetic materials are considered, the permeability for all the subdomains is defined to be the vacuum permeability μ_0 .

Now, it is necessary to define current constraints applicable to the homogeneous model mirroring the fact that each tape of the stack carries the same current. When a stack is modeled by means of an H formulation full model, many integral constraints are necessary to impose the desired transport currents, one for each HTS tape. To address this problem, the bulk subdomain Ω_h is further subdivided into bulk's subsets $\Omega_{h,i}$, as depicted in Figure 2.9. Thus, one constraint is necessary for each bulk's subset, instead of one constraint per tape. These constraints have the following form,

$$\hat{I}_i = \iint_{\Omega_{h,i}} \mathbf{J} \cdot d\mathbf{S}, \quad (2-33)$$

where \hat{I}_i is the transport current in the i^{th} bulk's subset $\Omega_{h,i}$. The current \hat{I}_i is a function of the thickness of the bulk's subset. Additionally, each subset is discretized by means of a rectangular structured mesh with only one element along its thickness. The form of the mesh and the use of first-order edge elements guarantee the condition $\partial \mathbf{J} / \partial y = \mathbf{0}$ within each subset. Hence, the homogenization allows the reduction of the applied constraints. The decision about the number of bulk's subsets must be made by reaching a compromise between the computation time and the accuracy.

The homogenized stack has almost the same electromagnetic behavior of the original HTS stack, but the numerical model has a much smaller number of degrees of freedom (DOF), therefore the solutions can be obtained much more quickly. The strategy described here has been extended to 3D problems by Zermeño *et al.* [98].

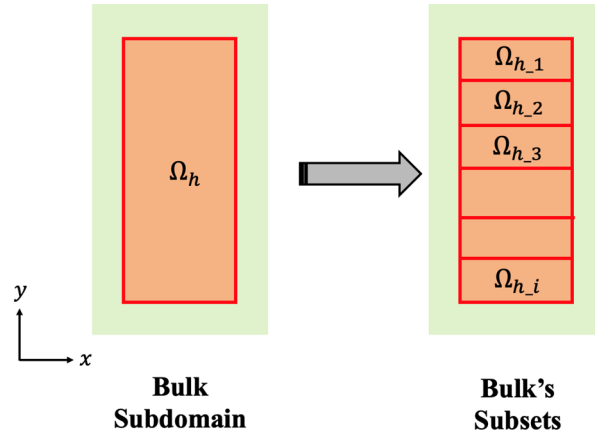


Figure 2.9. Further subdivision of the bulk subdomain Ω_h into bulk's subsets Ω_{h_i} . The number of integral constraints now depends on the number of subsets and not of the number of tapes.

Chapter 3 Case Study

The case study together with its references and full models are presented in this chapter. The full models use the H and T - A formulations described in the previous chapter. The homogenous and multi-scale models using the H formulation as described in the previous chapter are also presented here. This chapter contains the case study models using strategies already proposed by other authors. These models do not represent an original contribution to the present work, but will allow a fair comparison of the new strategies described in the following chapters.

The development of a home-made code from scratch to solve the problems described here represents a substantial amount of work. The use of commercial FEM software packages can help in this task. All the models discussed in this thesis were implemented in COMSOL Multiphysics 5.3 [100]. COMSOL has specific modules for electromagnetic calculations (AC/DC module) and for general equation-based models (PDE module). Additionally, this software provides the options to select between elements of different types and orders. The computer used to perform the simulations is an Apple MacBookPro (3 GHz Intel Core i7-4578U, 4 cores, 16 GB of RAM). The basic characteristics of the computer are important to weight the reported computation times.

3.1 Reference Model

Within the applied superconductivity community, the term pancake refers to either a circular coil or a racetrack coil (coil shaped as a racetrack) [19], [101]. The pancakes can be modeled considering their cross-section using stacks of tapes and 2D approximations. The models for circular coils consider cylindrical coordinates, while the sufficiently large internal radius of the racetrack coils allows using cartesian coordinates [22], [29], [102].

The case study used in this work is the racetrack coil used in [19], [95]. This coil has 10 pancakes, each consisting of 200 turns, bringing a total number of turns equal to 2,000. The geometric parameters of the racetrack coil are summarized in Table 3-1. The symmetry of the racetrack coil allows modeling just one quarter of the cross-section of the coil. Therefore, it is possible to consider

only 5 pancakes, each consisting of 100 turns in a planar 2D geometry. The coil, its cross-section and the modeled section are depicted in Figure 3.1. In this work, the H formulation model that considers in detail each system's tape, presented in [19], [95], is used to validate the rest of the models, and is hereinafter called reference model.

Since the resistivity of the surrounding medium is several orders of magnitude larger than the resistivity of the superconducting layer, the model does not consider normal conductor subdomains Ω_n , and the surrounding medium subdomain Ω_{sm} has a resistivity value $\rho_{sm} = 1 \Omega m$, as proposed in [22]. The superconducting Ω_{sc} and surrounding medium Ω_{sm} subdomains have a permeability equal to the permeability of vacuum μ_0 [19]. The resistivity of the superconducting subdomain is derived from the power-law (2-4) and the Kim-like (2-5) models. The electromagnetic parameters of the coil are summarized in Table 3-2.

Table 3-1. Case study geometric parameters.

Parameter	Value
Number of pancakes	10
Turns per pancake	200
Unit cell width	4.45 mm
Unit cell thickness	293 μm
HTS layer width	4 mm
HTS layer thickness	1 μm

Table 3-2. Case study electromagnetic parameters.

Parameter	Value
E_c	$1 \times 10^{-4} Vm^{-1}$
n	38
J_{c0}	$2.8 \times 10^{10} Am^{-2}$
B_0	0.04265 T
k	0.29515
α	0.7
Ω_{sm} resistivity ρ_{sm}	1 Ωm
μ_0	$4\pi \times 10^{-7} Hm^{-1}$

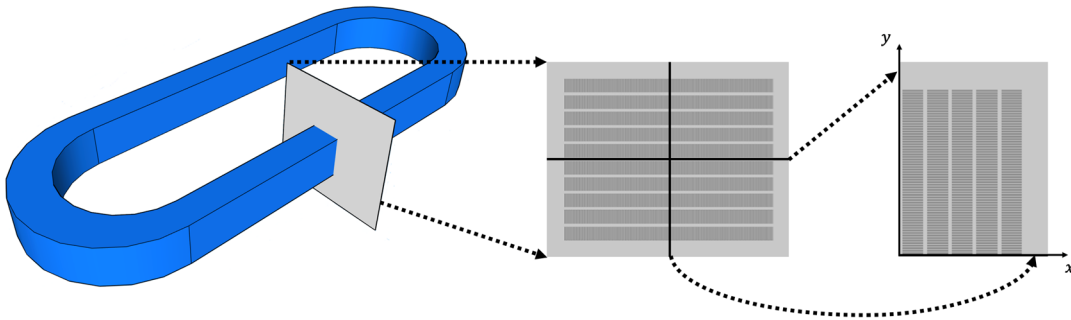


Figure 3.1. Racetrack coil used as case study. The coil has 10 pancakes with 200 turns per pancake. The coil can be modeled considering only its cross-section. Due to the symmetry, the analyzed portion of the case study has 5 pancakes with 100 tapes.

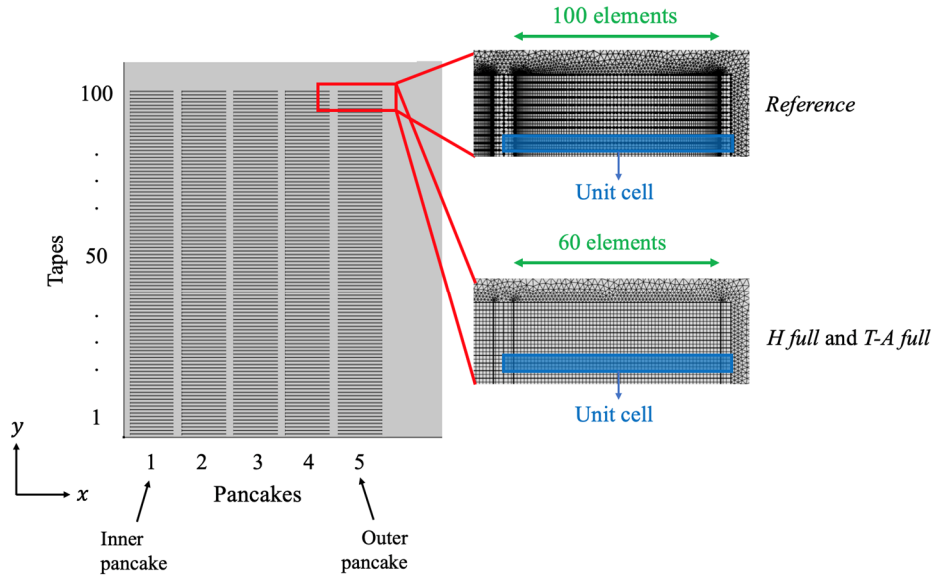


Figure 3.2. Geometry and mesh of the reference, H full and $T-A$ full models corresponding to $\frac{1}{4}^{\text{th}}$ of the coil's cross section. The mesh in the unit cells is structured with 100 elements along the tape's width for the H full model and 60 elements for the $T-A$ full model.

Figure 3.2 depicts the geometry of the reference model including the numbering of the pancakes and tapes. The mesh of the unit cells is structured, and considers only one element along the HTS layer's thickness and 100 elements along its width. The 100 elements are distributed symmetrically with respect to the center of the tape with an increasing number of elements towards the edges of the tape, see Figure 3.2. This kind of elements' distributions allows the accurate estimation of the \mathbf{J} distribution at the edges of the tapes, where the penetration of the magnetic field makes the current fronts to appear [19].

3.2 H Full Model

Another group of H formulation models was built to assess the impact of the numbers of elements along the tape's width. These models are similar to the reference model, but the mesh used in the unit cells is modified. The mesh considers different numbers of elements ranging from 25 to 150, while maintaining a uniform distribution of the elements for all the cases. This assessment goes beyond the 100 elements to take into account the fact that the mesh of the reference model considers an increasing element density at the extremities of the tapes.

The models are simulated for one cycle of a sinusoidal transport current with an amplitude of 11 A, and a frequency of 50 Hz. The value 11 A was chosen because at the peak of the cycle the tape 1 in pancake 5 is completely penetrated by the current density.

The quantitative comparison of the models is carried out by calculating the relative error of the average hysteresis losses and the coefficient of determination (R^2) of the \mathbf{J} distributions. The average hysteresis losses are obtained using data of the second half of the cycle, as follows,

$$Q_{av} = \frac{2}{P} \int_{P/2}^P \iint_{\Omega_{sc}} \mathbf{E} \cdot \mathbf{J} \, ds \, dt, \quad (3-1)$$

where P is the period of the sinusoidal cycle, and Ω_{sc} are the superconducting subdomains. The relative error of the average losses, expressed in percent, is defined as,

$$er_Q = \frac{(Q_{M_{av}} - Q_{R_{av}})}{Q_{R_{av}}} 100 \%, \quad (3-2)$$

where $Q_{R_{av}}$ and $Q_{M_{av}}$ are the average losses computed with the reference and with the model that is being compared, respectively. For the test conditions $Q_{R_{av}} = 127.24$ W/m.

Unlike the average hysteresis losses, the \mathbf{J} distributions are multivariable functions instead of scalars. The coefficient of determination is a widely used metric to evaluate the goodness of the fit [103]. Here, it is used to compare the current density along tapes' width for all the tapes and for all the time steps. The coefficient of determination is defined as,

$$R^2 = 1 - \frac{\int_0^P \iint_{\Omega_{sc}} (\mathbf{J}_R - \mathbf{J}_M)^2 \, ds \, dt}{\int_0^P \iint_{\Omega_{sc}} (\mathbf{J}_R - \bar{\mathbf{J}}_R)^2 \, ds \, dt}, \quad (3-3)$$

where \mathbf{J}_R and \mathbf{J}_M are the current densities computed with the reference model and tested model, respectively. $\bar{\mathbf{J}}_R$ is the mean value of \mathbf{J}_R . It must be remembered that $R^2 = 1$ means a perfect matching between \mathbf{J}_R and \mathbf{J}_M . When used to compare the models, the R^2 coefficient has an additional advantage over er_Q . The averaging nature of er_Q tends to hide both local and instantaneous errors, e.g., an instantaneous excess in the losses may be compensated by another instantaneous deficit; while these same errors have a cumulative effect in the R^2 coefficient.

To allow comparing the computation times, the normalized computation time is defined as,

$$\bar{ct} = \frac{ct_M}{ct_R} 100 \%, \quad (3-4)$$

where ct_R and ct_M are the computation time required by the reference model and by the tested model, respectively. For the test conditions $ct_R = 31$ h 32 min.

The results of the simulations using different number of elements are summarized in Figure 3.3. The relative error of the losses er_Q and R^2 are plotted as a function of the number of elements along the tapes' width. The relative error of the losses is reduced as the number of elements is incremented. The results of Figure 3.3 show that the use of coarser meshes leads to overestimation of the losses, which is good news because the models with a coarser mesh require less computational recourses, then when less computational recourses are used the losses are overestimated. The R^2 coefficient

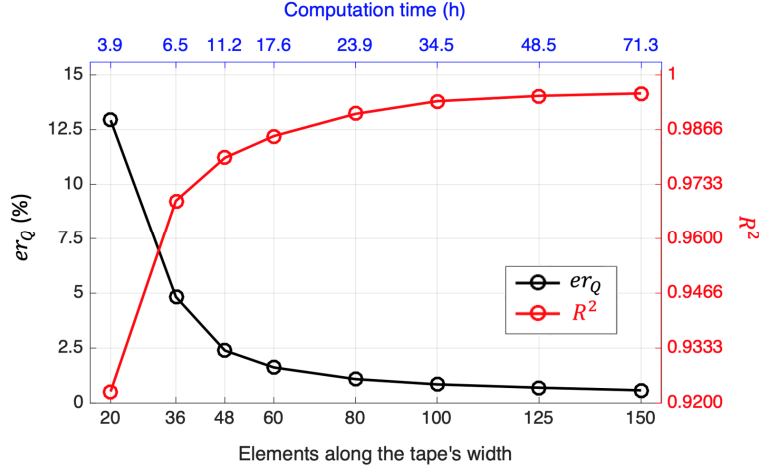


Figure 3.3. Relative error of the losses er_Q and coefficient of determination R^2 of \mathbf{J} as a function of the number of elements along the tape's width. The accuracy improves as the number of elements increases. The upper axis shows the computation time. The positive sign of the er_Q values means that the hysteresis losses are overestimated when fewer elements along the tape's width are used.

increases toward 1 as the number of elements is incremented. The upper axis is included to report the computation time. As expected, the increase in the number of elements produces the increase of the computation time. When the number of elements is 150 the required computation time is 71 h 18 min, ($\bar{c}t = 226\%$).

When the number of elements along the tapes' width is 60, the relative error of the losses takes the value $er_Q = 1.62\%$ (less than 2%), the R^2 is 0.9848 (more than 0.98), and the computation time is 17 h 36 min ($\bar{c}t = 75.8\%$). Here, it is considered that with 60 elements along the tapes' width, the compromise between accuracy and computation time is fulfilled. The H formulation model that considers in detail each tape of the system and uses 60 elements along the tapes' width is hereinafter called H full model. The mesh of the unit cells of the H full model is presented in Figure 3.2. In addition, throughout the rest of this work, it is assumed that all models have 60 elements along the tapes' width, with the exception of the reference model. The difference between the reference and the H full model is the distribution and the number of elements along the tapes' width, 100 elements with a non-uniform distribution for the reference model, and 60 elements with a uniform distribution for the H full model.

3.3 T-A Full Model

The $T-A$ full model, as well as the reference and H full models, considers in detail all the tapes. Therefore, in the $T-A$ full model the current vector potential \mathbf{T} is computed in every single-tape. The mesh of the unit cells is also structured as shown in Figure 3.2. Here, the HTS layers have no thickness and the mesh is made of 1D elements uniformly distributed along the HTS layers' width.

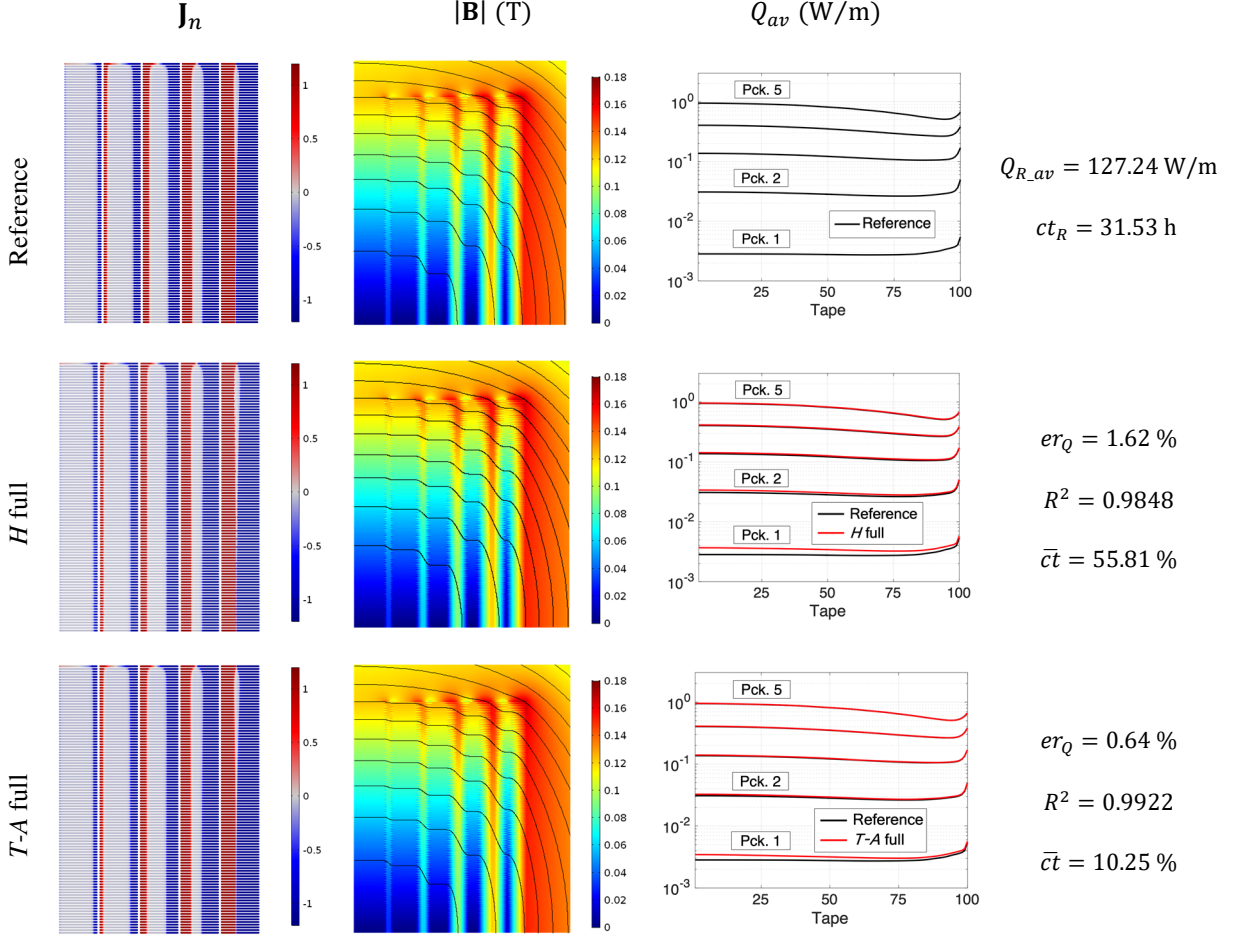


Figure 3.4. Results of reference, H full and T - A full models. The first and second columns show \mathbf{J}_n and $|\mathbf{B}|$ at the second peak of the transport current ($t = 15$ ms). The third column shows the average losses as a function of the tape's number inside each pancake, the tapes and pancakes are numbered as indicated in Figure 3.2.

The T - A full model is also simulated for one cycle of a sinusoidal transport current with an amplitude of 11 A, and a frequency of 50 Hz. To validate the model, the results are compared against the results of the reference model. The relative error of the losses is $er_Q = 0.64\%$, the coefficient of determination is $R^2 = 0.9922$, and the computation time is 3 h 14 min ($\bar{c}t = 10.25\%$). These values, more specifically the normalized computation time, demonstrate that the T - A formulation allows building more efficient models than the models using the H formulation.

The normalized current density $\mathbf{J}_n = \mathbf{J}/J_c$ at the second peak of the transport current $t = 15$ ms computed with the reference, H full and T - A full models is shown in the first column of Figure 3.4. The magnitude of the magnetic flux density $|\mathbf{B}|$, also at $t = 15$ ms is presented in the second column. The plots in these first columns are indistinguishable to the naked eye. The third column of Figure 3.4 shows the average hysteresis losses in each tape. The x-axis in the plots represents the tape's number, and there are five curves in each plot, one for each pancake. The numbering of the tapes and pancakes follows the order presented in Figure 3.2. The losses estimated with the H and T - A full

models are very similar to the losses estimated with the reference model, but there are visible differences in the losses of the first two pancakes.

The losses in pancake 5 are almost three orders of magnitude larger than the losses in pancake 1. This difference is due to the increase in the current penetration in the tapes moving from pancake 1 to pancake 5. Also, the higher losses in pancake 5, the outermost pancake, are related to the difference in the field direction, having a higher perpendicular component in this pancake than in the innermost pancakes. Although there are variations in the losses at the end of the pancakes, the losses in the tapes of a given pancake remain within the same order of magnitude. The plots in Figure 3.4 demonstrate that the T - A full model can also achieve accurate estimations of the electromagnetic quantities at a local level, i.e. along each individual tape.

3.4 H Multi-Scale and H Homogenous Models

3.4.1 H Multi-Scale Model

The model of the case study which applies the multi-scaling strategy, as described in Section 2.6.1, is called H multi-scale model. The position of the analyzed tapes is selected following the directives proposed in [19], [104], This model considers 6 analyzed tapes in each pancake, 30 analyzed tapes in total. The set of analyzed tapes in each pancake is $\{25, 66, 88, 96, 99, 100\}$, there are more analyzed tapes in the upper part of the pancakes to catch the higher variations of the losses between tape 60 and 100. In this specific case the number and the position of the analyzed tapes is enough to retrieve the form of the plots of the losses in Figure 3.4. The position of the analyzed tapes is shown in Figure 3.5. The mesh of the unit cells in the coil submodel, as well as the mesh of the single-tape submodel, is structured as depicted in Figure 3.5.

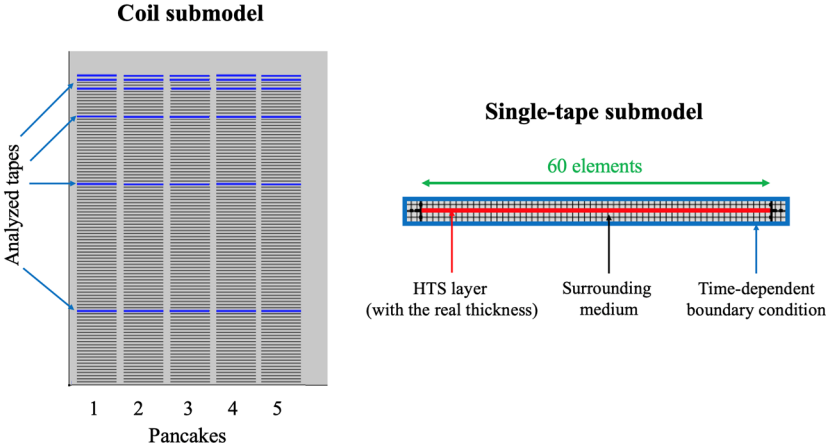


Figure 3.5. H multi-scale model. Position of the analyzed tapes in the coil submodel. The mesh of the single-tape submodel considers 60 elements along the tape’s width.

Once the hysteresis losses are computed along the analyzed tapes, the Piecewise Cubic Hermite Interpolating Polynomial (PCHIP) method [105] is used to interpolate the losses in the non-analyzed tapes from the analyzed tapes.

3.4.2 *H* Homogeneous Model

The *H* homogeneous model of the case study applies the homogenization strategy as described in Section 2.6.2. The model considers 5 bulks, one for each pancake, and each bulk is subdivided into 6 subsets, as shown in Figure 3.6. The distribution of the subsets is analogue to the distribution of the analyzed tapes in the *H* multi-scale model. This means that the position of the analyzed tapes in the multi-scale model corresponds to the center of each bulk subset. The subsets in the upper part of the pancakes have a larger aspect ratio than the ones close to the symmetry plane. Such kind of distributions has been recommended for homogenous models in [19], [22]. The mesh of the bulks is structured considering one element along the subset’s thickness and 60 elements along the tapes’ width, as depicted in Figure 3.6.

The hysteresis losses are computed in each bulk’s subset. The losses in each subset are divided by the number of tapes included in each subset, then it is possible to approximate the losses in each tape.

3.4.3 Results

To compare and validate the *H* multi-scale and *H* homogeneous models, as previously, the models were simulated considering a cycle of an 11 A, 50 Hz sinusoidal transport current. Figure 3.7 presents

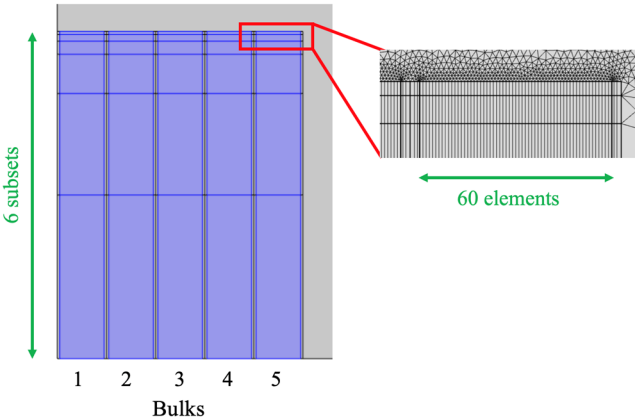


Figure 3.6. Geometry and mesh of the *H* homogeneous model. Each bulk is subdivided into 6 subsets. The mesh of the bulks considers 1 element along the subsets’ thickness and 60 elements along the tapes’ width.

the results of the simulations. To facilitate the comparisons, the results of the reference model are also presented. The figure presents \mathbf{J}_n and $|\mathbf{B}|$, both at $t = 15$ ms, and Q_{av} .

The predefined \mathbf{J} distribution \mathbf{J}_a used by the H multi-scale model is uniform, as can be seen in the first column first row of Figure 3.7. It can be observed that the uniform \mathbf{J}_a is not the best approximation of the \mathbf{J} distribution, i.e., \mathbf{J}_a does not contain any screening current. Consequently, the magnetic flux density and the hysteresis losses estimated with the H multi-scale model exhibit noticeable differences with respect to the results of the reference model. The plot in the first row third column shows that the largest errors in the losses are present in the tapes at the upper part of the pancakes, where the screening currents play a larger role in the magnetic flux density distribution than in other parts of the system [19], [22]. The red circles in the plot of the losses in the first row third column indicate the position of the analyzed tapes. Conversely, the screening currents are successfully reproduced by the H homogenous model, producing a more accurate estimation of the magnetic flux density and the losses than the H multi-scale model, as can be seen in the last column of Figure 3.7.

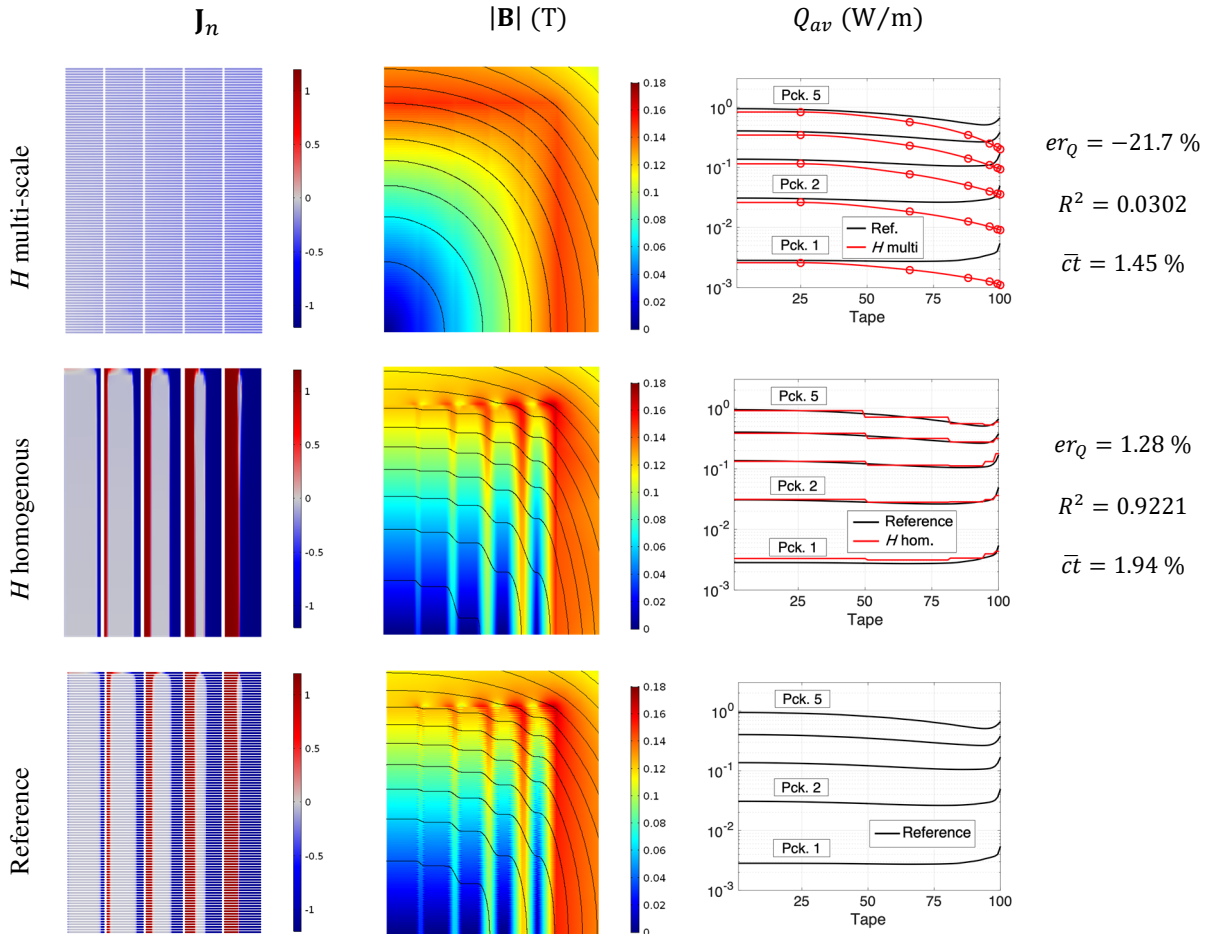


Figure 3.7. Results of H multi-scale and H homogeneous models. The first and second columns show, respectively, \mathbf{J}_n and $|\mathbf{B}|$ at the second peak of the transport current ($t = 15$ ms). The third column shows the average losses as a function of the tape's number inside each pancake.

The relative error of the losses is $er_Q = -21.7\%$ for the H multi-scale model, the negative sign indicates that the hysteresis losses are underestimated. The R^2 value of the \mathbf{J} distributions is 0.0304 for the H multi-scale model. The H homogenous model provides a more accurate estimation of the losses and the \mathbf{J} distribution, with the following values, $er_Q = 1.28\%$ and $R^2 = 0.9221$. In the case of the homogeneous model, the R^2 coefficient is computed rescaling the current density obtained with the homogenous model and considering just the values at the positions of the original superconductor subdomains.

The computation time required by the H multi-scale model is 27 min 30 s ($\bar{c}t = 1.45\%$). This time is the summation of the time required to run the coil submodel (5 min) and the time required to run the single-tape submodel 30 times, one for each analyzed tape (the average computation time of the single-tape submodel is 45 s). It is recalled that the computation of the H multi-scale model can be reduced if the analyzed tapes are analyzed in parallel. The computation time required by the H homogenous model is 36 min 44 s ($\bar{c}t = 1.94\%$). The computation time of both models is almost the same, while the accuracy of the H homogenous is considerably better.

On basis of the results presented in this section it is shown that, for this case study, the H homogenous model is a better alternative than the H multi-scale. Nevertheless, it should be mentioned that the multi-scaling strategy allows addressing the study of larger systems. It may be the case that, for a sufficiently large system, the H homogenous model exceeds the memory resources of the computer used to perform the simulations. Moreover, the homogenous strategy is limited to the analysis of systems made of stacks of HTS tapes. While the multi-scaling strategy is not limited in this way, see for example [106].

Chapter 4 *H* Formulation Strategies

This chapter presents two improved *H* multi-scaling strategies. These strategies are called iterative multi-scaling and simultaneous multi-scaling. Both strategies can be understood as an evolution of the multi-scaling strategy as presented in Section 2.6.1. These strategies are original contributions of the present research work.

4.1 Iterative Multi-Scaling

The accuracy of the multi-scale models depends on the accuracy on the background magnetic field [19]. The magnetic field is computed on the basis of the current density distribution in the conductors. Therefore, to be able to assess correctly the magnetic field, the current density should be accurately computed over each individual tape. The lack of knowledge of the **J** distribution and therefore the poor estimation of the background magnetic field is the main limitation of the *H* multi-scale strategy. This limitation became apparent in Section 3.4.3, where the **J** distribution was assumed to be uniform. To address this issue and preserve the capability to analyze the system by means of a reduced set of analyzed tapes, a new method referred to as iterative multi-scale strategy is proposed hereinafter.

The *H* multi-scale models solve a dynamic problem, i.e., estimate the electromagnetic quantities at every time step. The iterative multi-scale strategy allows obtaining a new and more accurate dynamic solution at each iteration, thanks to the fact that the information flow is more complex in this strategy. In the non-iterative multi-scaling strategy, the flow of information goes from the coil submodel to the single-tape submodel. Whereas, in the iterative strategy, the information flows from the single-tape submodel to the coil submodel, and at the following iteration the data flows back to the single-tape submodel.

To initialize the iterative procedure, the current density in every tape is supposed to be uniform, then the coil submodel is used to estimate the background magnetic field. The magnetic field strength

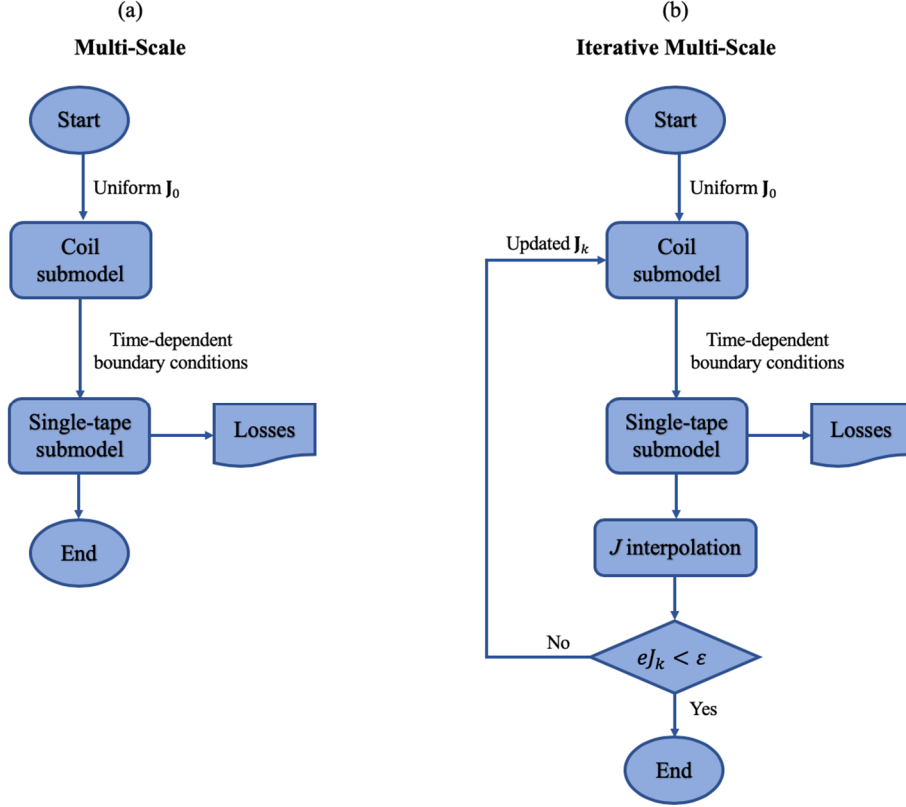


Figure 4.1. Flowcharts for the multi-scale and iterative multi-scale methods. In the iterative method, the \mathbf{J} distributions of the analyzed tapes are used to approximate the \mathbf{J} distribution of the non-analyzed tapes. The current density for all the tapes is fed back to the coil submodel.

along the boundary of the analyzed tapes for every time step is used as time-dependent boundary condition in the single-tape submodel. The single-tape submodel is not only used to compute the hysteresis losses, and the current density is also computed in the analyzed tapes. Once the \mathbf{J} distributions in all the analyzed tapes have been computed, an interpolation method is used to estimate the \mathbf{J} distributions in the rest of the tapes, i.e., the non-analyzed tapes. The new \mathbf{J} distribution for all the tapes is exported to the coil submodel and a new distribution of the magnetic field is computed. The process is repeated to obtain better estimations of the \mathbf{J} distribution and, in turn, of the background magnetic field. For comparison, Figure 4.1 shows the flowchart of the iterative multi-scale method alongside the flowchart of the multi-scale method.

To exit from the iterative loop, the \mathbf{J} distribution for all the tapes of the current iteration is compared with the \mathbf{J} distribution of the previous iteration. As described in Section 3.2, when the R^2 coefficient was defined, it is preferable to compare the current density, because the relative error of the average losses er_Q , as defined in (3-2), may hide instant errors. In the literature of numerical methods [103], it is usual that the algorithms are built to gradually reduce a defined error. Therefore, it is necessary to define a global error of the \mathbf{J} distributions which does not hide local nor instant errors. The error of the \mathbf{J} distributions at the iteration k is computed as,

$$eJ_k = \frac{\sqrt{\int_0^P \iint_{\Omega_{sc}} (\mathbf{J}_{k-1} - \mathbf{J}_k)^2 ds dt}}{\sqrt{\int_0^P \iint_{\Omega_{sc}} (\mathbf{J}_{k-1})^2 ds dt}} \quad (4-1)$$

where P is the period of the analyzed sinusoidal cycle, and Ω_{sc} are the superconducting subdomains, \mathbf{J}_{k-1} and \mathbf{J}_k are the \mathbf{J} distributions for the iteration k and $k - 1$, respectively. Thus, if the error eJ_k is smaller than a user-predefined criterion ε , then the process is completed.

4.1.1 H Iterative Multi-Scale Model

The model of the case study applying the iterative multi-scaling strategy is referred to as *H iterative multi-scale model*. It uses the set of analyzed tapes used by the H multi-scale model of the previous chapter, i.e., in each pancake the set is $\{25, 66, 88, 96, 99, 100\}$. The geometries of the coil submodel and the single-tape submodel of the iterative model are those presented in Figure 3.5.

The multi-scaling strategy requires the interpolation of the \mathbf{J} distributions in the non-analyzed tapes. As a complement to this strategy, a new interpolation method was developed. This method is based on the Inverse Cumulative Density Function (ICDF) interpolation method, originally presented in [35] and further developed in [107]. The description of the ICDF interpolation applied to the computation of the \mathbf{J} distributions in the non-analyzed tapes is presented in Appendix B. The ICDF interpolation produces more realistic \mathbf{J} distributions, avoiding some issues produced by the conventional linear interpolation. Both interpolation methods, ICDF and linear, were implemented in MATLAB[®] scripts which are called by a main script implementing the full iterative multi-scale algorithm.

4.1.2 Results

To validate the strategies, the model was simulated for one cycle of an 11 A, 50 Hz sinusoidal transport current. The convergence criterion is defined as $\varepsilon = 0.01$. This criterion is reached at the 7th iteration regardless of the interpolation method used to approximate the \mathbf{J} distributions in the non-analyzed tapes. Figure 4.2 presents the results for the 1st, 2nd, 3rd and 7th iterations, using the ICDF interpolation. The results of the reference model are also shown in the last row. The \mathbf{J}_n and $|\mathbf{B}|$ plots show the results at $t = 15$ ms. The average losses are given in the third column, the red circles in these plots indicate the position of the analyzed tapes.

The results of the first iteration, when the uniform current density is used, correspond to the results of the H multi-scale model presented in Figure 3.7. The screening currents appear in the second iteration, and with each iteration the results are closer to the results of the reference model presented in the last row.

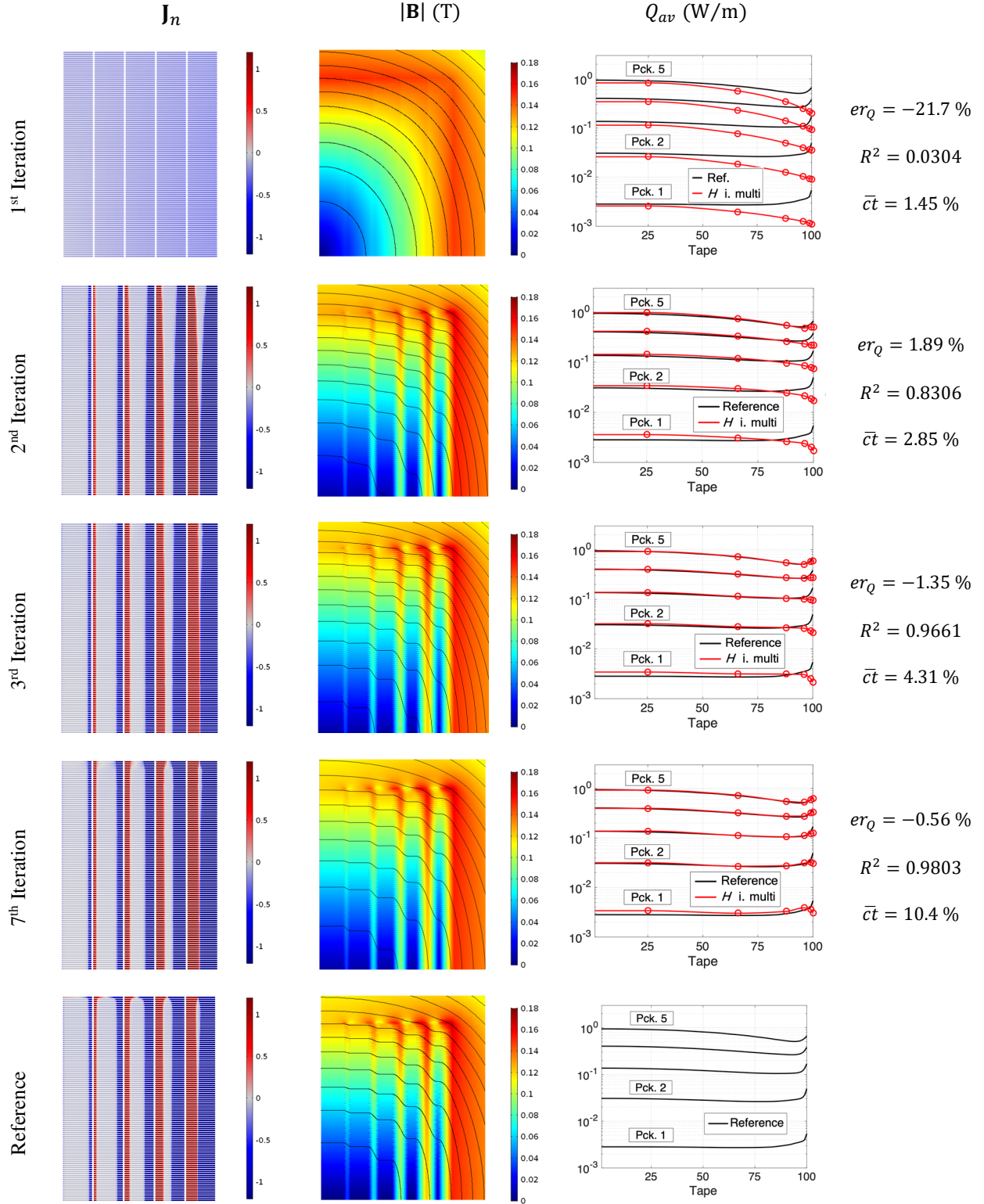


Figure 4.2. Results of the H iterative multi-scale model. The upper rows show the results for the 1st, 2nd, 3rd and 7th iterations. The first two columns present the results at the second peak of the transport current ($t = 15$ ms). The er_Q gradually approaches to zero, while R^2 approaches to 1. er_Q and R^2 , are defined in (3-2) and (3-3), respectively. The \mathbf{J}_n and $|\mathbf{B}|$ of the 7th iteration are indistinguishable from the reference results.

The evolution of the \mathbf{J} distribution is also clearly observed in Figure 4.3, where the \mathbf{J} distributions at $t = 5$ ms in the tape 100 of the pancake 5 for different iterations are shown together with the \mathbf{J} distribution estimated with the reference model. The results when the linear interpolation is applied to approximate the current density are visually indistinguishable to those obtained from the ICDF interpolation. For clarity, only the latter are shown in Figure 4.2 and Figure 4.3.

In Figure 4.2 it can be observed that the local accuracy of the losses at the central pancakes is lower than that of the outer pancakes, even when the accuracy improves with each iteration, there are visible differences at the 7th iteration. The reason for this behavior is that the \mathbf{J} distribution at the central pancake is affected by the \mathbf{J} distribution in the neighbor pancakes, i.e., pancake 2 and pancake 1 itself. While, in the case of pancake 5, there is no pancake on the right side, therefore the convergence is faster in this outer pancakes because it is not necessary to wait for an accurate \mathbf{J} distribution in the nonexistent pancake 6. Conversely, the losses in the tapes closer to tape 1 undergo a faster convergence than the ones surrounding tape 100. In these internal tapes the external field is more affected by the transport current than by the screening currents in the rest of the tapes. At the 7th iteration there are still local visible errors, especially in pancake 1. These errors can be reduced if more iterations are performed. However, the iterative process stops at the 7th iteration, because the local errors in pancake 1 do not have a significant impact in the current density error eJ_k . It is useful to recall that the plots of the losses in Figure 4.2 use logarithmic scale.

Figure 4.4 shows the loss error er_Q and the R^2 in \mathbf{J} distributions, as defined in (3-2) and (3-3), respectively. This plot compares the results at each iteration with those of the reference model. The results for the cases with both interpolation methods, ICDF and linear, are presented. Both black error curves start at $er_Q = -21.7\%$ and present an asymptotic behavior. The error at the 7th iteration when linear interpolation is used is -0.87% , while when ICDF interpolation is used this final value of the error is $er_Q = -0.56\%$. Again, the negative sign of the er_Q values means that the losses have been

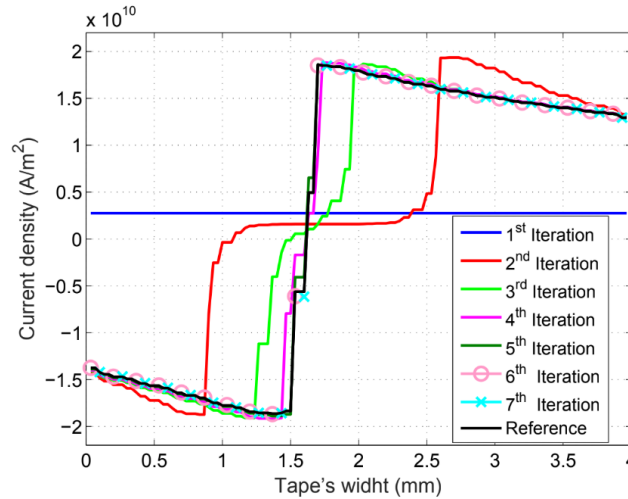


Figure 4.3. \mathbf{J} distribution in tape 100 of pancake 5, at the first peak of the transport current at $t = 5$ ms. The distribution evolves from a uniform distribution to a distribution that overlap with that of the reference model.

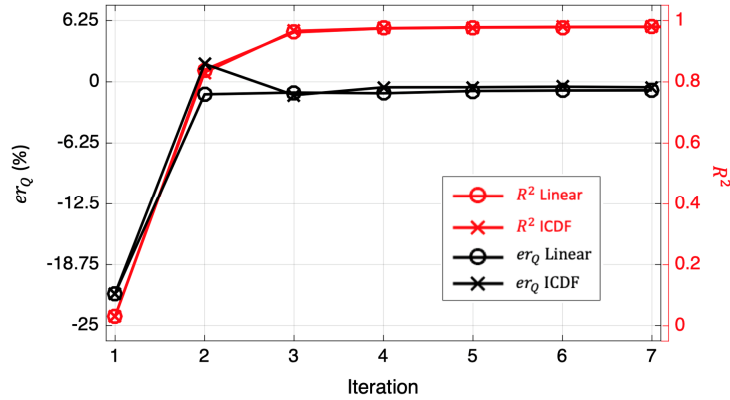


Figure 4.4. er_Q and R^2 values of the H iterative multi-scale model, at the different iterations. The negative sign of some er_Q values means that the losses have been underestimated.

underestimated. The red curves also present an asymptotic behavior, starting at $R^2 = 0.0304$, and reaching the values 0.9796 and 0.9803, for the cases with linear and ICDF \mathbf{J} interpolations, respectively. Figure 4.4 demonstrates that both interpolation methods produce almost the same results. Actually, the accuracy is marginally better with the ICDF interpolation. The tangible benefits are mostly present in the zones covering the moving fronts of the \mathbf{J} distribution. These zones cover a small fraction of the whole tapes leading to a negligible impact on the overall results.

The computation time required to complete one iteration with the H iterative multi-scale model is 27 min 30 s, i.e., the same time required by the H multi-scale model. The following iterations require additional time to complete the interpolation of the \mathbf{J} distributions, this time sums up to 60 s and to 30 s, for the ICDF and linear interpolations, respectively. Therefore, the total computation time required by the H iterative multi-scale model is 3 h 17 min (ICDF interpolation) and 3 h 21 min (linear interpolation) ($\bar{c}t = 10.33\%$ or $\bar{c}t = 10.51\%$), depending of the interpolation method.

4.2 Simultaneous Multi-Scaling

The multi-scale and the iterative multi-scale strategies use two different submodels. The coil submodel is used to compute the background magnetic field strength, and the single-tape submodel is used to compute the hysteresis losses and the \mathbf{J} distribution in the analyzed tapes. The simulations of the different analyzed tapes by means of the single-tape submodel can be parallelized, but these simulations can only be performed after the computation of the background magnetic field using the coil submodel. Therefore, the computation of the background field and the \mathbf{J} distributions is not carried out simultaneously.

Here, a new strategy called *simultaneous multi-scaling* is proposed. The simultaneous multi-scaling strategy allows solving simultaneously the current density in the analyzed tapes and the background field in the full system, therefore a predefined \mathbf{J} distribution is not required. The strategy relies on the

possibility to include an additional contribution in Ampère's law (2-10). This summand allows imposing an external current density \mathbf{J}_e in the superconducting subdomains Ω_{sc} of the non-analyzed tapes, as follows,

$$\nabla \times \mathbf{H} = \mathbf{J} + \mathbf{J}_e. \quad (4-2)$$

Considering Faraday's law (2-9) and the constitutive relations (2-4) and (2-5), the governing equation of the H formulation is then expressed as,

$$\nabla \times (\rho(\nabla \times \mathbf{H} - \mathbf{J}_e)) = -\mu \frac{\partial \mathbf{H}}{\partial t}. \quad (4-3)$$

The external \mathbf{J}_e in the superconducting subdomains Ω_{sc} of the analyzed tapes and in the surrounding medium subdomain Ω_{sm} is zero. The external \mathbf{J}_e in the superconducting subdomains Ω_{sc} of the non-analyzed tapes is approximated by interpolating the \mathbf{J} distributions of the analyzed tapes.

The resistivity in the superconducting subdomains Ω_{sc} of the analyzed tapes is defined by the power-law (2-4) and the Kim-like (2-5) models. The resistivity of the superconducting subdomains Ω_{sc} of the non-analyzed tapes is considered to be the resistivity of the surrounding medium proposed in [22], i.e., $\rho_m = 1 \Omega\text{m}$. This value is orders of magnitude larger than the resistivity of the superconducting subdomains, therefore the induced current density in the non-analyzed tapes has a negligible impact when compared with the external \mathbf{J}_e .

It is possible to further reduce the number of DOF, and therefore the computation time of the H simultaneous multi-scale models, by means of the homogenization of the non-analyzed tapes. The external \mathbf{J}_e imposed in the homogeneous bulks modeling the non-analyzed tapes is the interpolated \mathbf{J} distribution multiplied by f_{HTS} (the ratio between the cross-section of all the HTS layers and the cross-section of the bulk).

4.2.1 H Simultaneous Multi-Scale Models

Two H simultaneous multi-scale models of the case study are subsequently presented. Both models use the set of analyzed tapes previously considered for the multi-scale models. The first model considers the non-analyzed tapes with their original geometry, this model is called *H simultaneous multi-scale model*. The second model, called *H simultaneous multi-scale homogenous model*, results from the combination of the multi-scaling and homogenization strategies. This latter model considers the same set of analyzed tapes of the multi-scale models, and most of the non-analyzed tapes are homogenized. Not all the non-analyzed tapes are homogenized, the non-analyzed tapes adjacent to the analyzed tapes keep their original shape. These non-homogenous non-analyzed tapes establish greater distance between the analyzed tapes and the distortions in the magnetic field produced by the homogeneous non-analyzed tapes. The geometries of these two multi-scale models are presented in Figure 4.5.

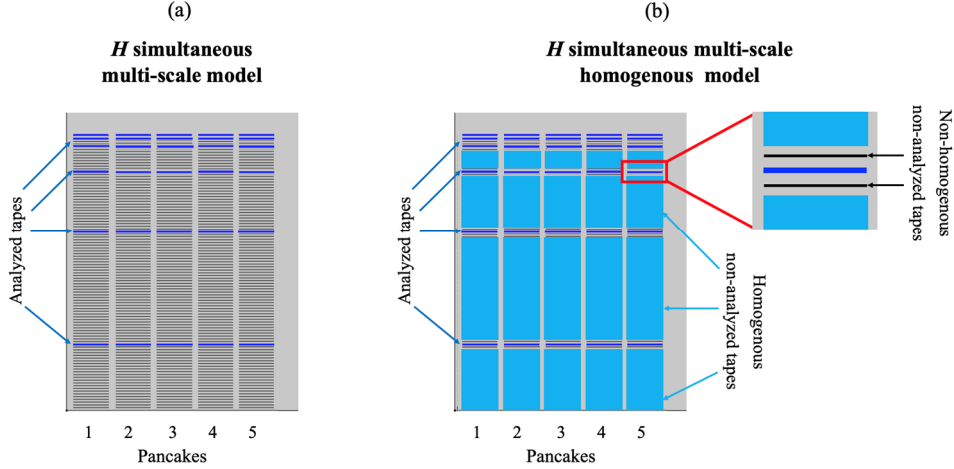


Figure 4.5. (a) geometry of the H simultaneous multi-scale model. (b) geometry of the H simultaneous multi-scale homogenous model, most of the non-analyzed tapes are homogenized.

The implementation ICDF interpolation requires the computation of integrals, derivatives and inverse functions. In the H iterative multi-scale model, this method is implemented in a MATLAB script. The H simultaneous multi-scale models were implemented in a single COMSOL model, and for convenience just the simpler linear interpolation was used. This is not a major drawback, because as demonstrated in Figure 4.4, the ICDF interpolation makes only a marginal contribution to the accuracy of the model.

4.2.2 Results

The simultaneous multi-scale models were also simulated for one cycle of an 11 A, 50 Hz sinusoidal transport current. Figure 4.6 shows the results of these models together with those of the reference model. As in the previous sections, \mathbf{J}_n and $|\mathbf{B}|$ show the results at the second peak of the transport current ($t = 15$ ms). The \mathbf{J}_n plot of the second row clearly shows the homogenous regions inside the pancakes, and also a smoother magnetic flux density is observed in the homogeneous regions.

The relative errors of the losses are $er_Q = 1.57\%$ and $er_Q = 0.72\%$, for the H simultaneous multi-scale and the H simultaneous multi-scale homogenous models, respectively. The R^2 values reveal that both models have almost the same accuracy, with values equal to 0.9818 and 0.9833, for the H simultaneous multi-scale and the H simultaneous multi-scale homogenous models, respectively. The advantage of the homogenization of the non-analyzed tapes is clearly observed in the computation time. The computation times are 16 h 56 min ($\bar{c}t = 53.7\%$) for the H simultaneous multi-scale, and 8 h 41 min ($\bar{c}t = 27.5\%$) for the H simultaneous multi-scale homogenous models, respectively.

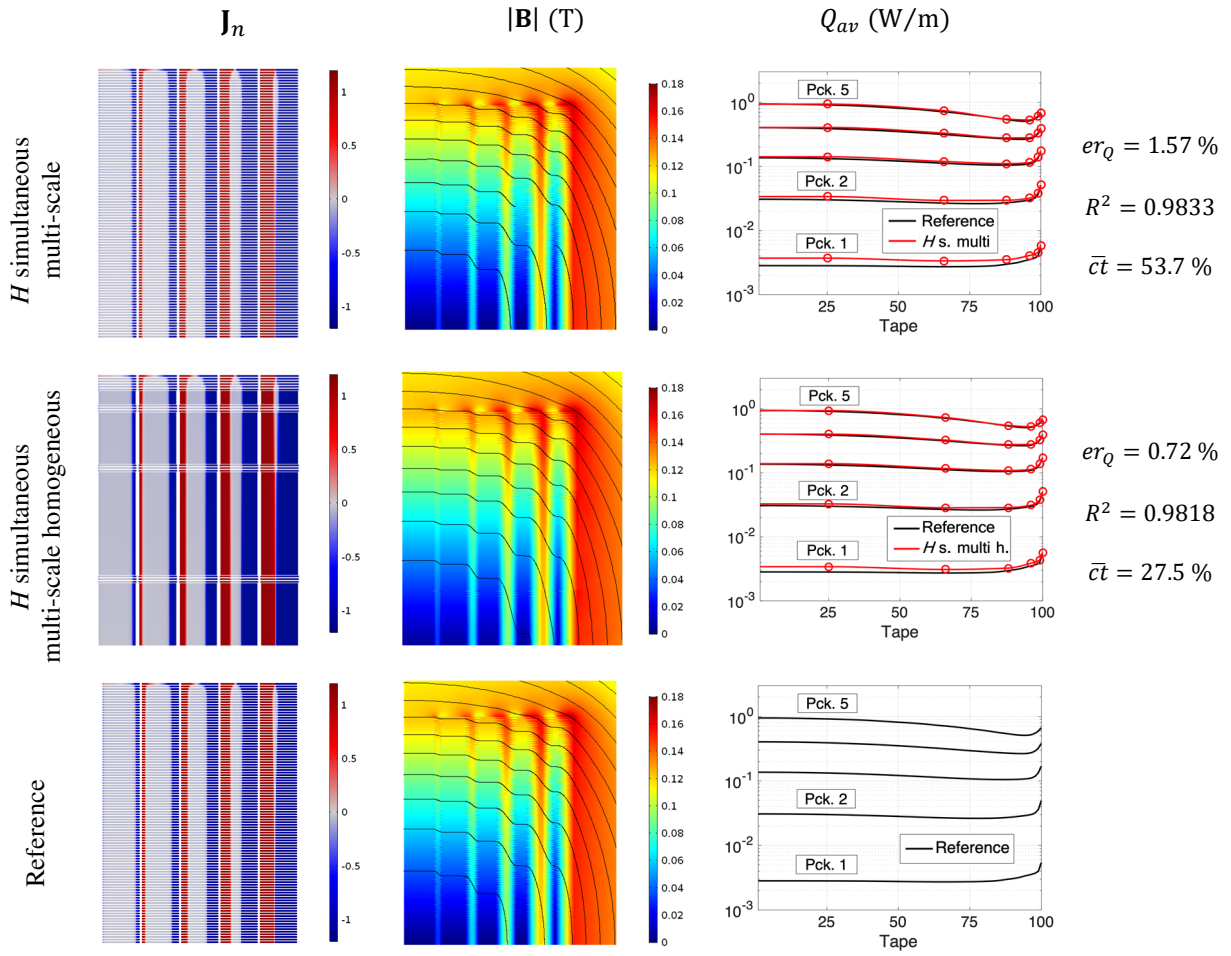


Figure 4.6. Results of the H simultaneous multi-scale and H simultaneous multi-scale homogeneous models. The first two columns present the results at the second peak of the transport current ($t = 15$ ms).

Chapter 5 *T-A* Formulation Strategies

In this chapter the multi-scaling and homogenization approaches are adapted to be used in conjunction with the *T-A* formulation. Before describing the *T-A* multi-scaling and *T-A* homogenous strategies, an additional approach, referred to as *T-A densified*, is presented hereinafter. These strategies make use of less resources, compared with the *T-A* full strategy, while obtaining similar accuracies. These three strategies are additional original contributions of this work.

5.1 Densification

The multi-scaling strategies, described in the previous chapters, use a reduced set of analyzed tapes. The *densification* strategy proposed here also address the analysis of the systems made of stacks of tapes by means of a reduced number of tapes, here called *densified tapes*. Each densified tape represents a given number of tapes, therefore there are no such concepts as analyzed and non-analyzed tapes.

The densified tapes are one-dimensional objects along which the \mathbf{J} distributions are computed by means of the current density potential \mathbf{T} and its only non-zero component T_y , as given in equations (2-23) and (2-24). In the original *T-A* formulation, the surface current density $\mathbf{K} = \delta\mathbf{J}$ is imposed into the *A* formulation, see equations (2-27) and (2-29). To take into account the densification of the tapes, this surface current density is now defined as,

$$\mathbf{K}_d = d(\delta\mathbf{J}), \quad (5-1)$$

where d is the number of tapes merged into a single densified tape.

The densification process is depicted in Figure 5.1. In the example, the densified tape is built out of 3 tapes, labelled $r - 1$, r and $r + 1$, therefore $d = 3$. The densified tape is located at the position of the tape number r . The densification process involves two steps. The first step is to remove the tapes

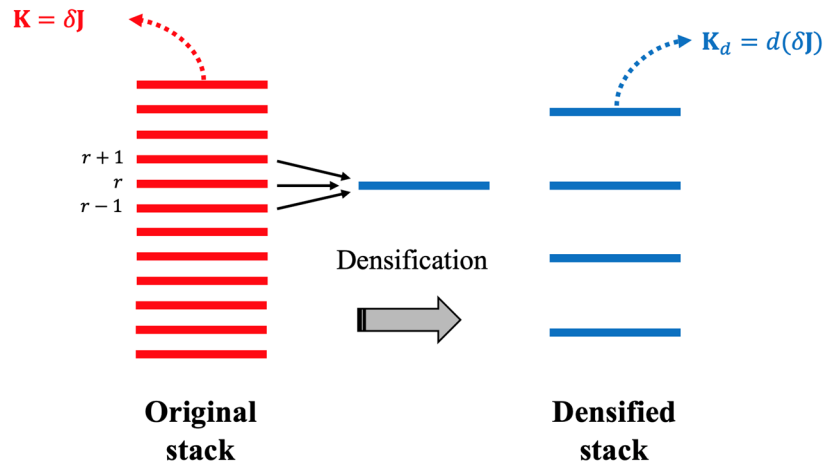


Figure 5.1. Densification process, the number of tapes in the stack is reduced and the magnetic effect of the densified tapes is artificially increased.

$r - 1$ and $r + 1$. Second, the magnetic effect of tape r is forced to be three time larger than the magnetic effect of the same tape in the full model. The increment of the magnetic effect of the densified tapes is implemented by means of the parameter d in equation (5-1), while the transport current in the densified tape remains the same as the transport current in original tape, see equation (2-26). Therefore, the original stack can be modeled by means of a stack of densified tapes, and the number of densified tapes is lower than the number of tapes in the original stack.

It should be mentioned that it is not necessary for the parameter d to be an integer number, like in the example depicted in Figure 5.1. The parameter d may be equal to other real positive number. This feature is useful, for example, when a stack made of 5 tapes is going to be modeled by means of 2 densified tapes. In this case, the densified tapes may merge 3 and 2 tapes, respectively, But in another possible scenario, the densified tapes may merge 2 tapes and a half each one, then the parameter d should be $d = 2.5$.

Once the \mathbf{J} distribution is computed, the hysteresis losses can be calculated in the densified tapes. These losses are considered as the losses produced by the tapes of the original stack in the position of the densified tapes. The losses in the rest of the tapes, those that were removed in the densification process, are interpolated from the losses in the densified tapes.

The densification strategy cannot be applied together with the H formulation. The reason for this is that, due to the use of edge elements, as described in Section 2.5.1, it is not possible to impose surface current densities into an H formulation model. The densification strategy, as presented here, relies on the possibility to impose the surface current density \mathbf{K}_d , see equation (5-1).

5.1.1 *T-A* Densified Model

The model of the case study applying the densification strategy described in this chapter is called *T-A densified model*. The *H* multi-scale models, which were presented in the previous chapters, use the same set of analyzed tapes per pancake, i.e., {25, 66, 88, 96, 99, 100}. For the purpose of a fair comparison between models, the *H* homogenous model has six subsets per pancake, and the distribution of these subsets is analogue to the set of analyzed tapes. However, the choice of this set, as a set of densified tapes, leads to inaccurate results. For instance, in the above-mentioned set the densified tape 25 should merge tapes 1 to 50, covering a non-negligible portion of the stacks leading to a large error in the estimation of the local magnetic field. The field would be overestimated around the densified tape that concentrates the effect of fifty tapes. The same issue would be found for the remaining densified tapes. Hence, a large separation between densified tapes should be avoided.

Different sets of densified tapes were tried, our yardstick is that the compromise between accuracy and computation time is fulfilled with a set of 31 densified tapes. The geometry of the model and the position of the densified tapes is depicted in Figure 5.2. The first twenty densified tapes represent four tapes each ($d = 4$). For the following five tapes, the parameter d takes the values {3.5, 3, 2.5, 2, 1.5}, respectively. Finally, the upper six tapes densified tapes represent just one tape, ($d = 1$). The denser distribution of densified tapes at the upper part of the pancake allows achieving the required accuracy in the regions with larger variations in the **J** distributions.

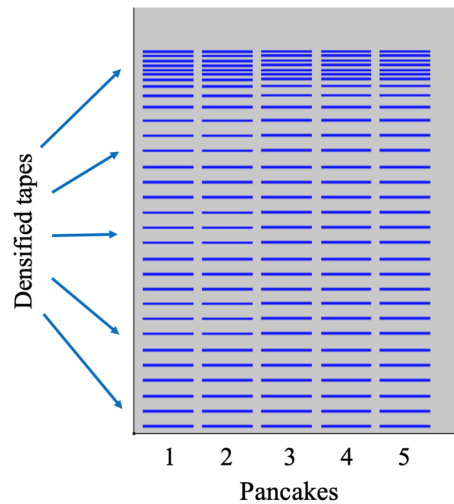


Figure 5.2. Geometry of the *T-A* densified model. There are 31 densified tapes in each pancake. A larger number of densified tapes is considered in the upper portions of the pancakes.

5.1.2 Results

The strategies described in this chapter are validated using the same operating conditions presented in the previous chapters, a sinusoidal transport current with amplitude equal to 11 A, and a frequency equal to 50 Hz. The simulation results are shown in Figure 5.3. In the \mathbf{J}_n plots, the thickness of the lower densified tapes has been increased to reduce the empty spaces and facilitate the comparison with the reference results. It should be remembered that, as in the T - A full model, the densified tapes are 1D objects. Due to the nature of the densified tapes, larger self-fields and larger distances between tapes lead to the distortion in the magnetic field surrounding the densified tapes. The average losses are very similar to the reference losses. A denser the distribution of densified tapes at the upper section of the pancakes allows a more accurate reproduction of the losses curves.

The total average losses are slightly underestimated by the T - A densified model, having a value of $Q_{av} = 124 \text{ W/m}$ instead of $Q_{R_{av}} = 127.24 \text{ W/m}$ of the reference model. The relative error takes the value $er_Q = -2.62 \%$. The discrepancy originates from the losses in the lower sections of the pancakes where a lesser number of densified tapes is considered.

The computation of R^2 as defined in (3-3) requires the knowledge of the current density in all the tapes, however, the T - A densified model computes the \mathbf{J} distributions just in the densified tapes. For the purpose of obtaining the current density in all the tapes and computing R^2 , the \mathbf{J} distributions in the tapes that were removed are interpolated from the \mathbf{J} distributions of the densified tapes. The

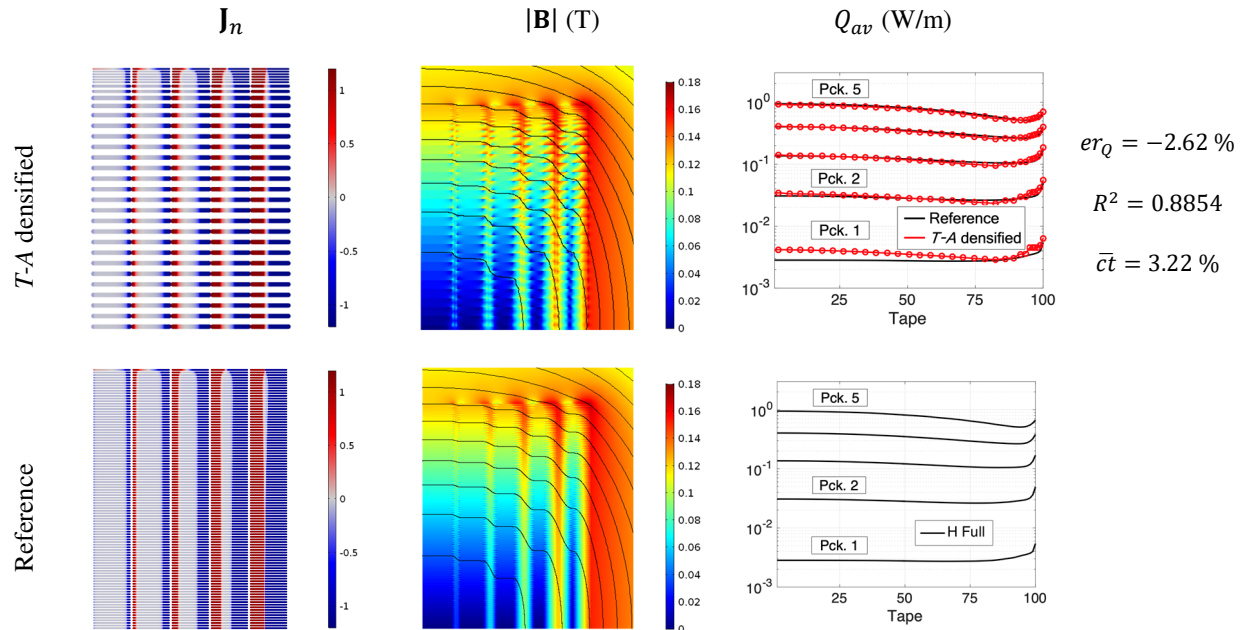


Figure 5.3. Results of the T - A densified model. The \mathbf{J}_n and $|\mathbf{B}|$ show the results at the second peak of the transport current ($t = 15 \text{ ms}$). For easier visualization, thicker lines are used to represent \mathbf{J}_n in the densified tapes at the bottom of the stacks.

computed value is $R^2 = 0.8854$. This value indicates that this approach does not compute accurately the current density distribution in all the tapes as well as the local magnetic field; however, it remains an acceptable strategy for estimating the losses.

The computation time required to complete the simulation with the T - A densified model is 61 min ($\bar{c}t = 3.22\%$), approximately one third of the computation time required by the T - A full model.

5.2 Simultaneous Multi-Scaling

The T - A simultaneous multi-scaling strategy proposed here, as well as the strategy proposed in Section 4.2, does not require two different submodels. The computation of the background magnetic field and the \mathbf{J} distribution are carried out in a single model based on the T - A formulation.

In the T - A full models, the current vector potential \mathbf{T} is defined over all the tapes. In the present approach, \mathbf{T} is defined only along the analyzed tapes. The \mathbf{J} distribution along the analyzed tape is obtained by calculating \mathbf{T} , see equations (2-23) and (2-24). The \mathbf{J} distributions in the non-analyzed tapes are approximated by linear interpolation using the \mathbf{J} distributions of the analyzed tapes. The

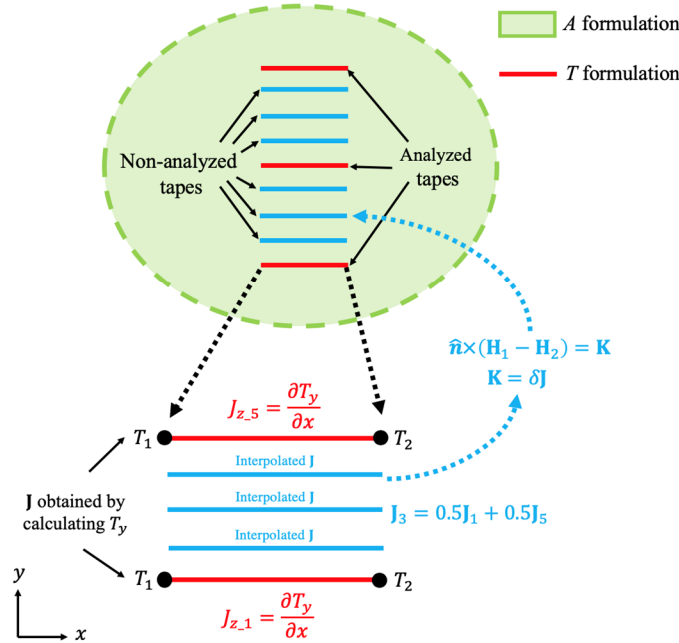


Figure 5.4. T - A simultaneous multi-scale strategy. In this example three analyzed tapes are considered. The \mathbf{J} distributions in the non-analyzed tapes are approximated by linear interpolation. The thickness of the superconducting layer is δ and \mathbf{K} is the surface current density that is imposed into the A formulation. $\hat{\mathbf{n}}$ is the unit vector normal to the tape. \mathbf{H}_1 and \mathbf{H}_2 are the magnetic field strength vectors above and below the superconducting layer, respectively.

magnetic flux density \mathbf{B} is obtained by calculating the curl of the magnetic potential \mathbf{A} , which is defined over the entire bounded universe and is given by (2-27). The current density in both analyzed and non-analyzed tapes is multiplied by the thickness of the superconducting layer δ to obtain a surface current density \mathbf{K} to be imposed into the A formulation, see equations (2-27) and (2-29). Figure 5.4 shows this multi-scale approach applied to a small stack.

As it was the case with the H simultaneous multi-scale models, the DOF can be reduced by means of the homogenization of the non-analyzed tapes. Alternatively, in the T - A multi-scale models the DOF can also be reduced by the densification of the non-analyzed tapes.

5.2.1 T - A Simultaneous Multi-Scale Models

Three T - A *simultaneous multi-scale* models of the case study are presented here. The difference between these models is the treatment of the non-analyzed tapes. The three models use the same set of 6 analyzed tapes per pancake used in the H multi-scale models. The first model, called *T - A simultaneous multi-scale*, considers the non-analyzed tapes with their original number and geometry.

The T - A formulation uses first order elements to approximate \mathbf{T} and second order elements to approximate \mathbf{A} . If first order elements are used for both quantities, the computation time can be reduced [34], but this choice produces undesired spurious oscillations in the \mathbf{J} distribution, as discussed in Appendix A.

To increase the computational efficiency of the model without compromising the accuracy, the unit cells of the analyzed tapes and their adjacent non-analyzed tapes use second order elements to approximate \mathbf{A} , while first order elements are used to approximate \mathbf{A} throughout the rest of the system. The domains using first and second order elements are connected by means of Dirichlet boundary conditions. A further reduction of the DOF is achieved by considering 30 elements along most of the non-analyzed tapes, while 60 elements are considered in the analyzed tapes and their adjacent non-analyzed tapes. The analyzed tapes, the domains using second order elements for \mathbf{A} and the mesh are shown in Figure 5.5.

The other two T - A multi-scale models simplify the geometric description of the pancakes by means of the densification or homogenization of the non-analyzed tapes. These models are called *T - A simultaneous multi-scale densified* and *T - A simultaneous multi-scale homogenous* models, respectively. As it was done in Section 4.2.1, the non-analyzed tapes adjacent to the analyzed tapes keep their original geometry to establish greater distance between the analyzed tapes and the distortions in the magnetic field produced by the densified or homogenized non-analyzed tapes. The geometries of the T - A multi-scale models are depicted in Figure 5.6.

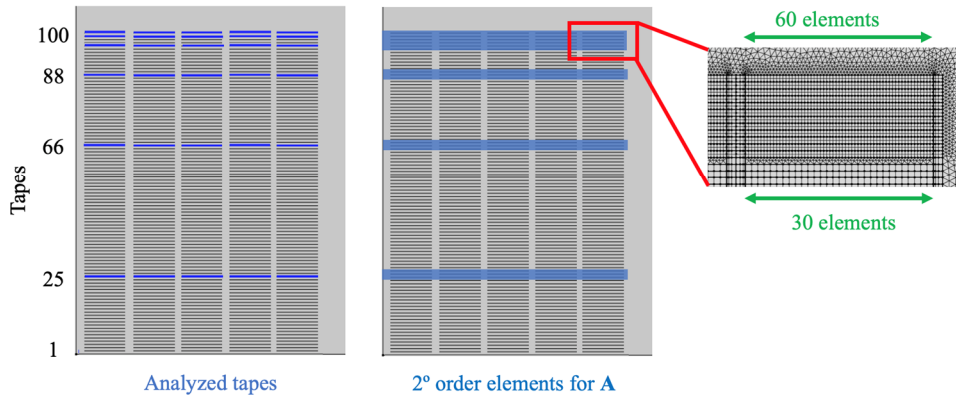


Figure 5.5. Geometry and mesh of the T - A simultaneous multi-scale model. The analyzed tapes and their adjacent non-analyzed ones use second order elements for \mathbf{A} . The mesh considers 60 elements along the analyzed tapes and their adjacent non-analyzed tapes, while 30 elements are considered along the rest of the tapes.

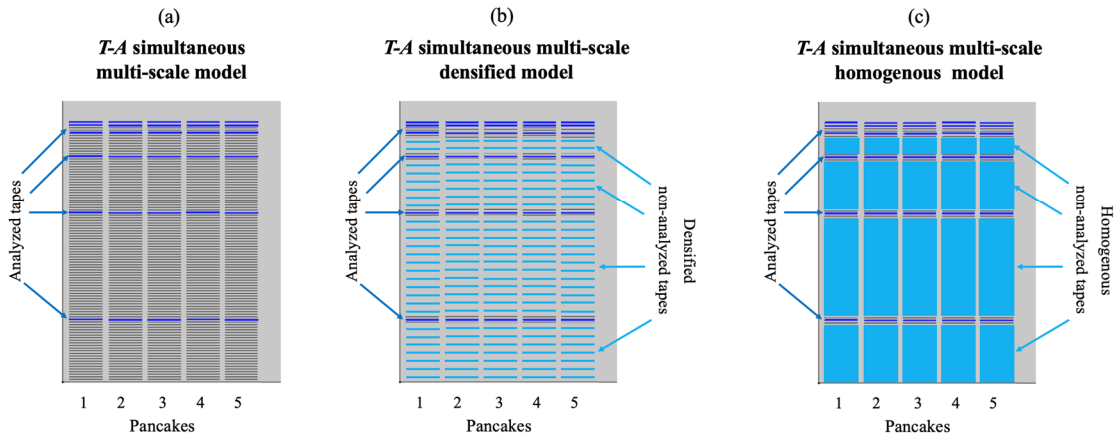


Figure 5.6. Geometry of the T - A multi-scale models. In the T - A simultaneous multi-scale model all the tapes retain their original geometry. In the other models most of the tapes are either densified or homogenized.

5.2.2 Results

The three T - A simultaneous models are validated using the same operating conditions used to validate the previous models, i.e., sinusoidal transport current, amplitude of 11 A and frequency of 50 Hz. The simulation results are presented in Figure 5.7. The first column shows the \mathbf{J}_n plots. It is possible to appreciate thicker lines representing the densified tapes in the second row and the bulks representing the homogenized tapes in the third row. As shown in the second column, the $|\mathbf{B}|$ calculated with the T - A simultaneous multi-scale model is very similar the one calculated with the reference model.

However, the $|\mathbf{B}|$ calculated with the T - A simultaneous multi-scale homogenous and densified models show local variations with respect to the reference model.

An accurate estimation of the hysteresis losses is achieved with the three T - A simultaneous multi-scale models. In the three cases, the magnitude of the relative error of the losses is less than 1 %. Also, the \mathbf{J} distributions are accurately estimated: the R^2 values for the T - A simultaneous multi-scale

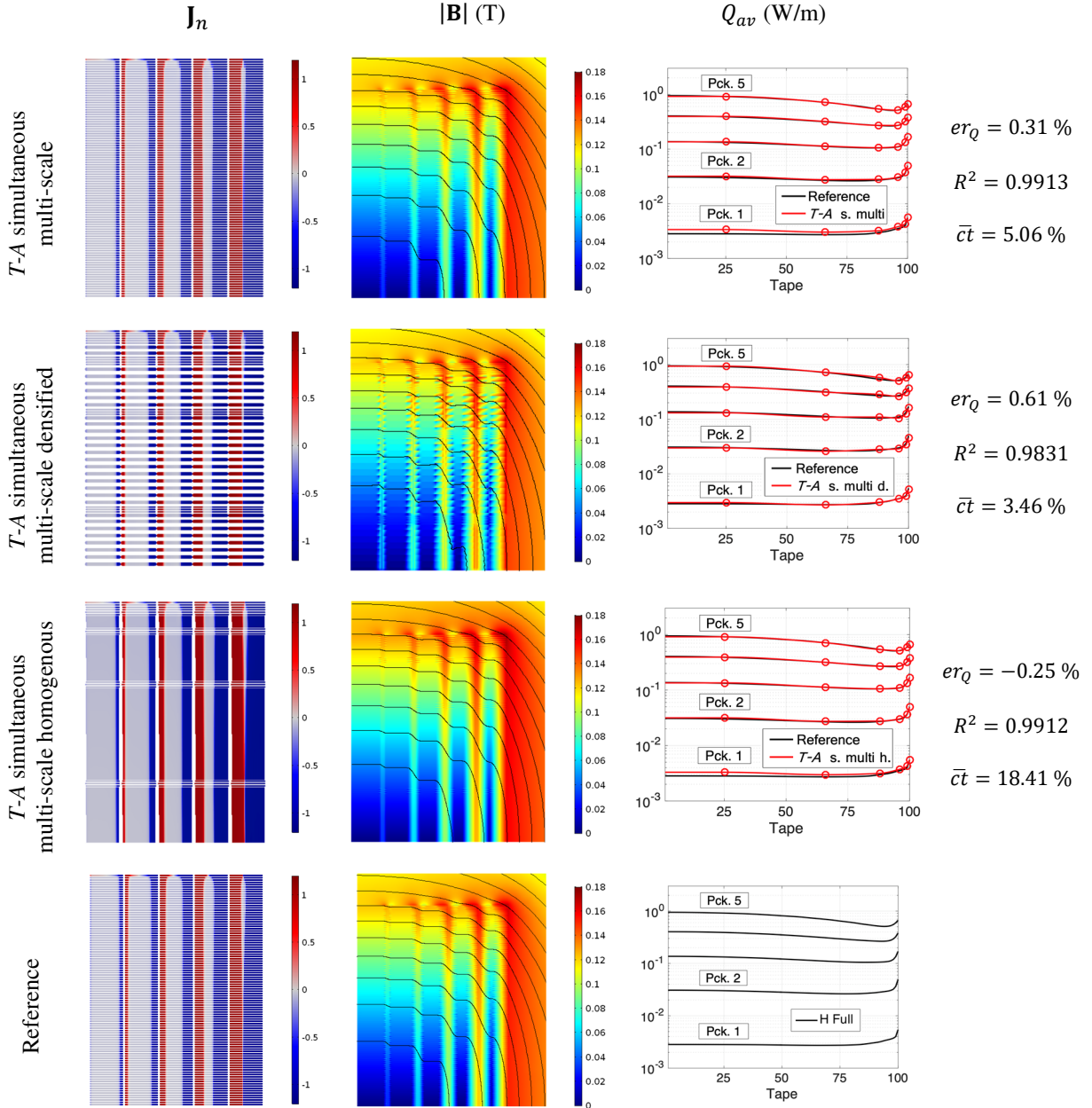


Figure 5.7. Results of the T - A simultaneous multi-scale models. The \mathbf{J}_n and $|\mathbf{B}|$ plots show the results at the second peak of the transport current ($t = 15$ ms). The three multi-scale models use the usual set of 6 analyzed tapes per pancake.

and the T - A simultaneous multi-scale homogenous are greater than 0.99. The densification of the non-analyzed tapes causes just a slight reduction of the R^2 to a value of 0.9831.

The computation time required to complete the simulation with the T - A simultaneous multi-scale model is 1 h 35 min ($\bar{c}t = 5.06\%$). The computation time required by the T - A simultaneous multi-scale densified model is 1 h 5 min ($\bar{c}t = 3.46\%$), i.e., 30 min quicker than the computation time of the T - A simultaneous multi-scale model. The homogenization of the non-analyzed tapes reduces the DOF, but produces a noticeable increment of the computation time. Unlike the H simultaneous multi-scale models, here the homogenization of the non-analyzed tapes does not lead to the reduction of the computation time. The computation time required by the T - A simultaneous multi-scale homogenous model is 5 h 48 min ($\bar{c}t = 18.41\%$), approximately four times larger than the computation time of the T - A simultaneous multi-scale model.

5.3 Homogenization

As described in Section 2.6.2, the homogenization strategy models a stack of HTS tapes as a homogeneous anisotropic bulk that preserves the overall electromagnetic properties of the HTS tapes in the stack.

The homogenization process coupled with the T - A formulation is depicted in Figure 5.8. Once again, the magnetic vector potential \mathbf{A} is defined all over the entire bounded universe. After the homogenization, the tapes that were previously 1D objects are now 2D bulks, and the potential \mathbf{T} is now exclusively defined inside the bulk. Following the assumptions that belongs to the T - A formulation as described in Section 2.5.2, for the purpose of computing \mathbf{T} inside the bulk, the influence of the component of \mathbf{B} parallel to the surface of the tapes B_x is not considered. Therefore, from equation (2-20), it follows that \mathbf{T} has only one non-zero component. In the stack depicted in Figure 5.8, this non-zero component is T_y . As in the non-homogenous case, T_y is defined by means of equation (2-24).

The homogenous bulk can be understood as the limiting case of a densely packed stack where the thickness of the HTS layer of the tapes is increased to the point that the air gaps disappear. The resistivity of the layers of copper and other non-superconducting layers forming part of the HTS tapes are several orders of magnitude larger than the resistivity of the superconducting layer [22]. Hence, these layers are not considered. The resistivity of the bulk subdomains, for the purpose of computing \mathbf{T} , is considered to be the resistivity of the superconducting material, which is derived from the power-law (2-4) and Kim-like models (2-5).

Each tape of the densely packed stack (homogenous bulk) should carry the same transport current of the actual physical tape. To impose such transport current, it is necessary to define the values T_1 and T_2 to be used as boundary conditions along the edges of the bulks perpendicular to the tapes, in the case of Figure 5.8 these edges are the vertical ones. The values T_1 and T_2 are defined by means of the following relation: $I_k = (T_1 - T_2)\delta$, which is the same relation presented in equation (2-26), and where I_k is the transport current in each tape and δ is the real thickness of the HTS layer.

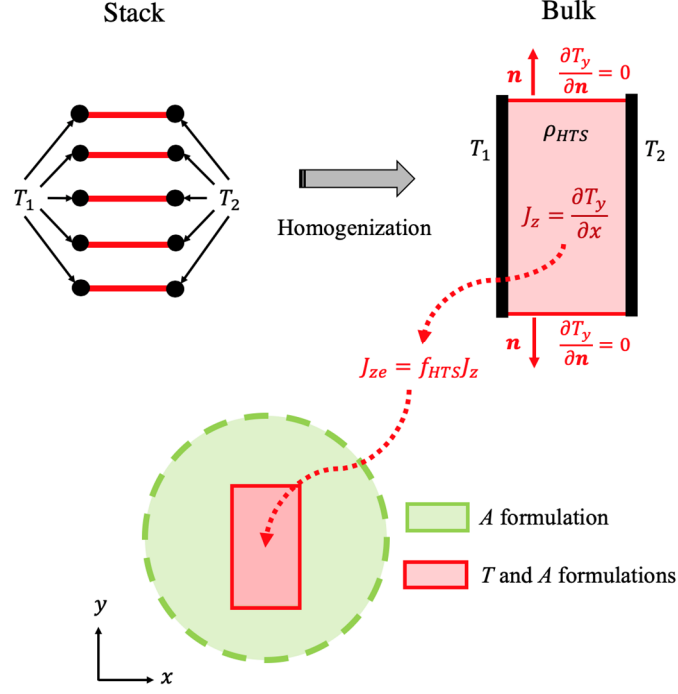


Figure 5.8. *T-A* homogeneous strategy. **A** is defined all over the entire bounded universe and **T** is exclusively defined inside the bulk. The influence of B_x is neglected, therefore T_y is the only component of **T**. The boundary conditions T_1 and T_2 are applied to the vertical edges of the bulk. The engineering current density J_{ze} is imposed into the *A* formulation.

The boundary conditions on the edges parallel to the 1D tapes, upper and lower edges in Figure 5.8, are Neumann boundary conditions of the form,

$$\frac{\partial T_y}{\partial \mathbf{n}} = 0 \quad (5-2)$$

where \mathbf{n} represents the unit vector normal to the corresponding edge.

The current density inside the bulk has one component defined by $J_z = \partial T_y / \partial x$, as in equation (2-23). To compensate for the fact that J_z is the current density in a tape whose thickness has been increased to form the homogenous bulk, a new engineering current density J_{ze} is defined as,

$$J_{ze} = f_{HTS} J_z \quad (5-3)$$

where f_{HTS} is the ratio between the real thickness of the HTS layer δ and the thickness of the unit cell Δ , see equation (2-32). Then J_{ze} is imposed in the bulk subdomain as a source term in the governing equation of the *A* formulation, then equation (2-27) is transformed into,

$$\nabla^2 A_z = -\mu J_{ze}. \quad (5-4)$$

5.3.1 *T-A* Homogeneous Model

The *T-A homogeneous* model of the case study considers 5 bulks, one for each pancake. The mesh in the bulk subdomains is structured considering 6 unequal elements along the bulk's height. The distribution of the elements is the same distribution of the bulk subsets in the *H* homogenous model, as depicted in Figure 3.6. The distribution of the elements along the bulk's height is analogue to the distribution of the analyzed tapes in the multi-scale models. The geometry and mesh of the *T-A* homogenous model is shown in Figure 5.9.

In contrast with what was considered in the *H* homogenous model, where the losses are computed by integrating the local losses in the whole bulks [22], the hysteresis losses in the *T-A* homogenous model are computed by integrating the local losses along the lines parallel to the HTS layers at the center of each of the 6 bulk's elements. The losses, corresponding to the tapes located at the center of the 6 elements, are used to approximate by interpolation the losses along the rest of the tapes. If the losses are integrated in the whole bulk, the variations on J_c at the extremities of the 6 bulk's elements produce a drastic increment of the local losses at these extremities. Consequently, by interpolating the losses as described above, it is possible to avoid numerical artifacts.

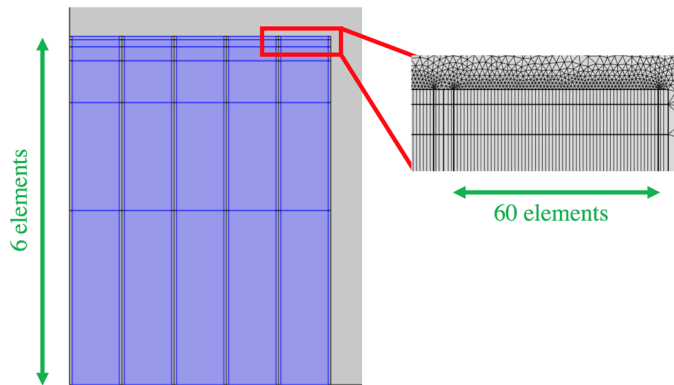


Figure 5.9. Geometry and mesh of the *T-A* homogeneous model. The bulk's mesh considers 6 elements along the bulks, with a denser distribution of elements in the upper sections of the pancakes.

5.3.2 Results

The *T-A* homogeneous model is validated considering the same conditions used to validate the previous models. The results are shown in Figure 5.10. As in the previous sections, the results of the reference model are presented to facilitate comparisons. The \mathbf{J}_n plots are presented in the first column; the solid blocks in the first row represent the homogenous bulks. Due to the homogenization process, a smoother magnetic field is observed in the *T-A* homogenous results than in the reference results.

In the plot at the first row of Figure 5.10, it is possible to observe that the losses in the pancake 1 estimated with the T - A homogenous model deviate from the reference results. The losses in the first pancake are two orders of magnitude lower than those of the pancake 5, therefore the deviation does not affect the global result. The total losses are slightly overestimated, the computed value equal to $Q_{av} = 128.14$ W/m, then the relative error is $er_Q = 0.71$ %.

The R^2 of the \mathbf{J} distributions is 0.9214, this value is lower than the values reached by the T - A multi-scale models, but is almost equal to $R^2 = 0.9221$, the value obtained with the H homogenous model. This shows a systematic degradation in the accuracy of the current density due to the homogenization process. Even when the homogenous model estimates the \mathbf{J} distribution all over the homogeneous bulks, the R^2 value is computed considering just the values at the positions of the original superconductor subdomains.

The computation time required by the T - A homogenous model is 14 min 51 s ($\bar{c}t = 0.78$ %). It is therefore the fastest model of all the models outlined in this work.

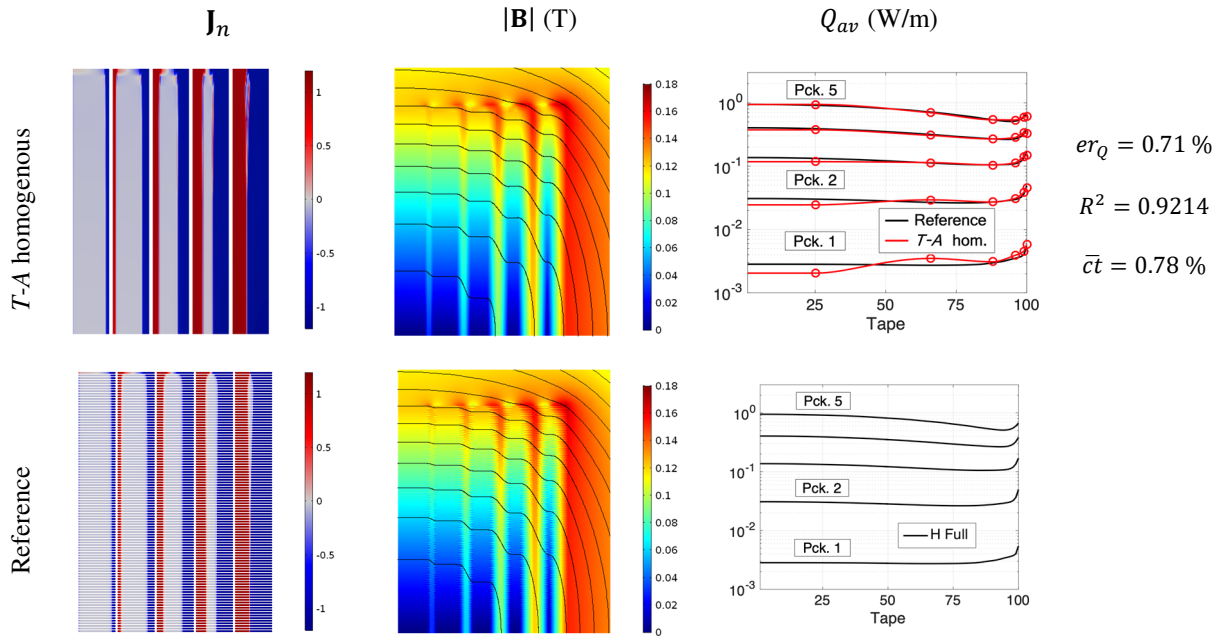


Figure 5.10. Results of the T - A homogeneous model. The \mathbf{J}_n and $|\mathbf{B}|$ plots show the results at the second peak of the transport current ($t = 15$ ms). The computation time required by this model is the lowest.

Chapter 6 Comparison

The comparison of the models of the case study introduced in Section 3.1 is presented in this chapter. For ease of comparison, the results, already presented in previous chapters, are brought together to infer which is the most efficient strategy for large-scale applications. Additionally, the number of DOF of each model are presented.

Table 6-1 shows the relative error of the average losses, er_Q , the coefficient of determination R^2 of the \mathbf{J} distributions, the normalized computation time $\bar{c}t$, and the number of DOF of all the models of the case study. Also, the results of the reference model are presented at the top of Table 6-1. The averaging nature of er_Q makes it not the best metric for the accuracy of the models, this is the reason why the R^2 is also taken into account.

The first comparison, arising from Table 6-1, is the comparison between the reference and the H full models. As described in Section 3.2, the reference model uses the H formulation and considers in detail all the tapes. The differences between the reference and the H full model are the number of elements along the tape's width and their distribution. The reference model considers 100 elements with a denser distribution of elements at the edges of the tape, while the H full model considers 60 elements and a uniform distribution. The reduction in the number of elements along the tape's width causes the reduction of the number of DOF and the computation time. The reduction in the DOF is approximately of the same magnitude of the reduction in the number of elements, while the computation time is reduced by a factor of about two.

The model with the highest number of DOF and the largest computation time is the reference model. The models with the lowest number of DOF are the single-tape submodels of the H multi-scale and H iterative multi-scale models. The coil submodel has more DOF, but their associated computation is equal to 5 min which is irrelevant compared to the overall computation time, see Section 3.4.3. Hence, the computation time of the H multi-scale model is mostly determined by the size of the single-tape submodel and the number of analyzed tapes. In the case of the H iterative multi-scale model, the computation time is also determined by the number of iterations, which for this case study is 7. Therefore, the computation time of the H iterative multi-scale model is approximately seven

Table 6-1. Models comparison.

Model	Losses (W/m)	Comp. time (h)		DOF
Reference	127.24	31 h 32 min		563893
Model	er_Q (%)	R^2	$\bar{c}t$ (%)	DOF
<i>H</i> full	1.62	0.9848	55.81	359408
<i>H</i> multi-scale	-21.7	0.0302	1.45	cs-112752, st-709 *
<i>H</i> iterative multi-scale	-0.56	0.9803	10.41	cs-112752, st-709 *
<i>H</i> simultaneous multi-scale	1.57	0.9833	53.70	359408
<i>H</i> sim. multi-scale homogeneous	0.72	0.9818	27.54	66752
<i>H</i> homogenous	1.28	0.9221	1.94	11838
<i>T-A</i> full	0.64	0.9922	10.25	548624
<i>T-A</i> densified	-2.62	0.8854	3.22	103638
<i>T-A</i> simultaneous multi-scale	0.31	0.9913	5.06	114582
<i>T-A</i> sim. multi-scale densified	0.61	0.9831	3.46	112853
<i>T-A</i> sim. multi-scale homogeneous	-0.25	0.9912	18.41	107529
<i>T-A</i> homogenous	0.71	0.9214	0.78	20612

* The abbreviation cs stands for the DOF of the coil submodel, and the abbreviation st stands for single-tape submodel.

times larger than the computation time of the *H* multi-scale model, even when they share the same single-tape and coil submodels.

Despite the repeated use of the single-tape submodel, the *H* multi-scale model is the one with the lowest computation time among the models using the *H* formulation. However, the accuracy of the *H* multi-scale model is the lowest ($er_Q = -21.7\%$, $R^2 = 0.0304$). The other models have errors that are between one and two orders of magnitude lower. The accuracy is improved by the iterative implementation of the multi-scaling strategy, but in exchange, the computation time increases.

Since only a few tapes are analyzed in the multi-scale models, the **J** distributions of the non-analyzed tapes must be approximated somehow. The linear interpolation is a fairly straightforward process. However, this method is unable to lead to the expected **J** distributions throughout the tape's width, as explained in Appendix A. Hence, a new interpolation method, referred to as ICDF, has been proposed. Even though the ICDF interpolation produces meaningful results, the improvements are concentrated around the current fronts of the **J** distributions, and the positive effect in the overall results is marginal. Therefore, this interpolation method is not implemented in the simultaneous multi-scaling strategies, because the computational burden added by the ICDF interpolation is not justified by the outcome.

The computation time of the *H* simultaneous multi-scale model is similar to that of the *H* full model, and both models share the same variables, geometry, and number of DOF. The *H* simultaneous multi-scale model prevents the presence of the non-linear resistivity of the superconductor material in the non-analyzed tapes, as described in Section 4.2. Nevertheless, this simplification of the model is not reflected in the computation time due to the imposition of the interpolated **J** distributions and interpolation process itself. The homogenization of the non-analyzed tapes in the *H* simultaneous

multi-scale homogeneous model reduces the number of DOF to one fifth of the number of the H full model. This reduction allows reducing the computation time roughly by a factor of two. The accuracy of the H simultaneous multi-scale and H simultaneous multi-scale homogeneous models is almost the same, with an R^2 coefficient around 0.98, for both cases.

The T - A full model has more DOF than the H full model, this difference is mostly due to the use of second-order elements to approximate \mathbf{A} in the T - A formulation. Despite the larger number of DOF, the T - A full model is approximately five times faster than the H full model. Both full models consider the same number of elements along the tape's width, hence the reduction in the computation time is just influenced by the choice of the formulation.

Among the T - A models, the one with the lowest accuracy ($R^2 = 0.8854$) value is the T - A reduced model. The separation between densified tapes is larger than the separation between tapes in the original stack, therefore the background magnetic field is locally distorted and the \mathbf{J} distribution deviates from the reference values. The number of densified tapes in the densified model has to be larger than the number of analyzed tapes in the multi-scale models, otherwise the accuracy is drastically affected.

When going from the H full model to the H simultaneous multi-scale model, the number of DOF remains the same, but when going from the T - A full model to the T - A simultaneous multi-scale model the number of DOF is reduced. The reduction in the number of DOF is possible because, in the T - A simultaneous multi-scale model, the vector potential \mathbf{T} is not computed in the non-analyzed tapes, therefore the DOF associated to \mathbf{T} in the non-analyzed tapes are not required. The superiority of the T - A simultaneous multi-scale model over the H simultaneous multi-scale becomes clear when the computation times are compared. The T - A simultaneous multi-scale model is approximately ten times faster than the H simultaneous multi-scale model. At the same time, the T - A simultaneous multi-scale model is two times faster than T - A full model. The accuracy of the T - A simultaneous multi-scale model ($R^2 = 0.9913$) is slightly better than the H simultaneous multi-scale model ($R^2 = 0.9833$).

The T - A simultaneous multi-scale model can be simplified by means of either equivalent tapes or homogenous bulks to model the non-analyzed tapes, i.e., the T - A simultaneous multi-scale reduced and homogenous models. The accuracy of the three T - A simultaneous multi-scale models is similar, with R^2 values between 0.9831 and 0.9913. For the case of the three T - A simultaneous multi-scale models, the number of DOF is reduced when densified tapes and homogenous bulks are used, but the computation time is just reduced in the T - A simultaneous multi-scale densified model. The computation time of the T - A simultaneous multi-scale homogeneous model is incremented to more than three times the computation time of the T - A simultaneous multi-scale model. This is not the case of the H simultaneous multi-scale homogeneous model where the computation time is reduced due to the homogenization of the non-analyzed tapes. The simplification of the H simultaneous multi-scale model by means of the use of densified tapes is not possible because, as explained in Section 5.1, surface current densities cannot be imposed into an H formulation model.

Other than the single-tape submodels of the H multi-scale models, the models with the lowest number of DOF are the H and T - A homogenous models. When compared to their respective full models the homogenization reduces the number of DOF by factors of 30.4 and 26.6, for the H and T - A homogenous models, respectively. Also, the H and T - A homogenous models have two of the

lowest computation times. When compared to their respective full models speed up factors (ratio of the computation times) induced by the homogenization are 28.8 and 13.1, for the H and $T-A$ homogenous models, respectively. Despite this last difference in the speed up factors, the $T-A$ homogenous model (15 min) is approximately 2.5 times faster than the H homogenous model (37 min). Therefore, the $T-A$ homogenous is the most efficient strategy, because it benefits from the speed up factors offered by the $T-A$ formulation and the homogenization. Hence, the $T-A$ homogenous strategy is the fastest one. It should be pointed out that the homogenization causes some slight distortions in the \mathbf{J} distribution. The presence of the distortions is reflected in the reduction of the R^2 coefficients to around 0.92 for both H and $T-A$ homogeneous models.

Chapter 7 32 T All-Superconducting Magnet

High magnetic field facilities are built and operated to enable research in materials science. Nuclear fusion, medicine and pharmacology are among the areas of science that benefit from high magnetic field facilities [16], [108]. The capacity of HTS material to maintain high critical currents under high magnetic fields has strongly stimulated the research towards a new generation of high-field magnets employing commercial HTS tapes [109]–[111]. At the time of writing, the highest reported direct-current magnetic field is 45.5 T. This value was recently reached by a 14.4 T HTS test coil operated inside a 31.1 T resistive magnet [112]. This insert (inner coils), called Little Big Coil (LBC), is part of the efforts undertaken at the National High Magnetic Field Laboratory (NHMFL) in Tallahassee, USA, to pave the way for the use of HTS tapes in high-field magnets. The field generated by the LBC slightly exceeded the 45 T routinely provided to users in the NHMFL by a resistive-superconducting hybrid magnet that has been in operation since 2000 [113].

There are many HTS inserts, test coils and user magnet projects around the world [14], [101], [114]–[120]. The 26 T all-GdBCO magnet was designed by the MIT Francis Bitter Magnet Laboratory, and constructed and tested by SuNAM Co. [115]. A 25 T all-superconducting magnet with an 11.5 T HTS insert was developed at High Field Laboratory for Superconducting Materials (HFLSM) in the Tohoku University [117]. Another 25 T all-superconducting magnet with a 7.5 T HTS insert is under development at the Chinese Academy of Science [114]. The “NOUGAT” project, at the French National High Magnetic Field Laboratory in Grenoble, has the target to generate 30 T with a 10 T HTS insert working inside a 20 T resistive magnet [111], [119]. Within these projects, the all-superconducting magnet with the most intense field is the 32 T all-superconducting (for brevity, all-sc) magnet of the NHMFL [101], [120].

The 32 T all-sc was successfully tested in December 2017 and it is expected to be available soon for users [20]. It consists of a 17 T HTS insert and a 15 T LTS outsert (outer coils). The LTS outsert was custom-made by Oxford Instruments, Inc. The HTS insert is made of more than 20,000 turns of HTS tapes manufactured by SuperPower Inc. [8]. The windings of the insert should withstand extreme Lorentz’s forces, consequently the mechanical strength of the winding is increased by co-winding the tapes with sol-gel plated stainless steel strips. The design and operation of 32 T all-sc magnet requires

vast knowledge in several disciplines. For example, the aspects of the mechanical design are reported in [121], and the analysis of quench has been carried out in [122]–[124].

One of the challenges of this new magnet technology is the estimation of the current density distribution in the HTS insert. The \mathbf{J} distribution allows computing the hysteresis losses and the attenuation in the magnetic field produced by the screening currents, i.e., the so-called Screening Current-Induced Field (SCIF) [14], [125]. The main limitation for the analysis of large-scale HTS systems, like the 32 T all-sc magnet, using H full models is the huge amount of computational resources required to deal with tens of millions of DOF. The analysis of the 32 T all-sc magnet was one of the issues tackled right from the beginning of the present research. As part of this effort, an H iterative multi-scale model of the full-sized HTS insert was presented in [126]. Two attempts have been made by other authors to deal with the electromagnetic modeling of the 32 T all-sc. The study of smaller size prototype magnets was addressed using an H homogeneous model in [102]. And, the model of the inner coil of the HTS insert, also using an H homogenous model, was presented in [28].

After having been successfully validated the T - A homogeneous strategy in Section 5.3, this strategy is subsequently used to address the electromagnetic modeling of the 32 T all-sc magnet. This strategy was chosen because, from all the strategies presented in the previous chapters, it is the one that requires the lower amount of computational recourses while retaining sufficient accuracy. In this case, it is not possible to implement a H full model of the 32 T all-sc magnet, and only the results of the T - A homogeneous model are presented. It should be noticed that the T - A homogenous strategy has already been validated. The T - A homogeneous model enables the analysis of the full-sized HTS insert, considering the effect of the magnetic field generated by the LTS outsert, under the conditions imposed by a real charge cycle.

7.1 Magnet Description and Model

As previously mentioned, the 32 T all-sc magnet is made of a 17 T HTS insert and a 15 T LTS outsert. The HTS insert is comprised of two concentric coils, referred to as Coil 1 and Coil 2. These coils consist of 20 and 36 double pancakes made of HTS tapes co-wound with a stainless-steel tape. The HTS tapes have a width of 4 mm and a thickness of approximately 170 μm , while the HTS layer is 1 μm thick. The LTS outsert is made of three Nb_3Sn coils and two NbTi coils. Figure 7.1 shows the sketch of the 32 T all-sc magnet, this figure was provided by HNMFL [127]. Table 7-1 and Table 7-2 outline the geometric parameters of the HTS insert and the LTS outsert, respectively. For a more detailed description of the magnet, the reader is referred to [101], [120].

When the system is made of cylindrical coils, the system's symmetries allow reducing the model, to only a 1/4th of the full 2D axisymmetric one. In the present case, only the right upper quadrant of magnet is considered. Figure 7.2 shows the axisymmetric sketch of the 32 T all-sc magnet.

The five coils of the LTS outsert are modeled as five concentric bulks in which uniform current densities are imposed to provide a magnetic flux density of 15 T in the center of the magnet at peak-field operation. These uniform current densities are assumed to be independent of the field

produced by the HTS insert. Therefore, the electromagnetic coupling is as follows: the field produced by the LTS outsert affects the HTS insert, but the uniform current density imposed in the LTS outsert is independent of the field produced by the HTS insert. This is a valid assumption because the LTS outsert is made of multi-filamentary wires, therefore the SCIF is relatively small [128].

Table 7-1. HTS insert parameters.

Parameters	Coil 1	Coil 2
Inner radius (mm)	20	82
Outer radius (mm)	70	116
Height (mm)	178	320.4
Pancakes	40	72
Turns/Pancake	253	145

Table 7-2. LTS outsert parameters.

Parameter	Coil 1	Coil 2	Coil 3	Coil 4	Coil 5
Inner radius (mm)	134.93	171.81	213.89	256.77	288.55
Outer radius (mm)	154.92	191.30	234.08	279.56	311.41
Height (mm)	517.40	557.20	597.00	636.80	636.80
Turns	5234	6662	8356	5302	7127

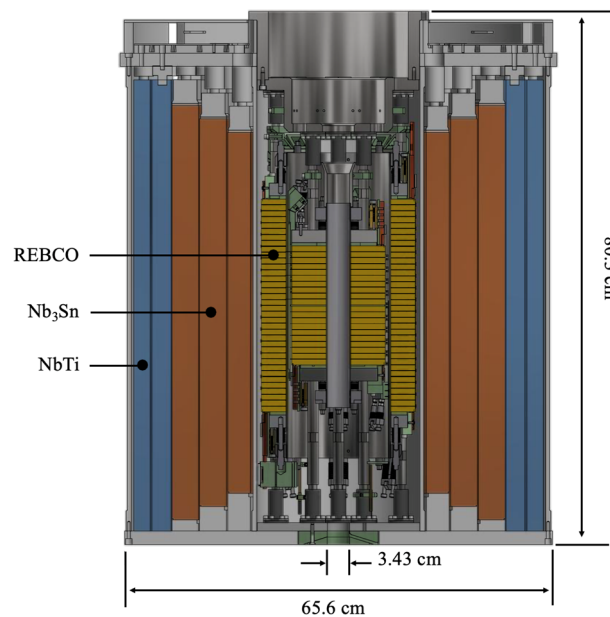


Figure 7.1. Sketch of the 32 T all-superconducting magnet. The HTS insert (inner coils) consist of two coils made of 20 and 36 double HTS pancakes. The LTS outsert (outer coils) consist of three Nb₃Sn coils and two NbTi coils. Figure provided by HNMFL [127], used with permission, Hubertus Weijers.

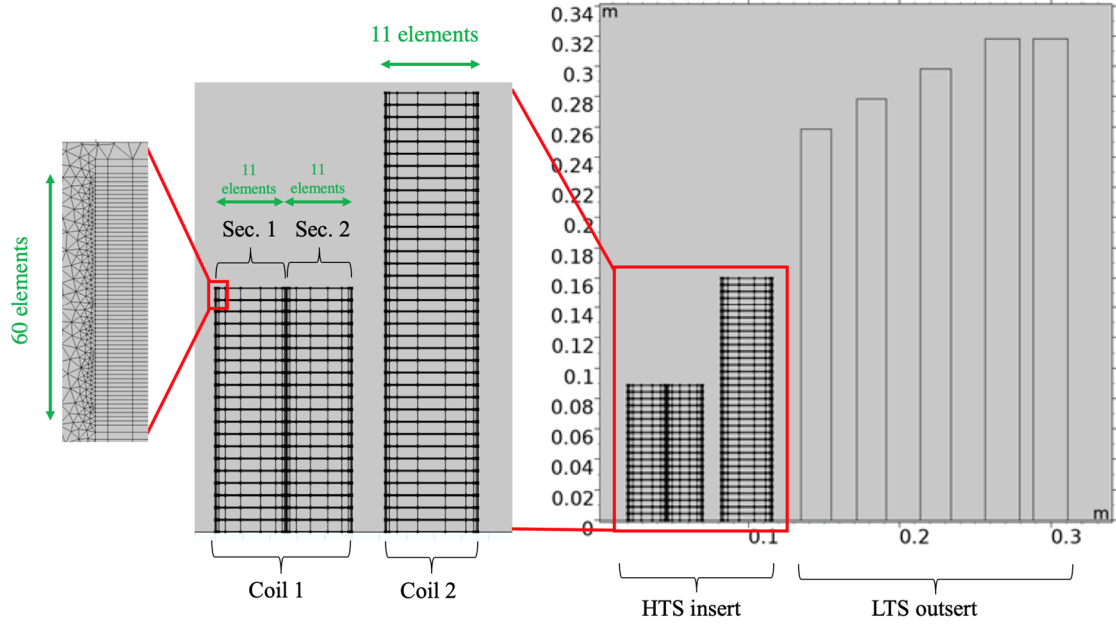


Figure 7.2. Geometry and mesh of the model of the 32 T all-sc magnet. The figure shows the HTS insert and the LTS outsert, and the coils of the insert. The mesh of the bulks considers 60 elements along the tape's width, and 11 elements along the coil/section's thickness.

7.2 Critical Current Density

The characterization of the HTS tape was carried out at NHMFL, by collecting I_c measurements at 4.2 K. The collected data were provided by NHMFL [127].

The resistivity of the superconducting material is modeled by the power-law model (2-4). The J_c was derived from I_c measurements using the parameter-free method proposed in [57]. For easier handling, the data obtained with the free-parameter method were fitted into an expression similar to (2-5). In the framework of an axisymmetric model depicted in Figure 7.2, this expression takes the following form,

$$J_c(B_r, B_z) = \frac{\beta J_{c0}}{\left(1 + \frac{\sqrt{k^2 B_z^2 + B_r^2}}{B_0}\right)^\alpha} \quad (7-1)$$

where B_r and B_z are the radial and axial components of the magnetic flux density. The previous equation includes an extra dimensionless coefficient β . This coefficient is included to handle the variation of I_c among the different batches of tapes. The rest of the parameters of (7-1) and the power-law model are summarized in Table 7-3.

Each pancake of Coil 2 is wound with a single piece of HTS tape having the same I_c value, and therefore they have the same β coefficient. In contrast, each pancake of Coil 1 is wound with two pieces of tape having different I_c values. Therefore, the Coil 1 pancakes are further subdivided into two sections. Section 1, going from tape 1 to tape 131, and Section 2, going from tape 132 to tape 253. The β coefficient takes values ranging from 0.63 for the pancakes in the middle plane to 1.5 for the pancakes in the upper positions. The values of the β coefficient used in the present model are contained in the tables of the Appendix C. These values were provided by NHMFL [127].

Table 7-3. HTS tape parameters.

Parameter	Value
E_c	$1e-4 \text{ Vm}^{-1}$
n	25
J_{c0}	$7.24e11 \text{ Am}^{-2}$
B_0	0.4674 T
k	$9.13e-3$
α	0.7518

7.3 T - A Homogeneous Model

In a 2D axisymmetric geometry the only component of the vector potential \mathbf{A} is A_φ (azimuthal component). In the 1D superconducting layers, the only non-zero component of the current density is defined by $J_\varphi = \partial T_r / \partial z$. Then, the governing equations of the \mathbf{A} and \mathbf{T} formulations, (2-20) and (2-22), respectively, considering cylindrical coordinates are given by,

$$\frac{\partial}{\partial z} \left(\rho_{HTS} \frac{\partial T_r}{\partial z} \right) = \frac{\partial B_r}{\partial t}, \quad (7-2)$$

$$\nabla^2 A_\varphi = -\mu_0 J_\varphi. \quad (7-3)$$

The homogeneous bulks representing the pancakes in the T - A homogeneous model were meshed with a structured mesh considering 60 elements uniformly distributed along the tape's width, as shown in Figure 7.2. This number of elements was used in the previous chapters and was justified in Section 3.2. The results reported in the previous chapters and in [104], [126] show that more significant variations in the losses are expected in the inner and outer tapes of the pancakes. Therefore, the mesh of the Coil 2 pancakes has 11 elements along the bulk's thickness, and the elements' distribution considers an increasing number of elements at the bulk's extremities. This distribution of elements is shown in Figure 7.2. It should be mentioned that the choice of the number of elements

and its distribution was obtained by trying out different numbers of elements and element distributions until the elected distribution fulfilled the compromise between accuracy and computation time fixed by the user.

Because of the further division of the Coil 1 pancakes, each section considers a mesh with 11 elements along each section's thickness. The transition between sections with different coefficient β produces drastic variations in \mathbf{J} and in the losses at the middle of Coil 1. In order to avoid this numerical artifact, it is considered that β experiences a linear change starting at tape 128 and finishing at tape 134. The distribution of the elements in Coil 1 is also shown in Figure 7.2.

7.4 Simulation Results

The simulated charge cycle represents a real operating condition for the magnet. The magnetic flux density at the center of the magnet is charged up to 32 T in 1 h, then is discharged up to -32 T for 2 h, and the process is repeated. The currents in the HTS insert and the LTS outsert have the triangular shape presented in Figure 7.3. The current amplitudes are 173 A and 268 A in the insert and outsert, respectively. The simulated time span is 6 h.

The magnet flux density magnitude $|\mathbf{B}|$ in the insert and the outsert, as well as the normalized current density \mathbf{J}_n in the insert, at the first peak of the charge cycle ($t = 1$ h) are shown in Figure 7.4. In Figure 7.4 (b), it is possible to appreciate the screening currents induced by the penetration of the magnetic field into the tapes. At the peak of the charge cycle, the \mathbf{J} distribution is such that the upper pancakes, especially those of Coil 2, are fully penetrated mainly by the screening currents. Also, it is possible to appreciate changes in \mathbf{J}_n when going from Section 1 to Section 2 in Coil 1. These changes are caused by the variation in the coefficient β .

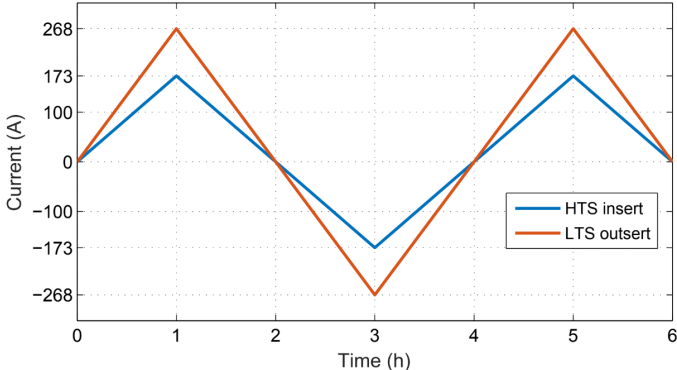


Figure 7.3. Charge cycle used in the simulation. The transport currents in the HTS insert and the LTS outsert has a triangular shape.

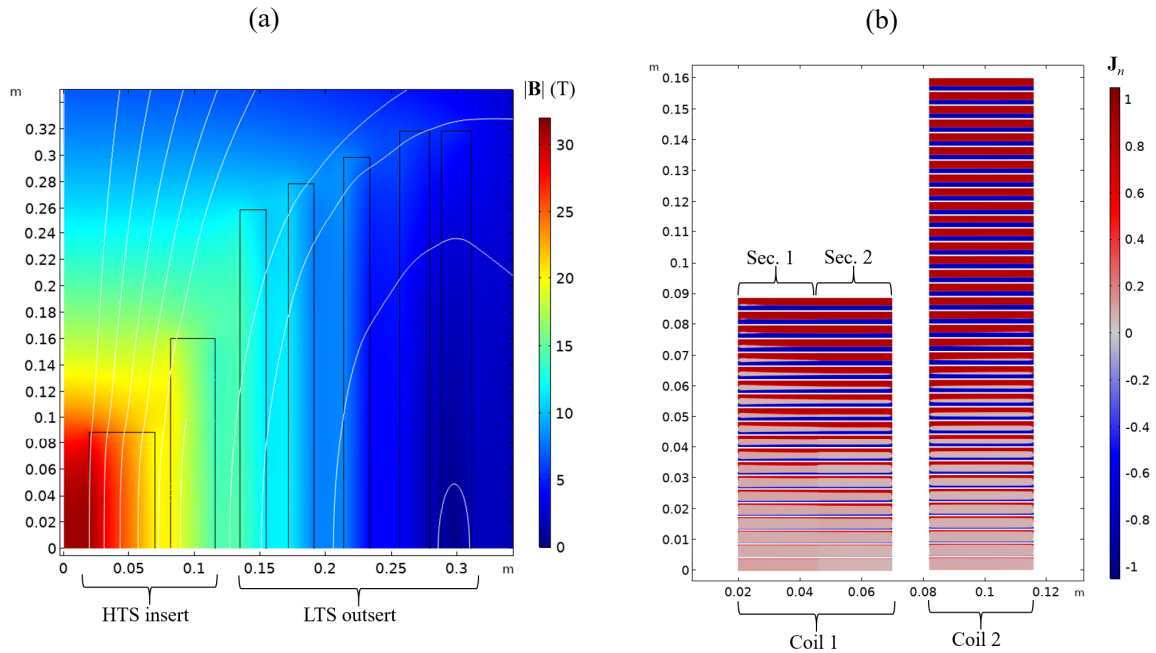


Figure 7.4. (a) Magnetic flux density magnitude and (b) normalized current density at 1 h, the first peak of the ramping cycle. The upper pancakes are fully penetrated by screening currents.

7.4.1 Losses

The power dissipation as a function of time during the simulated lapse is presented with a black line in Figure 7.5. The red line represents the charge cycle. The transient effects cause that the losses of the first ramp from zero current to the first positive peak (in the interval [0, 1 h]) are lower than those of the first ramp from zero current to the first negative peak (in the interval [2 h, 3 h]). After the transient effects, the losses are periodic with a frequency that is twice that of the charge cycle. The total hysteresis losses over the 6 h charge cycle is $Q = 61.08$ kJ.

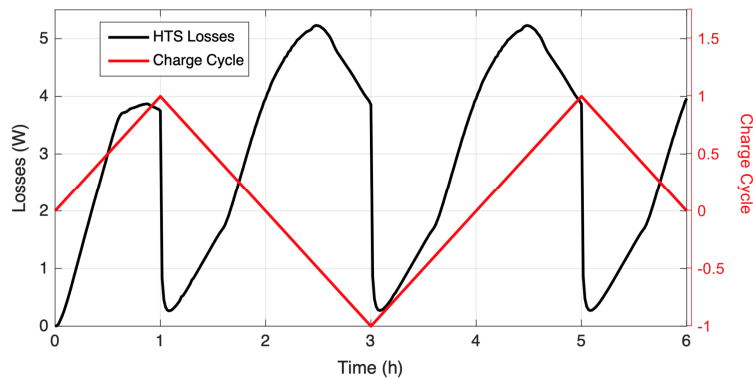


Figure 7.5. The black line represents the instantaneous total hysteresis loss. The red line represents the charge cycle.

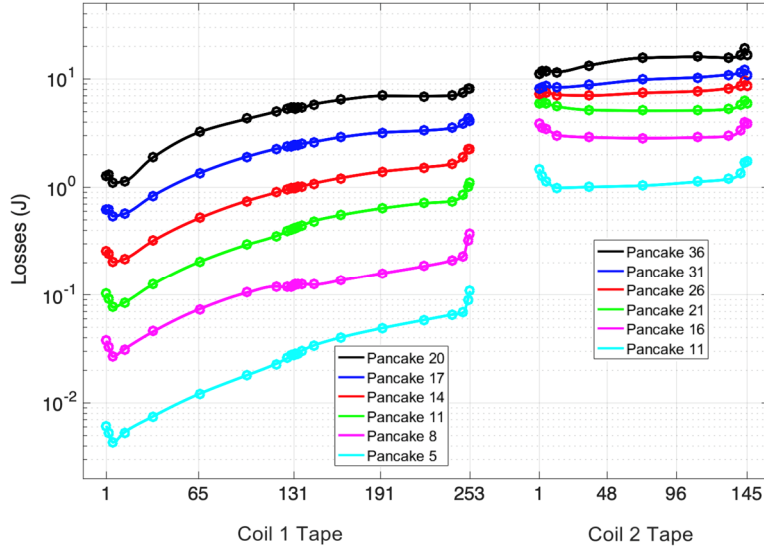


Figure 7.6. Losses in selected pancakes of both coils of the HTS insert.

The losses in some representative pancakes as a function of the tape's number are shown in Figure 7.6. The pancakes at the upper positions have higher losses, as it has been previously observed in [102], [104], [126]. This behavior results from the deeper penetration of the magnetic field in the upper pancakes. As expected from Figure 7.4 (b), the losses are greater in Coil 2 than in Coil 1, with 82.9 % of the total loss taking place in the former. The distribution of the elements along the pancakes allows to successfully obtain the variations in the losses at the inner and outer tapes of the pancakes. There are more data points at the central part of Coil 1, because the mesh considers a denser distribution of elements in that position, then it is possible to observe the effects of the transition between sections with different β .

7.4.2 Screening Current-Induced Field

The screening currents are induced by the penetration of the magnetic field into the tapes. The magnetic field penetrates from the borders of the tapes producing current fronts. The screening current affects the magnetic field distribution all over the coil and particularly attenuates the central magnetic field. This attenuation is referred to as SCIF, and it is quantified by the following expression,

$$B_{SCIF} = B_{sim} - B_n, \quad (7-4)$$

where B_{sim} is the field computed at the center of the magnet including the effect of the screening currents. The nominal field B_n is the field considering uniform current distributions flowing in both the insert and the outsert.

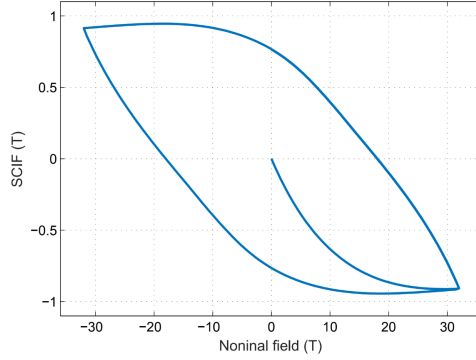


Figure 7.7. SCIF. B_{SCIF} versus nominal field B_n . The lapse of the charge cycle allows to retrieve the hysteresis loop. The maximum B_{sim} is 31.09 T.

When B_{SCIF} is plotted as a function of B_n , a hysteresis loop is formed. The simulated lapse of the charge cycle in Figure 7.3 is enough to retrieve the full hysteresis loop shown in Figure 7.7. The B_{sim} at the peak of the charge cycle is 31.09 T, which is almost 1 T lower than the expected 32 T. The remnant field at 0 A is 0.77 T.

The comparison of the estimated losses against experimental data is hindered by the difficulty of distinguishing the hysteresis losses contribution from the total losses. For a fair comparison of the SCIF, the numerical model should couple the mechanic and electromagnetic phenomena. The mechanical stress degrades J_c [129], [130], and the J_c strongly affects the shape of the SCIF loop [25]. Therefore, the validation against experimental results requires either a specific experimental set up or a more complex model, which are both beyond the scope of this thesis.

7.5 Real-Time Simulations

The computer used to perform the simulations described in this chapter is a desktop computer (6 cores, Intel (R) Xeon(R) ES-2630, 2.2 GHz, 64 GB RAM). The time required to simulate the 6 h charge cycle with the T - A homogenous model is 5 h 29 min. It is demonstrated that the T - A homogenous strategy not only facilitates the modeling of large-scale HTS systems, but also allows achieving real-time simulations of real charge/discharge cycles magnets on a personal computer.

The desktop computer used in this chapter is the same computer used to perform the simulation using the H iterative multi-scale model of the 32 T all-sc magnet reported in [126]. In that publication [126], the simulation do not consider the effect of the LTS outsert, and the charge cycle is a 2 min long triangle-shaped ramp, which do not represent a real-case scenario. The total hysteresis losses estimated using the H iterative multi-scale model are 9.946 kJ, while the losses estimated using the T - A homogeneous model are 9.659 kJ, this means that the difference is about 2.9 %. For these conditions, the computation time required to perform the simulation with the H iterative multi-scale

model is 19 days and 6 h, while the computation time required with the T - A homogeneous model is 1 h and 10 min. Therefore, the T - A homogeneous model is 396.2 times faster than the H iterative multi-scale model.

Chapter 8 Conclusions

As mentioned in Section 2.4, the H formulation has arguably become the de facto standard to compute the electromagnetic quantities within the applied superconductivity community. However, the T - A formulation has proven to be more efficient to model large-scale systems made of HTS tapes than the H formulation. For the case study, the speed up factor in favor of the T - A formulation, reported in Chapter 6, is five. Also, the other strategies based on the T - A formulation have lower computation times than their H formulation counterparts.

The multi-scaling and homogenization strategies have been successfully used together with the H formulation by various authors. In this context, the contributions of the present research can be classified into the following four categories. First, the H multi-scale strategy was improved, giving rise to the H iterative and simultaneous multi-scale strategies. Second, the properties of the T - A formulation were exploited to develop the T - A densified strategy. Third, the multi-scaling strategy was adapted to be used in conjunction with the T - A formulation. Finally, the most efficient strategy emerged from the adaptation of the homogeneous strategy to be used with the T - A formulation.

It was demonstrated that all the new strategies, except for the H simultaneous multi-scaling, significantly reduce the computation time. In general, all the proposed strategies simplify the description of the systems and provide quick results without seriously compromising the accuracy. All the strategies, except for the H multi-scaling, allow estimating the \mathbf{J} distributions and, subsequently the magnetic field and the losses with a high degree of accuracy. Excluding the H simultaneous multi-scale model, the lower accuracy is the accuracy of the T - A densified model ($R^2 = 0.8854$, $er_Q = -2.62\%$). Henceforth, the models proposed in this work represent a good alternative to the full models, and alternative that is more significant in the cases where the size of the system does not allow the implementation and use of the full models.

The iterative multi-scaling strategy surpasses the main limitation of the multi-scaling strategy, i.e., the lack of a definition for the “initial” \mathbf{J} distribution. The iterative multi-scaling strategy starts from a uniform \mathbf{J} distribution and leads to a better \mathbf{J} distribution with each iteration. This is a clear advantage

over the classic multi-scaling strategy, inasmuch as it leads to a more accurate estimation of the background magnetic field over the entire system.

The simultaneous multi-scaling strategies can be seen as enhanced versions of the iterative multi-scaling strategy, since they require just one single model and do not rely on the iterative implementation of several dynamic simulations of two coupled submodels. Nevertheless, the H simultaneous multi-scaling strategy does not reduce the computation time, as it is the case for the other simultaneous multi-scaling strategies. All the multi-scaling strategies share the disadvantage that there is no automatic method to define the best choice of the set of analyzed tapes, and it becomes necessary to resort to the user's self-experience.

The speed up factor offered by the T - A formulation can be further increased by the additional use of the densification, multi-scaling and homogenization strategies. Within the T - A strategies, the T - A densified is the one with the lowest accuracy. The accuracy of the T - A simultaneous multi-scaling model is almost the same of that of the T - A full model, while the computation time is halved. It is important to emphasize that the T - A homogenous model has the lowest computation time. The T - A strategies presented in Chapter 5 inherit the limitations of the T - A formulation as presented in Section 2.5.2, i.e., they are intrinsically limited to cases where the 1D approximation of the superconducting layer is meaningful. Accordingly, the T - A strategies, here presented, are restricted to the analysis of systems made of 2G HTS tapes. On the contrary, the H full and H multi-scaling strategies are also suitable for the analysis of systems made of wires with different geometries, like MgB₂ wires, for instance.

The H iterative multi-scaling strategy has some additional advantages. It may be the case of a sufficiently large system where the memory resources of a personal computer are surpassed, even for the homogenous models. The H iterative multi-scale models can be used to analyze large-scale systems almost without size limit. The reason is that the number of DOF of the single-tape model remains constant independently of the size of the system. Instead the coil submodel, being a magnetostatic model, requires a lesser amount of computational resources to be simulated, therefore it is possible to analyze considerably larger systems. Also, the H iterative multi-scale models can be constructed with the objective of achieving an almost arbitrary level of local accuracy. To this end, it is necessary to increment the number of analyzed tapes in the specific regions where the accuracy needs to be increased. Finally, the simulations involving the single-tape submodels have the advantage to be easily parallelized, further reducing the computation time.

Once it was demonstrated that the T - A homogeneous strategy leads to quicker results, and its accuracy is satisfying, the T - A homogeneous strategy was used to build an electromagnetic model of the HTS insert of the 32 T all-sc magnet. This model allows estimating the \mathbf{J} distribution in the HTS tapes of the pancakes, therefore enabling to assess the hysteresis losses as well as the SCIF. The hysteresis losses provide important information to optimize the cooling system. Some applications, like the NMR and MRI magnets, require a high-accuracy of the magnetic field in the center of the magnet. Therefore, phenomena like the SCIF need to be understood and addressed. Although not discussed in the present work, the \mathbf{J} and \mathbf{B} distributions enable to conduct the analysis of the local stress/strain behavior, as it is presented in [131] for the case of the 32 T all-sc magnet. In general, the knowledge of the electromagnetic quantities allows establishing safe operational margins for the magnets as well as improving their design.

When comparing the T - A homogeneous of the 32 T all-sc magnet with other published models, i.e., H homogeneous and H multi-scale, it becomes clear that the T - A homogeneous model significantly reduces the computational load. Then, the T - A homogeneous model makes it possible to model the full-size HTS insert including the effect of the background magnetic field produced by the LTS outsert.

The availability of T - A homogeneous models opens up the possibility to perform real-time simulations, considering charge cycles which represent the real operation conditions of the systems, using personal computers. To the best of our knowledge, this capability is new in the analysis of such complex systems, like the 32 T all-sc magnet, and also brings the opportunity to perform faster parametric analysis.

The models described in the present document were built in the commercial software COMSOL Multiphysics, which also helps in the dissemination of the proposed strategies. Two simple model files solving the so-called “Benchmark #3” using the T - A multi-scale and T - A homogenous strategies, are publicly available in www.htsmodelling.com [132]. The Benchmark #3 is a small case study made of a stack of 20 HTS tapes proposed by the *HTS modeling workgroup* [132]. This website is a collective effort to share codes and documentation to speed up the research and development process in the modeling of HTS systems [55].

Appendix A

During the implementation of the T - A full model, it was found that *spurious oscillations* may appear in the current density in the superconducting layers. Similar issues have already been reported in fluid mechanics literature [133] [134], where different order elements are used to approximate velocity and pressure. It is hereinafter demonstrated that, with a proper choice of order elements, the spurious oscillations can be prevented. This issue has not been discussed in the literature about the T - A formulation yet, even when the problem of the spurious oscillations is visible in the results reported in [34]. The choice of the order of the elements is just addressed in [34] as a means to reduce the computation time.

The correct choice of the order of the elements to prevent the spurious oscillations is found by trial and error. Interestingly, the spurious oscillations can be hidden using the smoothing and resolution refinement options offered by the post-processing tools of COMSOL. The post-processing options are sometimes activated by default; therefore, it is possible for the spurious oscillations to go unnoticed. In the present work, such tools were not used and raw data are provided.

As discussed in the Chapter 2, the T - A formulation uses two state variables, \mathbf{T} and \mathbf{A} . Each variable can be approximated using elements of different orders. To assess the correct choice of orders, the case study, under the conditions of an 11 A and 50 Hz sinusoidal transport current, was simulated using the T - A full model considering three combinations of element orders. The first simulation uses Lagrange first-order elements for both \mathbf{T} and \mathbf{A} , the second simulation uses Lagrange second-order elements for both variables, while the last simulation uses first-order elements for \mathbf{T} and second-order elements for \mathbf{A} . The combination second-order elements for \mathbf{T} and first-order elements for \mathbf{A} was also tested, but in this case the simulation did not converge to any solution.

The \mathbf{J} distributions at $t = 15$ ms computed with the reference and T - A full models are shown in Figure A.1. The J_n for all the tapes is presented in the first row, while \mathbf{J} in the tape 96 of pancake 3 is presented in the second row. The results show that the \mathbf{J} computed with the T - A full model presents spurious oscillations when the same order of elements is used to approximate both \mathbf{T} and \mathbf{A} . The period of the oscillations when first-order elements are used for both variables is twice the period when second-order elements are used. Also, the period of the oscillations is reduced when the number of

elements along the tape's width is increased. The oscillations disappear when first-order elements are used for **T** and second-order elements for **A**

The relative error of the average losses er_Q , the coefficient of determination R^2 , and the normalized computation time $\bar{c}t$ are summarized in Table A-1. The spurious oscillations are present at subcritical values, so they have a negligible impact on the hysteresis losses. The relative error has an absolute value lower 1 % error for the three cases, while lower relative error (0.64 %) is achieved with the model using first-order elements for **T** and second-order elements for **A**.

The impact of the oscillations is clearly reflected in the R^2 coefficients. The smaller R^2 value of the model using second-order elements for both variables compared to the model using first-order elements reflects larger amplitudes in the oscillations as shown in Figure A.1. The model with the largest R^2 coefficient is the model using first-order elements for **T** and second-order elements for **A**, the one without spurious oscillations, confirming that this is the correct choice for the element's order.

The increment in the order of the elements leads to the increment of the number of DOF and the computation time. Then, the computation time when second-order elements are used for both variables is the largest computation time ($\bar{c}t = 28.59\%$), while the lowest computation time is achieved when first-order elements are used for both variables ($\bar{c}t = 8.77\%$).

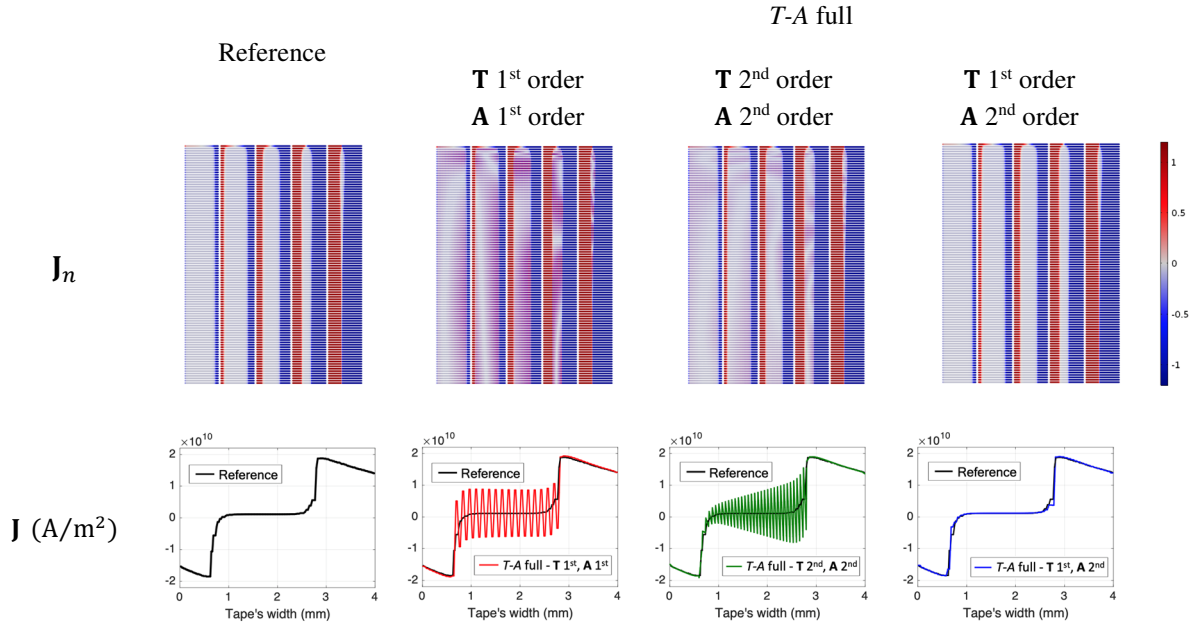


Figure A.1. \mathbf{J} distribution at $t = 15\text{ ms}$ (the second peak of the transport current) for the reference and T - A full models. The first rows show \mathbf{J}_n for all the tapes. The second row shows \mathbf{J} in the tape 96 of pancake 3. The T - A full model uses different order elements for **T** and **A**. The spurious oscillations are prevented when first order elements are used for **T** and second order elements for **A**.

Table A-1. Reference and *T-A* full models' comparison.

Model	Losses (W/m)	Computation time (h)		
Reference	127.24	31 h 32 min		
Model	er_Q (%)	R^2	$\bar{c}t$ (%)	
T 1st, A 1st orders	-0.96	0.8905	8.77	
<i>T-A</i> full T 2nd, A 2nd orders	-0.67	0.9884	28.59	
T 1st, A 2nd orders*	0.64	0.9922	10.25	

* **T 1st, A 2nd** order is the combination without spurious oscillations.

Appendix B

In this appendix a new method to interpolate **J** distributions is presented. This method produces meaningful results from the point of view of the physics of the superconductors. The shape of the **J** distributions estimated this way preserves the current fronts present in the original distributions, current fronts that are lost when the usual linear interpolation is applied. The new interpolation method is based on the Inverse Cumulative Density Function (ICDF) interpolation. The ICDF technique was initially proposed to interpolate probability density functions as described in [35].

Consider two normal distributions f_1 and f_3 , these distributions are shown in the first column of Figure B.1. The distributions represent two human populations with short and tall people, respectively. If the distribution f_2 represents a population with intermediate characteristics. How would f_2 be?

The linear interpolation is defined by

$$f_{2_Linear}(x) = \alpha f_1(x) + (1 - \alpha) f_3(x), \quad (\text{B-1})$$

where $\alpha \in [0,1]$ is a parameter indicating the weight given to the distribution f_1 . Clearly f_{2_Linear} does not represent a population of medium-height people. The linearly interpolated distribution is also shown in the first column of Figure B.1. The linear interpolation as defined in (B-1) is the interpolation used in most of the multi-scale models described in this work.

The ICDF method is not based on the interpolation of the original distributions, it is based on the interpolation of the inverse functions of the cumulative distributions. In the ICDF interpolation method, the interpolated distribution f_{2_ICDF} is defined by means of its inverse cumulative density function, given by,

$$\widehat{f_{2_ICDF}}^{-1}(y) = \alpha \widehat{f_1}^{-1}(y) + (1 - \alpha) \widehat{f_3}^{-1}(y), \quad (\text{B-2})$$

where $\widehat{f_1}^{-1}$ is the inverse function of $\widehat{f_1}$, and $\widehat{f_1}$ is the cumulative distribution function of f_1 . The function $\widehat{f_1}$ is given by,

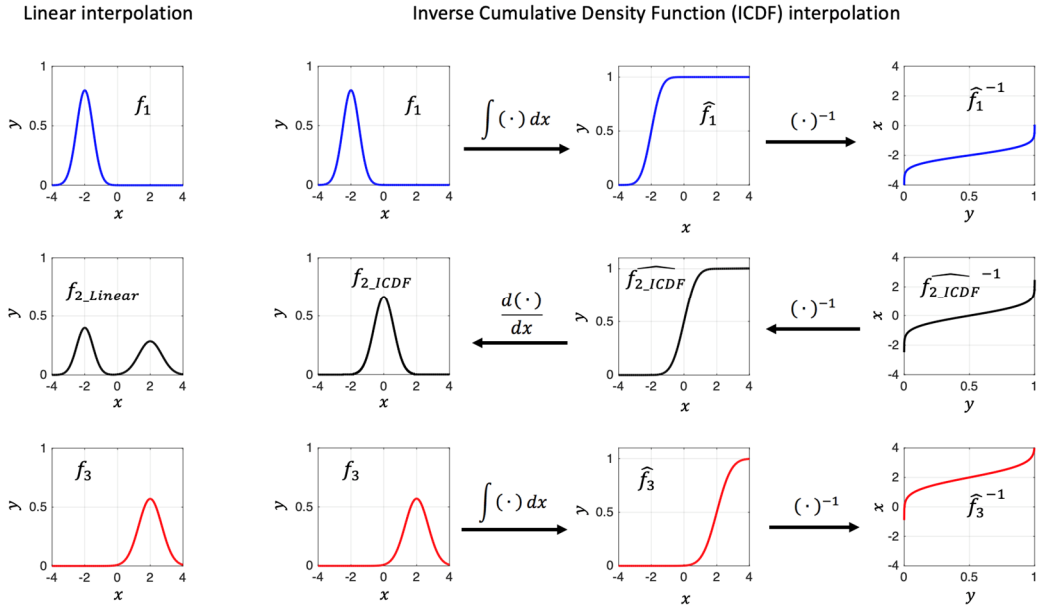


Figure B.1 Linear (left side) and ICDF (right side) interpolation of two normal distributions f_1 and f_3 . The linear produces a bimodal distribution which does not represents expected behavior. The ICDF interpolation offers meaningful results by producing the displacement distributions. The ICDF method actually interpolates the inverse cumulative density functions instead of the distributions themselves.

$$\hat{f}_1(x) = \int_{-\infty}^x f_1(x') dx', \quad (\text{B-3})$$

The rest of the cumulative functions are defined in a similar way. The ICDF interpolation method produces a meaningful result, and indeed the distribution f_{2_ICDF} represents a medium-height population. The distribution f_{2_ICDF} and the pipeline showing the process of the ICDF interpolation method are presented in the right side of Figure B.1.

The ICDF method must be adapted before it can be used to interpolate **J** distributions. First, the application of equation (B-2) is only possible when the cumulative functions are monotonically increasing functions, which in turns requires the original functions to be positive. The strategy proposed here is based on the idea proposed in [107], where prior to the interpolation process, the functions are decomposed into simpler functions. The decomposition proposed here separates the **J** distributions into three components. The first component is a uniform distribution given by the average value (constant component). Once the average component is subtracted from the **J** distribution, the resulting difference is further separated into its positive and negative components. Accordingly, a given **J** distribution \mathbf{J}_1 , being the **J** distribution of a given tape at a given instant, can be expressed as follows,

$$\mathbf{J}_1 = J_{1_avg} + J_{1_pos} + J_{1_neg}, \quad (\text{B-4})$$

where J_{1_avg} , J_{1_pos} , and J_{1_neg} are the average, positive and negative components, respectively. The last two components are called positive and negative, even when they are not necessary the positive and negative parts of \mathbf{J}_1 , they are the positive and negative parts of $\mathbf{J}_1 - J_{1_avg}$, respectively.

The respective components are interpolated separately. In the case of the negative components the interpolation process is applied to the absolute value of these components. The constant components account for the transport current through the tapes. In the cases studied in the present work, the interpolation of the constant component is not necessary because the transport current is the same for all the turns connected in series in the coils.

The next step is to normalize the positive and negative components. The normalizing factor is the defined integral of the component, thus the normalized positive component is defined as

$$\overline{J_{1_pos}} = \frac{J_{1_pos}}{\langle J_{1_pos} \rangle}, \quad (\text{B-5})$$

where J_{1_pos} is the positive component of the distribution \mathbf{J}_1 and the normalizing factor is defined as

$$\langle J_{1_pos} \rangle = \int_q J_{1_pos}(x) dx, \quad (\text{B-6})$$

and q is the tape's width. Thus, the normalized components have a definite integral (given by the area under the graph) equal to 1.

The direct application of equation (B-2) to interpolate the normalized current density components produces the expected results when the positive and negative components have just one local maximum. For some functions, like functions with two or more local maxima, the direct application of equation (B-2) may produce additional spurious local maxima in between the local maxima of the original functions. A similar problem with these spurious local maxima, so-called "translating bumps", was addressed in [107]. The origin of these "translating bumps" is a computational issue, they do not represent any physical phenomena, thus its presence should be avoided. The proposed solution in [107] is to use a multi-resolution scheme, which interpolates different band passed components of the original functions separately. For the specific case of \mathbf{J} distributions, here a simpler solution is proposed, to add an offset ς before the application of equation (B-2). The definite integral of the normalized components plus the offset is equal to a constant $\beta > 1$, as follows,

$$\beta = \int_q (\overline{J_{1_pos}}(x) + \varsigma) dx. \quad (\text{B-7})$$

The offset ς is chosen so that $\beta = 1.5$. Equation (B-7) is also valid for the other normalized positive and negative components. The value $\beta = 1.5$ was heuristically chosen. Smaller values for the offset ς do not eliminate the translating bumps, while larger values mask the original shape of the functions.

The offset ζ causes the cumulative function to be strictly increasing, avoiding step changes in the inverse cumulative function, which in turns avoids the translating bumps.

Now, the interpolated normalized components are obtained similarly to (B-2),

$$\widetilde{J_{2_pos}}^{-1}(y) = \alpha \widetilde{J_{1_pos}}^{-1}(y) + (1 - \alpha) \widetilde{J_{3_pos}}^{-1}(y), \quad (\text{B-8})$$

where,

$$\widetilde{J_{1_pos}}(x) = \int_0^x (\overline{J_{1_pos}}(x') + \zeta) dx'. \quad (\text{B-9})$$

The rest of the cumulative functions are defined in a similar way. In order to retrieve the interpolated component, the offset needs to be subtracted, and the interpolated normalized component must be denormalized. Thus, the interpolated positive component is defined as,

$$J_{2_pos} = \{\alpha \langle J_{1_pos} \rangle + (1 - \alpha) \langle J_{3_pos} \rangle\} \overline{J_{2_pos}}. \quad (\text{B-10})$$

Finally, the interpolated **J** distribution \mathbf{J}_2 is found by adding the average, positive, and negative interpolated components.

Figure B.2 shows an example of the ICDF interpolation, as described above. The distributions \mathbf{J}_1 and \mathbf{J}_3 shown in the first column were obtained from an H full model. The second column shows the decomposition of the distributions into its positive, average and negative components. The third column shows the normalization, integration and inversion of the respective positive components. Between the third and fourth columns the $\widetilde{J_{1_pos}}^{-1}$ and $\widetilde{J_{3_pos}}^{-1}$ are interpolated to find $\widetilde{J_{2_pos}}^{-1}$. The fourth column shows the reverse process of the third column, this is the inversion and differentiation of the interpolated component. The fifth column shows the positive, average and negative interpolated components, the process to interpolate the negative component is similar to that of the positive component. At the end of Figure B.2, it is possible to observe that the linear interpolation produces the averaging of the original **J** distributions. While the ICDF interpolation produces the displacement of the current density fronts, therefore producing meaningful **J** distributions.

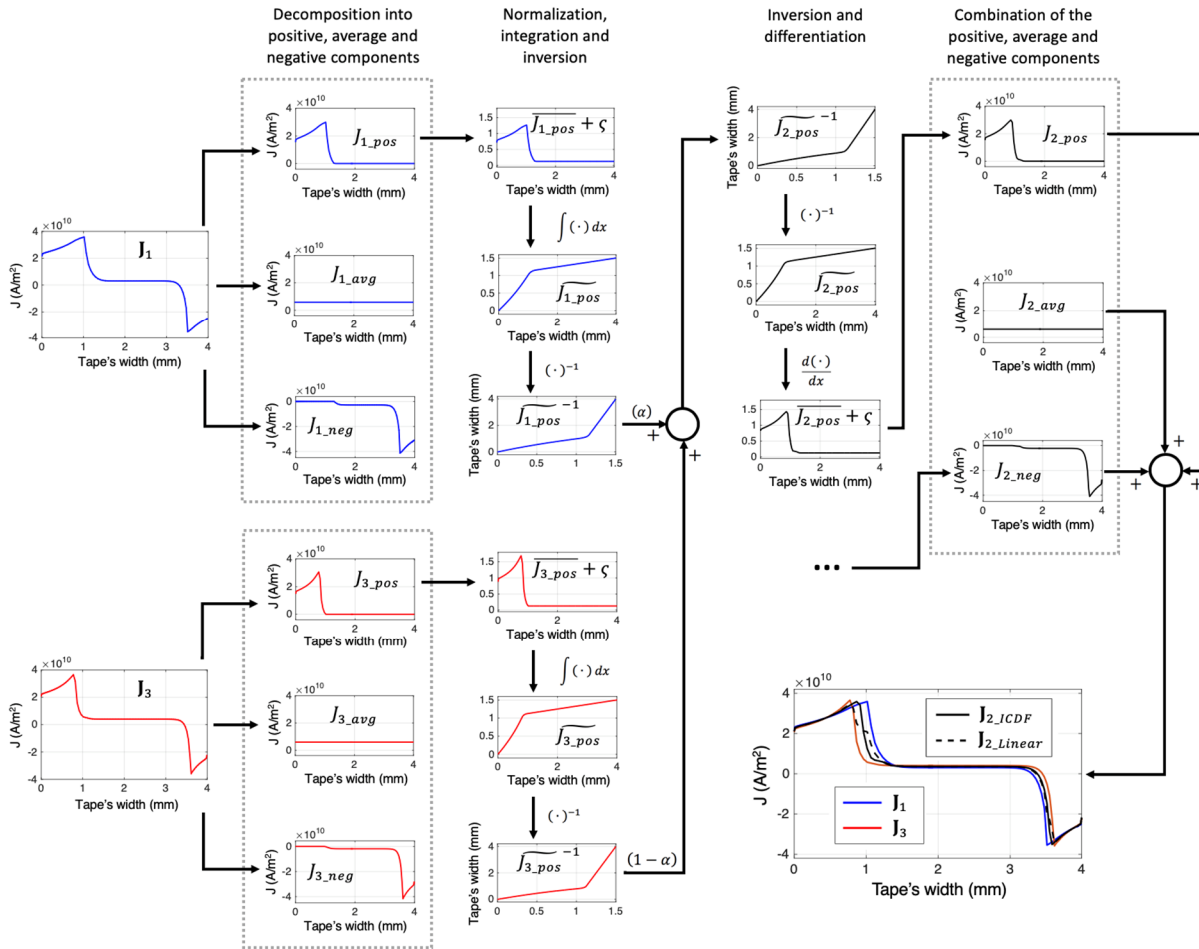


Figure B.2. ICDF interpolation of two J distributions. J_1 and J_3 are used to approximate J_2 . The complete process is just presented for the positive component. The interpolation of the absolute value of the negative component is the same process followed by the positive component. The ICDF interpolation produces the displacement of the current density fronts instead of just the averaging of the J distributions.

Appendix C

The tables included in this appendix contain the values of the β coefficient used in Section 7.2 to handle the variation of I_c among the different batches of tapes. Table C-1 contains the β coefficients used in both sections, inner and outer, of each pancake of Coil 1. Table C-2 contains the β coefficients used in each pancake of Coil 2. The numbering of the pancakes is as follows: pancake 1 is the pancake closest to the mid plane, and pancake 20 and 36 are the upper pancakes of Coil 1 and Coil 2, respectively; see Figure 7.2.

Table C-1. Values of the β coefficient in Coil 1

Pancake	Inner section β coefficient	Outer section β coefficient	Pancake	Inner section β coefficient	Outer section β coefficient
20	1.5063	1.4137	10	0.6601	0.8121
19	1.1765	1.4137	9	0.6308	0.8121
18	1.1185	1.0962	8	0.6381	0.95192
17	1.0851	1.0962	7	0.7526	0.95192
16	1.0444	0.9782	6	0.6479	0.5941
15	0.9977	0.9782	5	0.6966	0.5941
14	0.9565	0.9310	4	0.8306	0.7149
13	0.9426	0.9310	3	0.7966	0.7149
12	0.6649	0.7136	2	0.7833	0.9158
11	0.7526	0.7136	1	0.6162	0.9158

Table C-2. Values of the β coefficient in Coil 1

Pancake	β coefficient	Pancake	β coefficient
36	1.3811	18	0.9867
35	1.3202	17	0.9718
34	1.3086	16	0.9694
33	1.2568	15	0.9546
32	1.1643	14	0.9397
31	1.1472	13	0.9246
30	1.1436	12	0.9032
29	1.1424	11	0.8866
28	1.1241	10	0.8744
27	1.1152	9	0.8720
26	1.1097	8	0.8644
25	1.0666	7	0.8501
24	1.0522	6	0.8281
23	1.0303	5	0.7738
22	1.0279	4	0.7453
21	1.0154	3	0.7110
20	1.0133	2	0.6718
19	0.9975	1	0.6284

In the real magnet the measured values β are not exactly symmetric with respect to the mid plane but, as far as the model of the 32 T all-sc magnet is symmetric, the β coefficients are considered to be symmetric. And the values in Table C-1 and Table C-2 are representative of the real characteristics of the magnet.

Appendix D

This appendix contains a list of references of the articles published during the course of the PhD study. The articles are listed in chronological order.

The first article in the list [D1] deals with the experimental characterization of HTS conductors, the results presented in this article are important in power cable applications. The characterization of HTS conductors is out of the scope of this PhD thesis, but the experience gained was a valuable asset during the rest of the PhD project. The H iterative multi-scale strategy, described in Section 4.1, is published in [D3]. The article [D2] presents the application of the iterative multi-scale strategy to estimate the hysteresis losses in the HTS insert of the 32 T all-sc magnet of the NHMFL. The T - A homogeneous strategy, described in Section 5.3, is published in [D4]. The electromagnetic modeling of the 32 T all-sc magnet by means of the T - A homogeneous strategy, presented in Chapter 7, is published in [D5]. In the context of the collaboration with the NHMFL, the electromagnetic quantities estimated with the T - A homogeneous strategy allowed to address the stress/strain analysis of the 32 T all-sc magnet, these results are published in [D6]. The article [D7] presents the application of the T - A homogeneous strategy to investigate the behavior of the screening current-induced field and the field drift produced by the screening currents in large-scale HTS systems.

The main contribution of this thesis is the development of efficient strategies to address the electromagnetic modeling of large-scale HTS systems. It is important to emphasize that not all of the strategies proposed in the thesis have been published. Another article presenting a comparison of all of the strategies presented in the thesis will be submitted for publication in the following months.

- [D1] M. Breschi, E. Berrospe-Juarez, P. Dolgosheev, A. González-Parada, P. L. Ribani, and F. Trillaud, "Impact of twisting on critical current and n -value of BSCCO and (Re)BCO Tapes for DC Power Cables," *IEEE Trans. Appl. Supercond.*, vol. 27, no. 4, pp. 1–4, 2017.
- [D2] E. Berrospe-Juarez, V. M. R. Zermeño, F. Trillaud, and F. Grilli, "Iterative multi-scale method for estimation of hysteresis losses and current density in large-scale HTS systems," *Supercond. Sci. Technol.*, vol. 31, no. 9, p. 095002, 2018.

- [D3] E. Berrospe-Juarez, V. M. R. Zermeño, F. Trillaud, A.V. Gavrilin, F. Grilli, D. V. Abraimov, D. K. Hilton, H. W. Weijers, “Estimation of Losses in the (RE)BCO Two-Coil Insert of the NHMFL 32 T All-Superconducting Magnet,” *IEEE Trans. Appl. Supercond.*, vol. 28, no. 3, pp. 1–5, 2018.
- [D4] E. Berrospe-Juarez, V. M. R. Zermeño, F. Trillaud, and F. Grilli, “Real-time simulation of large-scale HTS systems: multi-scale and homogeneous models using the T–A formulation,” *Supercond. Sci. Technol.*, vol. 32, no. 6, p. 065003, 2019.
- [D5] E. Berrospe-Juarez, F. Trillaud, V. M. R. Zermeño, F. Grilli, H. W. Weijers, and M. D. Bird, “Screening Currents and Hysteresis Losses in the REBCO Insert of the 32 T All-Superconducting Magnet Using T-A Homogenous Model,” *IEEE Trans. Appl. Supercond.*, vol. 30, no. 4, pp. 1–5, 2020.
- [D6] D. J. Kolb-Bond; E. Berrospe-Juarez; I. Dixon, F. Grilli, V. M. R. Zermeño, F. Trillaud, H. W. Weijers, M. Bird, “Computing Strains due to Screening Currents in REBCO Magnets,” *IEEE Trans. Appl. Supercond.*, 2020.
- [D7] E. Berrospe-Juarez, V. M. R. Zermeño, F. Trillaud, and F. Grilli, “Screening Current- Induced Field and Field Drift Study in HTS coils using T-A homogenous model,” *Journal of Physics: Conference Series* (accepted for publication).

Bibliography

- [1] L. A. Pérez, “Los primeros cien años de la superconductividad,” *Mater. Av.*, vol. 18, pp. 43–48, 2012.
- [2] A. W. B. Taylor, *Superconductivity*, 1st ed. London: Wykeham Publications (London) Ltd, 1970.
- [3] M. N. Wilson, *Suprconducting Magnets*, 1st ed. Clarendon Press Oxford, 1983.
- [4] L. García-Colin Scherer and J. L. del Rio Correa, *Cien años de superconductividad*, Primera. Colegio Nacionla y Universidad Autónoma Metropolitana-Iztapalapa, 2013.
- [5] D. Dew-Hughes, “The critical current of superconductors: An historical review,” *Low Temp. Phys.*, vol. 27, no. 9, pp. 713–722, 2001.
- [6] J. G. Bednorz and K. A. Müller, “Possible high T_c superconductivity in the Ba-La-Cu-O system,” *Zeitschrift für Phys. B Condens. Matter*, vol. 64, no. 2, pp. 189–193, 1986.
- [7] M. K. Wu *et al.*, “Superconductivity at 93 K in a new mixed-phase Yb-Ba-Cu-O compound system at ambient pressure,” *Phys. Rev. Lett.*, vol. 58, no. 9, pp. 908–910, 1987.
- [8] SuperPower Inc., “SuperPower,” 2020. [Online]. Available: <http://www.superpower-inc.com/>. [Accessed: 10-Jan-2020].
- [9] SuNam Co., Ltd, “SuNam,” 2020. [Online]. Available: <http://i-sunam.com/>. [Accessed: 10-Jan-2020].
- [10] Fujikura, “Fujikura,” 2020. [Online]. Available: <https://www.fujikura.com/solutions/superconductingwire/>. [Accessed: 10-Jan-2020].
- [11] B. G. Marchionini, Y. Yamada, L. Martini, and H. Ohsaki, “High-Temperature Superconductivity: A Roadmap for Electric Power Sector Applications, 2015-2030,” *IEEE Trans. Appl. Supercond.*, vol. 27, no. 4, pp. 1–7, 2017.
- [12] Z. Melhem, *High temperature superconductors (HTS) for energy applications*, 1st ed.

Woodhead Publishing, 2011.

- [13] S. S. Kalsi, *Applications of High Temperature Superconductors to Electric Power Equipment*, 1st ed. John Wiley and Sons Inc, 2011.
- [14] H. Maeda and Y. Yanagisawa, “Recent Developments in High-Temperature Superconducting Magnet Technology (Review),” *IEEE Trans. Appl. Supercond.*, vol. 24, no. 3, pp. 1–12, 2014.
- [15] Y. Lvovsky, E. W. Stautner, and T. Zhang, “Novel technologies and configurations of superconducting magnets for MRI,” *Supercond. Sci. Technol.*, vol. 26, no. 9, p. 093001, 2013.
- [16] R. Battesti *et al.*, “High magnetic fields for fundamental physics,” *Phys. Rep.*, vol. 765–766, pp. 1–39, 2018.
- [17] P. Komarek, “Advances in large scale applications of superconductors,” *Supercond. Sci. Technol.*, vol. 13, no. 5, pp. 456–459, 2000.
- [18] M. Zhang, W. Yuan, J. Kvitkovic, and S. Pamidi, “Total AC loss study of 2G HTS coils for fully HTS machine applications,” *Supercond. Sci. Technol.*, vol. 28, no. 11, p. 115011, 2015.
- [19] L. Quéval, V. M. R. Zermeño, and F. Grilli, “Numerical models for ac loss calculation in large-scale applications of HTS coated conductors,” *Supercond. Sci. Technol.*, vol. 29, no. 2, p. 024007, 2016.
- [20] K. Coyne, “New world-record magnet fulfills superconducting promise,” 2017. [Online]. Available: <https://nationalmaglab.org/news-events/news/new-world-record-magnet-fulfills-superconducting-promise>. [Accessed: 10-Jan-2020].
- [21] F. Grilli, E. Pardo, A. Stenvall, D. N. Nguyen, W. Yuan, and F. Gomory, “Computation of losses in HTS under the action of varying magnetic fields and currents,” *IEEE Trans. Appl. Supercond.*, vol. 24, no. 1, pp. 78–110, 2014.
- [22] V. M. R. Zermeno, A. B. Abrahamsen, N. Mijatovic, B. B. Jensen, and M. P. Sørensen, “Calculation of alternating current losses in stacks and coils made of second generation high temperature superconducting tapes for large scale applications,” *J. Appl. Phys.*, vol. 114, no. 17, p. 173901, 2013.
- [23] A. Morandi, “2D electromagnetic modelling of superconductors,” *Supercond. Sci. Technol.*, vol. 25, no. 10, p. 104003, 2012.
- [24] N. Amemiya and K. Akachi, “Magnetic field generated by shielding current in high Tc superconducting coils for NMR magnets,” *Supercond. Sci. Technol.*, vol. 9, no. 21, p. 095001, 2008.
- [25] Y. Yanagisawa *et al.*, “Magnitude of the screening field for YBCO coils,” *IEEE Trans. Appl. Supercond.*, vol. 21, no. 3, pp. 1640–1643, 2011.
- [26] Y. Yanagisawa, Y. Xu, X. Jin, H. Nakagome, and H. Maeda, “Reduction of screening current-induced magnetic field of REBCO coils by the use of multi-filamentary tapes,” *IEEE Trans. Appl. Supercond.*, vol. 25, no. 3, pp. 1–5, 2015.
- [27] Y. Li *et al.*, “Magnetization and screening current in an 800-MHz (18.8-T) REBCO NMR

- insert magnet: experimental results and numerical analysis,” *Supercond. Sci. Technol.*, vol. 32, no. 10, p. 105007, 2019.
- [28] J. Xia, H. Bai, H. Yong, H. W. Weijers, T. A. Painter, and M. D. Bird, “Stress and strain analysis of a REBCO high field coil based on the distribution of shielding current,” *Supercond. Sci. Technol.*, vol. 32, no. 9, p. 095005, 2019.
- [29] R. Brambilla, F. Grilli, and L. Martini, “Development of an edge-element model for AC loss computation of high-temperature superconductors,” *Supercond. Sci. Technol.*, vol. 20, no. 1, pp. 16–24, 2007.
- [30] Z. Hong, A. M. Campbell, and T. A. Coombs, “Numerical solution of critical state in superconductivity by finite element software,” *Supercond. Sci. Technol.*, vol. 19, no. 12, pp. 1246–1252, 2006.
- [31] G. P. Mikitik, Y. Mawatari, A. T. S. Wan, and F. Sirois, “Analytical methods and formulas for modeling high temperature superconductors,” *IEEE Trans. Appl. Supercond.*, vol. 23, no. 2, pp. 8001920–8001920, 2013.
- [32] B. Shen, F. Grilli, and T. A. Coombs, “Review of the AC loss computation for HTS using H formulation,” *Supercond. Sci. Technol.*, vol. 33, no. 3, p. 033002, 2020.
- [33] H. Zhang, M. Zhang, and W. Yuan, “An efficient 3D finite element method model based on the T-A formulation for superconducting coated conductors,” *Supercond. Sci. Technol.*, vol. 30, no. 2, p. 024005, 2016.
- [34] F. Liang *et al.*, “A finite element model for simulating second generation high temperature superconducting coils/stacks with large number of turns,” *J. Appl. Phys.*, vol. 122, no. 4, p. 043903, 2017.
- [35] A. . Read, “Linear interpolation of histograms,” *Nucl. Instruments Methods Phys. Res. Sect. A Accel. Spectrometers, Detect. Assoc. Equip.*, vol. 425, no. 1–2, pp. 357–360, Apr. 1999.
- [36] M. Tinkham, *Introduction to superconductivity*, 2nd ed. McGraw-Hill, Inc., 1996.
- [37] R. G. Sharma, *Superconductivity Basics and Applications to Magnets*, 1st ed. Springer International Publishing, 2015.
- [38] A. A. Abrikosov, “On the Magnetic Properties of Superconductors of the Second Group,” *Sov. Phys. JETP*, vol. 5, no. 6, pp. 1174–1182, 1957.
- [39] S. R. Foltyn *et al.*, “Materials science challenges for high-temperature superconducting wire,” *Nat. Mater.*, vol. 6, no. 9, pp. 631–641, Sep. 2007.
- [40] Y. B. Kim, C. F. Hempstead, and A. R. Strnad, “Flux-Flow Resistance in Type-II Superconductors,” *Phys. Rev.*, vol. 139, no. 4A, pp. A1163–A1172, Aug. 1965.
- [41] A. C. Rose-Innes and E. H. Rhoderick, *Introduction to Superconductivity*, 2nd ed. Pergamon, 1978.
- [42] D. X. Fischer, R. Prokopec, J. Emhofer, and M. Eisterer, “The effect of fast neutron irradiation on the superconducting properties of REBCO coated conductors with and without artificial

- pinning centers,” *Supercond. Sci. Technol.*, vol. 31, no. 4, p. 044006, 2018.
- [43] F. S. Wells, A. V. Pan, X. R. Wang, S. A. Fedoseev, and H. Hilgenkamp, “Analysis of low-field isotropic vortex glass containing vortex groups in YBa₂Cu₃O_{7-x} thin films visualized by scanning SQUID microscopy,” *Sci. Rep.*, vol. 5, no. 1, 2015.
- [44] L. Prigozhin, “On the Bean critical-state model in superconductivity,” *Eur. J. Appl. Math.*, vol. 7, no. 3, pp. 237–247, 1996.
- [45] C. P. Bean, “Magnetization of hard superconductors,” *Phys. Rev. Lett.*, vol. 8, no. 6, pp. 250–253, 1962.
- [46] C. P. Bean, “Magnetization of high-field superconductors,” *Rev. Mod. Phys.*, vol. 36, no. 1, pp. 31–39, 1964.
- [47] A. M. Campbell and J. E. Evetts, “Flux vortices and transport currents in type II superconductors,” *Adv. Phys.*, vol. 50, no. 8, pp. 1249–1449, 2001.
- [48] Y. B. Kim, C. F. Hempstead, and A. R. Strnad, “Flux creep in hard superconductors,” *Phys. Rev.*, vol. 131, no. 6, pp. 2486–2495, 1963.
- [49] J. Rhyner, “Magnetic properties and AC-losses of superconductors with power law current-voltage characteristics,” *Phys. C Supercond. its Appl.*, vol. 212, no. 3–4, pp. 292–300, 1993.
- [50] M. D. Ainslie and H. Fujishiro, “Modelling of bulk superconductor magnetization,” *Supercond. Sci. Technol.*, vol. 28, no. 5, p. 053002, 2015.
- [51] Y. B. Kim, C. F. Hempstead, and A. R. Strnad, “Magnetization and critical supercurrents,” *Phys. Rev.*, vol. 129, no. 2, pp. 528–535, 1963.
- [52] D. K. Hilton, A. V. Gavrilin, and U. P. Trociewitz, “Practical fit functions for transport critical current versus field magnitude and angle data from (RE)BCO coated conductors at fixed low temperatures and in high magnetic fields,” *Supercond. Sci. Technol.*, vol. 28, no. 7, p. 074002, 2015.
- [53] G. G. Sotelo, M. Carrera, J. Lopez-Lopez, and X. Granados, “H-Formulation FEM Modeling of the Current Distribution in 2G HTS Tapes and Its Experimental Validation Using Hall Probe Mapping,” *IEEE Trans. Appl. Supercond.*, vol. 26, no. 8, pp. 1–10, 2016.
- [54] K. P. Thakur, A. Raj, E. H. Brandt, J. Kvitkovic, and S. V. Pamidi, “Frequency-dependent critical current and transport ac loss of superconductor strip and Roebel cable,” *Supercond. Sci. Technol.*, vol. 24, no. 6, p. 065024, 2011.
- [55] F. Sirois and F. Grilli, “Potential and limits of numerical modelling for supporting the development of HTS devices,” *Supercond. Sci. Technol.*, vol. 28, no. 4, p. 043002, 2015.
- [56] F. Grilli, F. Sirois, V. M. R. Zermeno, and M. Vojenciak, “Self-Consistent Modeling of the I_c of HTS Devices: How Accurate do Models Really Need to Be?,” *IEEE Trans. Appl. Supercond.*, vol. 24, no. 6, pp. 1–8, 2014.
- [57] V. M. R. Zermeno, K. Habelok, M. Stępień, and F. Grilli, “A parameter-free method to extract the superconductor’s $J_c(B, \theta)$ field-dependence from in-field current-voltage characteristics

- of high temperature superconductor tapes,” *Supercond. Sci. Technol.*, vol. 30, no. 3, p. 034001, 2017.
- [58] E. Pardo, M. Vojenčiak, F. Gömöry, and J. Šouc, “Low-magnetic-field dependence and anisotropy of the critical current density in coated conductors,” *Supercond. Sci. Technol.*, vol. 24, no. 6, p. 065007, 2011.
- [59] V. M. R. Zermeño, S. Quaiyum, and F. Grilli, “Open-Source Codes for Computing the Critical Current of Superconducting Devices,” *IEEE Trans. Appl. Supercond.*, vol. 26, no. 3, pp. 1–7, 2016.
- [60] W. T. Norris, “Calculation of hysteresis losses in hard superconductors carrying ac: Isolated conductors and edges of thin sheets,” *J. Phys. D. Appl. Phys.*, vol. 3, no. 4, pp. 489–507, 1970.
- [61] M. R. Halse, “AC face field losses in a type II superconductor,” *J. Phys. D. Appl. Phys.*, vol. 3, no. 5, pp. 717–720, 1970.
- [62] E. H. Brandt, “Thin superconductors in a perpendicular magnetic ac field: General formulation and strip geometry,” *Phys. Rev. B*, vol. 49, no. 13, pp. 9024–9040, 1994.
- [63] Y. Mawatari, “Critical state of periodically arranged superconducting-strip lines in perpendicular fields,” *Phys. Rev. B - Condens. Matter Mater. Phys.*, vol. 54, no. 18, pp. 13215–13221, 1996.
- [64] K. H. Müller, “Self-field hysteresis loss in periodically arranged superconducting strips,” *Phys. C Supercond. its Appl.*, vol. 289, no. 1–2, pp. 123–130, 1997.
- [65] J. R. Clem, “Field and current distributions and ac losses in a bifilar stack of superconducting strips,” *Phys. Rev. B - Condens. Matter Mater. Phys.*, vol. 77, no. 13, p. 134506, 2008.
- [66] F. Grilli, “Numerical modeling of HTS applications,” *IEEE Trans. Appl. Supercond.*, vol. 26, no. 3, pp. 1–8, 2016.
- [67] R. Brambilla, F. Grilli, L. Martini, and F. Sirois, “Integral equations for the current density in thin conductors and their solution by the finite-element method,” *Supercond. Sci. Technol.*, vol. 21, no. 10, p. 105008, 2008.
- [68] L. Prigozhin, “Analysis of critical-state problems in type-II superconductivity,” *IEEE Trans. Appl. Supercond.*, vol. 7, no. 4, pp. 3866–3873, 1997.
- [69] L. Prigozhin and V. Sokolovsky, “Computing AC losses in stacks of high-temperature superconducting tapes,” *Supercond. Sci. Technol.*, vol. 24, no. 7, p. 075012, 2011.
- [70] E. Pardo, F. Gömöry, J. Šouc, and J. M. Ceballos, “Current distribution and ac loss for a superconducting rectangular strip with in-phase alternating current and applied field,” *Supercond. Sci. Technol.*, vol. 20, no. 4, pp. 351–364, 2007.
- [71] E. Pardo, J. Šouc, and L. Frolek, “Electromagnetic modelling of superconductors with a smooth current-voltage relation: Variational principle and coils from a few turns to large magnets,” *Supercond. Sci. Technol.*, vol. 24, no. 8, p. 044003, 2015.
- [72] E. Pardo, “Modeling of screening currents in coated conductor magnets containing up to

40000 turns,” *Supercond. Sci. Technol.*, vol. 29, no. 8, p. 085004, 2016.

- [73] J. P. Bastos and N. Sadowski, *Electromagnetic Modeling by Finite Element Methods*, 1st ed. CRC Press, 2003.
- [74] J.-M. Jin, *The Finite Element Method in Electromagnetics*, 2nd ed. New York: Wiley, 2002.
- [75] J.-M. Jin, *Theory and Computation of Electromagnetic Field*. John Wiley & Sons, Inc., 2010.
- [76] F. Grilli, R. Brambilla, and L. Martini, “Modeling high-temperature superconducting tapes by means of edge finite elements,” *IEEE Trans. Appl. Supercond.*, vol. 17, no. 2, pp. 3155–3158, 2007.
- [77] G. Barnes, M. McCulloch, and D. Dew-Hughes, “Computer modelling of type II superconductors in applications,” *Supercond. Sci. Technol.*, vol. 12, no. 8, pp. 518–522, 1999.
- [78] T. A. Coombs, A. M. Campbell, A. Murphy, and M. Emmens, “A fast algorithm for calculating the critical state in superconductors,” *COMPEL - Int. J. Comput. Math. Electr. Electron. Eng.*, vol. 20, no. 1, pp. 240–252, 2001.
- [79] A. M. Campbell, “A direct method for obtaining the critical state in two and three dimensions,” *Supercond. Sci. Technol.*, vol. 22, no. 3, p. 034005, 2009.
- [80] N. Amemiya, S. I. Murasawa, N. Banno, and K. Miyamoto, “Numerical modelings of superconducting wires for AC loss calculations,” *Phys. C Supercond. its Appl.*, vol. 310, no. 1–4, pp. 16–29, 1998.
- [81] A. Stenvall and T. Tarhasaari, “Programming finite element method based hysteresis loss computation software using non-linear superconductor resistivity and $T - \phi$ formulation,” *Supercond. Sci. Technol.*, vol. 23, no. 7, p. 075010, 2010.
- [82] R. Pecher, M. McCulloch, S. J. Chapman, L. Prigozhin, and C. M. Elliott, “3D-modelling of bulk type-II superconductors using unconstrained H-formulation,” *Proc. Inst. Phys. Conf. Ser.*, vol. 181, pp. 1–11, 2003.
- [83] K. Kajikawa, T. Hayashi, R. Yoshida, M. Iwakuma, and K. Funaki, “Numerical evaluation of AC losses in HTS wires with 2D FEM formulated by self magnetic field,” *IEEE Trans. Appl. Supercond.*, vol. 13, no. 2, pp. 3630–3633, 2003.
- [84] S. Sugita and H. Ohsaki, “Numerical analysis of AC losses in REBCO thin film for coated conductor and fault current limiter,” *Phys. C Supercond. its Appl.*, vol. 392–396, no. 2, pp. 1150–1155, 2003.
- [85] Y. Ichiki and H. Ohsaki, “Numerical analysis of AC loss characteristics of YBCO coated conductors arranged in parallel,” *IEEE Trans. Appl. Supercond.*, vol. 15, no. 2, pp. 2851–2854, 2005.
- [86] F. Sass, G. G. Sotelo, R. De Andrade, and F. Sirois, “H-formulation for simulating levitation forces acting on HTS bulks and stacks of 2G coated conductors,” *Supercond. Sci. Technol.*, vol. 28, no. 12, p. 125012, 2015.
- [87] V. M. Rodriguez-Zermeno *et al.*, “Towards faster FEM simulation of thin film

- superconductors: A multiscale approach,” *IEEE Trans. Appl. Supercond.*, vol. 21, no. 3, pp. 3273–3276, 2011.
- [88] V. M. Zermeno, M. P. Sørensen, N. F. Pedersen, N. Mijatovic, and A. B. Abrahamsen, “Fast 2D Simulation of Superconductors: a Multiscale Approach,” *Proc. COMSOL Conf.*, 2009.
- [89] M. D. Ainslie, T. J. Flack, Z. Hong, and T. A. Coombs, “Comparison of first- and second-order 2D finite element models for calculating AC loss in high temperature superconductor coated conductors,” *COMPEL - Int. J. Comput. Math. Electr. Electron. Eng.*, vol. 30, no. 2, pp. 762–774, 2011.
- [90] B. Shen *et al.*, “Investigation of AC losses in horizontally parallel HTS tapes,” *Supercond. Sci. Technol.*, vol. 30, no. 7, p. 075006, 2017.
- [91] H. Liu, G. Li, H. Zhang, and Y. Wang, “Numerical modeling and experimental analysis of AC critical current in YBCO-coated conductors,” *IEEE Trans. Appl. Supercond.*, vol. 25, no. 3, pp. 1–5, 2015.
- [92] V. M. R. Zermeno, F. Grilli, and F. Sirois, “A full 3D time-dependent electromagnetic model for Roebel cables,” *Supercond. Sci. Technol.*, vol. 26, no. 5, p. 052001, 2013.
- [93] F. Grilli, R. Brambilla, F. Sirois, A. Stenvall, and S. Memiaghe, “Development of a three-dimensional finite-element model for high-temperature superconductors based on the H-formulation,” *Cryogenics (Guildf.)*, vol. 53, pp. 142–147, 2013.
- [94] A. Stenvall, V. Lahtinen, and M. Lyly, “An H-formulation-based three-dimensional hysteresis loss modelling tool in a simulation including time varying applied field and transport current: The fundamental problem and its solution,” *Supercond. Sci. Technol.*, vol. 27, no. 10, p. 104004, 2014.
- [95] E. Berrospe-Juarez, V. M. R. Zermeño, F. Trillaud, and F. Grilli, “Real-time simulation of large-scale HTS systems: multi-scale and homogeneous models using the T–A formulation,” *Supercond. Sci. Technol.*, vol. 32, no. 6, p. 065003, 2019.
- [96] J. R. Clem, J. H. Claassen, and Y. Mawatari, “AC losses in a finite Z stack using an anisotropic homogeneous-medium approximation,” *Supercond. Sci. Technol.*, vol. 20, no. 12, pp. 1130–1139, 2007.
- [97] W. Yuan, A. M. Campbell, and T. A. Coombs, “A model for calculating the AC losses of second-generation high temperature superconductor pancake coils,” *Supercond. Sci. Technol.*, vol. 22, no. 7, p. 075028, 2009.
- [98] V. M. R. Zermeño and F. Grilli, “3D modeling and simulation of 2G HTS stacks and coils,” *Supercond. Sci. Technol.*, vol. 27, no. 4, p. 044025, 2014.
- [99] L. Queval and H. Ohsaki, “AC losses of a grid-connected superconducting wind turbine generator,” *IEEE Trans. Appl. Supercond.*, vol. 23, no. 3, pp. 5201905–5201905, 2013.
- [100] “COMSOL Multiphysics version 5.3.” [Online]. Available: www.comsol.com. [Accessed: 10-Jan-2020].
- [101] W. D. Markiewicz *et al.*, “Design of a superconducting 32 T magnet with REBCO high field

- coils,” *IEEE Trans. Appl. Supercond.*, vol. 22, no. 3, pp. 4300704–4300704, 2012.
- [102] J. Xia, H. Bai, J. Lu, A. V. Gavrilin, Y. Zhou, and H. W. Weijers, “Electromagnetic modeling of REBCO high field coils by the H-formulation,” *Supercond. Sci. Technol.*, vol. 28, no. 12, p. 125004, 2015.
- [103] S. C. Chapra, *Métodos numéricos para ingenieros*, 5th ed. McGraw Hill, 2007.
- [104] E. Berrospe-Juarez, V. M. R. Zermeño, F. Trillaud, and F. Grilli, “Iterative multi-scale method for estimation of hysteresis losses and current density in large-scale HTS systems,” *Supercond. Sci. Technol.*, vol. 31, no. 9, p. 095002, 2018.
- [105] “Piecewise Cubic Hermite Interpolating Polynomial (PCHIP).” [Online]. Available: <https://www.mathworks.com/help/matlab/ref/pchip.html>. [Accessed: 05-Sep-2019].
- [106] C. R. Vargas-Llanos, V. M. R. Zermeño, S. Sanz, F. Trillaud, and F. Grilli, “Estimation of hysteretic losses for MgB₂ tapes under the operating conditions of a generator,” *Supercond. Sci. Technol.*, vol. 29, no. 3, p. 034008, 2016.
- [107] N. Bonneel, M. van de Panne, S. Paris, and W. Heidrich, “Displacement interpolation using Lagrangian mass transport,” *ACM Trans. Graph.*, vol. 30, no. 6, pp. 1–12, 2011.
- [108] National Research Council, Division on Engineering and Physical Sciences, Board on Physics and Astronomy, and Committee to Assess the Current Status and Future Direction of High Magnetic Field Science in the United States, *High Magnetic Field Science and Its Application in the United States: Current Status and Future Directions*. Washington, DC, USA: The National Academies Press, 2013.
- [109] D. Abraimov *et al.*, “Double disordered YBCO coated conductors of industrial scale: High currents in high magnetic field,” *Supercond. Sci. Technol.*, vol. 28, no. 11, p. 114007, 2015.
- [110] K. Tsuchiya *et al.*, “Critical current measurement of commercial REBCO conductors at 4.2 K,” *Cryogenics (Guildf.)*, vol. 85, pp. 1–7, 2017.
- [111] T. Benkel *et al.*, “Preliminary Tests and Margin Estimate for a REBCO Insulated 10 T Insert under High Magnetic Field,” *IEEE Trans. Appl. Supercond.*, vol. 27, no. 4, pp. 1–5, 2017.
- [112] S. Hahn *et al.*, “45.5-tesla direct-current magnetic field generated with a high-temperature superconducting magnet,” *Nature*, vol. 570, no. 7762, pp. 496–499, 2019.
- [113] J. R. Miller, “The NHMFL 45-T hybrid magnet system: Past, present, and future,” *IEEE Trans. Appl. Supercond.*, vol. 13, no. 2, pp. 1385–1390, 2003.
- [114] J. Liu, L. Wang, L. Qin, Q. Wang, and Y. Dai, “Recent development of the 25T all-superconducting magnet at IEE,” *IEEE Trans. Appl. Supercond.*, vol. 28, no. 4, pp. 1–5, 2018.
- [115] S. Yoon, J. Kim, H. Lee, S. Hahn, and S. H. Moon, “26 T 35 mm all-GdBa₂Cu₃O_{7-x} multi-width no-insulation superconducting magnet,” *Supercond. Sci. Technol.*, vol. 29, no. 4, 2016.
- [116] H. Schwalbe, “Editorial: New 1.2 GHz NMR Spectrometers— New Horizons?,” *Angew. Chemie - Int. Ed.*, vol. 56, no. 35, pp. 10252–10253, 2017.

- [117] S. Awaji *et al.*, “First performance test of a 25 T cryogen-free superconducting magnet,” *Supercond. Sci. Technol.*, vol. 30, no. 6, p. 065001, 2017.
- [118] H. Maeda, J. I. Shimoyama, Y. Yanagisawa, Y. Ishii, and M. Tomita, “The MIRAI program and the new super-high field NMR initiative and its relevance to the development of superconducting joints in Japan,” *IEEE Trans. Appl. Supercond.*, vol. 29, no. 5, pp. 1–9, 2019.
- [119] T. Benkel *et al.*, “REBCO Performance at High Field with Low Incident Angle and Preliminary Tests for a 10-T Insert,” *IEEE Trans. Appl. Supercond.*, vol. 26, no. 3, pp. 1–5, 2016.
- [120] H. W. Weijers *et al.*, “Progress in the Development and Construction of a 32-T Superconducting Magnet,” *IEEE Trans. Appl. Supercond.*, vol. 24, no. 3, pp. 1–5, 2016.
- [121] A. Voran, H. W. Weijers, W. D. Markiewicz, S. R. Gundlach, J. B. Jarvis, and W. R. Sheppard, “Mechanical Support of the NHMFL 32 T Superconducting Magnet,” *IEEE Trans. Appl. Supercond.*, vol. 27, no. 4, pp. 1–5, 2017.
- [122] M. Breschi, L. Cavallucci, P. L. Ribani, A. V. Gavrilin, and H. W. Weijers, “Analysis of quench in the NHMFL REBCO prototype coils for the 32 T Magnet Project,” *Supercond. Sci. Technol.*, vol. 29, no. 5, p. 055002, 2016.
- [123] M. Breschi, L. Cavallucci, P. L. Ribani, A. V. Gavrilin, and H. W. Weijers, “Modeling of Quench in the Coupled HTS Insert/LTS Outsert Magnet System of the NHMFL,” *IEEE Trans. Appl. Supercond.*, vol. 27, no. 5, pp. 1–13, 2017.
- [124] L. Cavallucci, M. Breschi, P. L. Ribani, A. V. Gavrilin, H. W. Weijers, and P. D. Noyes, “A Numerical Study of Quench in the NHMFL 32 T Magnet,” *IEEE Trans. Appl. Supercond.*, vol. 29, no. 5, pp. 1–5, 2019.
- [125] K. L. Kim *et al.*, “Study on elimination of screening-current-induced field in pancake-type non-insulated HTS coil,” *Supercond. Sci. Technol.*, vol. 29, no. 3, p. 035009, 2016.
- [126] E. Berrospe-Juarez *et al.*, “Estimation of Losses in the (RE)BCO Two-Coil Insert of the NHMFL 32 T All-Superconducting Magnet,” *IEEE Trans. Appl. Supercond.*, vol. 28, no. 3, pp. 1–5, 2018.
- [127] A. Gavrilin, H. Weijers, and M. D. Bird, “Presonal communication.” 2017.
- [128] L. Jun, “Analysis of magnetization induced error field in superconducting magnets,” *arXiv.org*, 2019.
- [129] H. S. Shin, K. H. Kim, J. R. C. Dizon, T. Y. Kim, R. K. Ko, and S. S. Oh, “The strain effect on critical current in YBCO coated conductors with different stabilizing layers,” *Supercond. Sci. Technol.*, vol. 18, no. 12, pp. S364–S368, 2005.
- [130] G. Majkic, R. J. Mensah, V. Selvamanickam, Y. Y. Xie, and K. Salama, “Electromechanical behavior of IBAD/MOCVD YBCO coated conductors subjected to torsion and tension loading,” *IEEE Trans. Appl. Supercond.*, vol. 19, no. 3, pp. 3003–3008, 2009.
- [131] D. J. Kolb-Bond *et al.*, “Computing Strains due to Screening Currents in REBCO Magnets,” *IEEE Trans. Appl. Supercond.*, 2020.

- [132] “HTS Modelling Workgroup,” 2020. [Online]. Available: <http://www.htsmodelling.com/>. [Accessed: 10-Jan-2020].
- [133] “Solving PDEs in Python—The FEniCS Tutorial Volume I,” 2018. [Online]. Available: https://fenicsproject.org/pub/%0Dtutorial/html/._ftut1009.html. [Accessed: 22-Nov-2018].
- [134] P. Hood and C. Taylor, “Navier–Stokes equations using mixed interpolation,” *Finite Elem. Methods Flow Probl.* (edited by J. T. Oden al) UAH Press. Huntsv., pp. 121–132, 1974.